Roma Tre

Metodi e Modelli Per l'Ingegneria Sostenibile

CORSO DI DOTTORATO DI RICERCA IN

XXXVIII

CICLO DEL CORSO DI DOTTORATO

Real-Time Parameters Estimations and Adaptive Control Structures for Power Converters in Grid-Tied and Railways Applications

Titolo della tesi

Giovanni Marini

Nome e Cognome del dottorando

Alessandro Lidozzi

Docente Guida/Tutor: Prof.

Marco Sebastiani

Coordinatore: Prof.

Abstract

This dissertation develops a unified framework for real time impedance awareness and adaptive control of power electronic converters operating under variable grid and load conditions. Variations in grid impedance, driven by changes in strength, topology, loading and operating points, directly influence stability margins, achievable bandwidth, harmonic behaviour and resonance phenomena, particularly in LCL-filtered converters. To address these challenges, the thesis proposes an end-to-end workflow that connects measurement, impedance estimation, parameter extraction and automatic controller adaptation, with explicit consideration of disturbance magnitude, sensing resolution and computational latency.

Three complementary estimation approaches are formulated. Active methods rely on controlled excitation: a band-limited White-Noise injection enables broadband impedance acquisition with minimal implementation overhead, while a deterministic Multi-Sine signal provides frequency-selective stimulation with improved signal-to-noise ratio and reduced observation time. Both methods are designed to operate within the dynamic limits of switching frequency, ensuring meaningful identification across the frequency range bounded by the LCL resonance.

A Quasi-Passive strategy is introduced to limit the frequency of active injections. Small variations of active and reactive power generate a compact set of operating points from which the impedance is estimated in real time. A triggering logic based on RMS-voltage deviation and current-harmonic distortion activates the estimator only when grid changes materially affect resistive or inductive behaviour. A fully passive method is also developed to exploit natural load variations, supported by a consistency metric that filters unreliable estimates in non-ideal operating conditions.

To support embedded implementation, each estimation method adopts processing steps aligned with its operating principle. The active estimators rely on frequency-domain analysis to obtain broadband or selected frequency impedance information, enabling fast self-commissioning of the current controller and configuration of the active damping layer. The Quasi-Passive method instead uses sequential measurements derived from controlled active and reactive power variations and algebraic reconstruction in the dq frame, making it suitable for predictive control applications where low-intrusiveness and selective triggering are required.

A resonance-tracking method is developed for railway systems. It operates on the DC side and identifies the dominant oscillatory mode directly from the power spectral density of the DC-bus current, enabling selective resonances attenuation.

The framework is validated through Hardware-in-the-Loop real-time verifications and laboratory experiments on grid-tied inverters, demonstrating consistent parameter identification across operating conditions and recovery of the intended control bandwidth after parameters updates. The results confirm improved stability in resonance affected scenarios and preservation of power quality performance. The railway application further shows that the same identification philosophy can be used to track time-varying resonances in DC traction networks and to enhance stability under constant power load.

Overall, the dissertation demonstrates that online grid parameters estimation, implemented through active, Quasi-Passive, passive or resonance tracking approaches, becomes practically valuable when its outputs directly drive adaptive control actions, enabling stable and predictable operation in both AC grid-tied converters and railway energy-recovery systems.

1 Background, Motivation and State of the Art

1.1 Introduction

Historically, the transmission and distribution of electrical power have relied on a rigid, unidirectional system designed for passive grid operation [1] [2] [3] [4]. This architecture, characterized by centralized generation and top-down power flow, was well suited to an era dominated by large-scale fossil fuel-based power plants. However, in recent decades, global decarbonization aimed at reducing greenhouse gas emissions and mitigating climate change has accelerated a structural shift in the power system [3] [2]. One of the most significant aspects of this transition is the massive integration of renewable energy sources and Distributed Generation (DG) units, especially at the medium and low-voltage levels [4] [1]. This transformation is gradually turning the electric grid into a more dynamic and interactive system. In an active grid, some distributed loads inject power into the grid (active loads), while others continue to draw power (passive loads). The increasing deployment of PV, wind farms, and battery energy storage systems introduces bidirectional power flows, along with new challenges such as voltage regulation, frequency stability, and fault protection coordination [4] [5] [6] [7] [8].

A major enabler of this transformation is the rapid expansion of power electronics technologies, particularly grid-connected converters like inverters [4] [9] [10] [11]. These devices allow non-synchronous sources to interface with the AC grid and enable functionalities such as fast control, energy shaping, and quality improvement. Among them, the front-end inverter plays a central role [12] [13] [14]. It operates as a bidirectional interface between the power grid and a wide range of loads or generation systems. Depending on the direction of power flow, it can function either as a rectifier or as an inverter, without any change in physical structure. This versatility makes it indispensable in numerous applications: for instance, it powers variable-speed electric motors that require frequency and voltage profiles different from those supplied by the grid; it acts as a grid-interface in photovoltaic systems, where DC power must be converted to synchronized AC; and it enables uninterruptible power supply (UPS) systems to ensure continuity during voltage sags or outages. In all these contexts, the front-end inverter is responsible not only for voltage, frequency, and reactive power regulation, but also for power factor correction, harmonic filtering, and, increasingly, resonance damping [15] [16] [17] [18] [19] [20] [21] [22]. However, the effectiveness of these features is closely tied to accurate real-time knowledge of key grid parameters, most importantly, the grid impedance at the fundamental frequency (50 Hz) [23] [24] [25] [26] [27]. As the range of functionalities assigned to the front-end inverter expands, its performance becomes increasingly dependent on the electrical characteristics of the grid it interfaces with. For this reason, understanding the impedance seen at the converter terminals becomes a prerequisite for ensuring stable operation under varying grid conditions. This parameter is critical in various control and protection applications, including phase-locked loop (PLL) synchronization and islanding detection systems, which prevent unsafe disconnection during grid disturbances [28] [29] [30] [31]. Since impedance changes with time, topology, and location, it cannot be predefined and must be estimated in real-time [32] [5] [33].

A natural consequence of the previous considerations is the need to focus on the equivalent impedance at the Point of Common Coupling (PCC), where the interaction between multiple loads and generation units is most critical. Estimating impedance at this point allows for the evaluation of short-circuit power availability, system stiffness, and the ability to absorb dynamic disturbances [34] [32] [35]. The IEEE 519 standard underscores the importance of this knowledge by setting harmonic distortion limits based on the ratio between short-circuit current and load current, emphasizing a shared responsibility between utilities and consumers for power quality. To interpret impedance variations within a realistic operational context, it is necessary to outline the main structural elements of today's electrical power system. Today, electricity is produced through a hybrid generation infrastructure, where large conventional power stations coexist with an increasing number of smaller, decentralized renewable units. These include both utility-scale solar PV and wind installations, as well as smaller rooftop and community-based DG systems. Electricity is transmitted over long distances through the National Transmission Grid, operating at extra-high voltage levels (around 400 kV), which helps to minimize transmission losses and ensure voltage stability. From generation sites, power is stepped up via transformers and transmitted to regional grids operating at approximately 230 kV. Sub-transmission networks then supply large industrial users and distribute electricity to lower-voltage systems via HV/MV substations. The final stage of delivery occurs through distribution networks, serving medium-voltage (typically 20 kV) and low-voltage (400/230 V) customers, including residential, commercial, and small industrial loads under 200 kW. Medium-voltage networks may adopt various topologies, meshed, ring, double-fed, or radial, but are generally operated in radial mode for simplicity and reliability. In urban LV networks, underground radial cabling is most common. Increasingly, these systems must also manage injections from decentralized energy producers, further complicating operational constraints such as voltage stability, fault detection, and protection discrimination [1] [2] [3].

This overview of the electrical infrastructure highlights that the impedance encountered at different points of the network is inherently dependent on topology, loading and voltage levels. Such variability directly motivates the need for real-time impedance estimation, since fixed or nominal values cannot adequately describe the operating conditions seen by modern converter-based resources. As the penetration of renewable and converter-interfaced resources increases, the resulting grid dynamics become more complex and traditional models of centralized dispatch and inertial stability are no longer sufficient. Grid impedance estimation is becoming a core function in maintaining inverter-grid stability [5] [23] [9] [36]. For example, generalized Nyquist criteria are used to ensure that the impedance ratio between the grid and the inverter output remains within safe bounds, preserving stability under all operating conditions [5] [37] [9] [38]. Additionally, impedance estimation plays a crucial role in fault detection, short-circuit current calculation, voltage regulation, and reactive power support. It is also key to the proper operation of decoupled dq-axis current controllers and advanced modulation strategies such as Adaptive Phase-Locked Loop (APLL) control [39] [28] [40]. A widely used metric to characterize grid strength is the Short-Circuit Ratio (SCR), defined as the square of the RMS grid voltage divided by the product of the grid impedance and the inverter rated power. A low SCR indicates a weak grid, which is more susceptible to instability and requires more robust control design [5] [34].

Numerous studies have explored impedance estimation techniques based on two main phases: first, the measurement of voltage and current at the PCC; and second, signal processing or model-based analysis to extract the impedance characteristics [32] [41]. These methods have been successfully applied to fault detection, anti-islanding protection, adaptive voltage control, and robust inverter regulation [29] [30] [42] [43] [44] [45]. In particular, adaptive control strategies that tune parameters based on real-time impedance estimation have proven effective in maintaining performance despite changing grid conditions [43] [46] [47] [48]. Such dynamic controllers are especially valuable in systems with intermittent renewables like solar and wind, which introduce both temporal variability and spatial unpredictability [5] [4]. Beyond conventional grid-connected contexts, impedance estimation also plays a central role in emerging applications. A particularly active area of research and investment is railway electrification, where power electronics-based converters are increasingly adopted to improve energy efficiency. In these systems, regenerative braking allows traction motors to operate as generators during deceleration phases, injecting power back into the grid. To do so safely and efficiently, real-time impedance estimation is essential: it ensures resonance avoidance, controls the re-injection path, and maintains power quality under dynamic loading conditions [49] [50] [51] [20] [52] [53].

In summary, the integration of renewable sources such as solar and wind marks a foundational shift in power system architecture. This transformation reduces reliance on fossil fuels, lowers emissions, and enhances energy security through diversified generation. However, it also introduces new layers of complexity in grid management. Among the essential tools to address these challenges, real-time impedance estimation stands out as a cornerstone, enabling stability, adaptability, and resilience in future power systems [5] [23] [32].

1.2 Line impedance

The line impedance can be understood as the resistance that a conductor presents to the flow of electric current. In the case of a line powered by constant Direct Current (DC), this resistance produces a purely dissipative effect, converting electrical energy into heat. However, transmission and distribution lines are typically energized with Alternating Current (AC), under which the behaviour of the conductor also includes reactive components, inductive and capacitive, alongside its resistive properties. To better understand the electrical behaviour of a power line, we examine the constitutive laws of the three fundamental passive elements used in its modelling: the resistor, the capacitor, and the inductor. For convenience, sinusoidal quantities are represented in the complex domain, where time-domain differential and integral operations are replaced by algebraic expressions involving the angular frequency ω.

1.2.1 Resistor

A resistor is a purely dissipative component that converts electrical energy into thermal energy through collisions between electrons and the atomic lattice of the conductor. It obeys Ohm's Law, which states that the voltage across the resistor is directly proportional to the current flowing through it. This relationship holds in both time and complex domains:

$$V = R \cdot I \tag{1}$$

Here, V and I are complex phasors corresponding to the sinusoidal voltage $v(t)$ and current $i(t)$, respectively. In a resistor, voltage and current are in phase, meaning there is no phase shift between them, and no reactive power is exchanged.

1.2.2 Capacitor

A capacitor is a reactive component that stores energy in the form of an electric field between its plates. It allows current to flow when the voltage across it changes, effectively opposing voltage variations. In the time domain, the voltage across a capacitor is given by:

$$v(t) = \frac{1}{C} \cdot \int i \cdot dt \tag{2}$$

In the complex domain, the integral of a sinusoidal function becomes a division by $j\omega$, leading to the expression:

$$V = \frac{I}{j\omega \cdot C} \tag{3}$$

Solving for I gives:

$$I = j\omega \cdot C \cdot V \tag{4}$$

This indicates that the current leads the voltage by 90 degrees, a characteristic property of capacitive behaviour. Capacitors do not dissipate power but alternately store and release it each cycle, contributing to reactive power flow in the system.

1.2.3 Inductor

An inductor is a reactive component that stores energy in a magnetic field created by the flow of current through a coil. It resists changes in current, generating a voltage proportional to the rate of change of current. In the time domain, its behaviour is described by:

$$v(t) = L\frac{di}{dt} \tag{5}$$

In the complex domain, differentiation becomes multiplication by $j\omega$, resulting in:

$$V = j\omega \cdot L \cdot I \tag{6}$$

Solving for I:

$$I = \frac{V}{j\omega \cdot L} \tag{7}$$

This means that the current lags the voltage by 90 degrees. Like capacitors, inductors exchange energy with the system rather than dissipating it, making them essential elements in the analysis of reactive power and resonance phenomena.

Together, these three elements provide the foundation for modeling the impedance of a transmission line. Real-world conductors often exhibit a combination of all three behaviours, and their relative impact depends on system parameters such as frequency, geometry, and material properties. In impedance estimation, particularly at the grid interface, understanding the contribution of resistive, capacitive, and inductive components is crucial for designing stable and efficient control systems. To analyse a general case of impedance, consider a two-terminal grid (bipole) composed of an arbitrary interconnection of linear passive elements and no internal sources, as shown in Figure 1. Suppose the bipole is excited by a sinusoidal current source at angular frequency ω and operates under steady-state sinusoidal conditions. Under these conditions, the voltage across the bipole is also sinusoidal and can be conveniently represented using phasors.

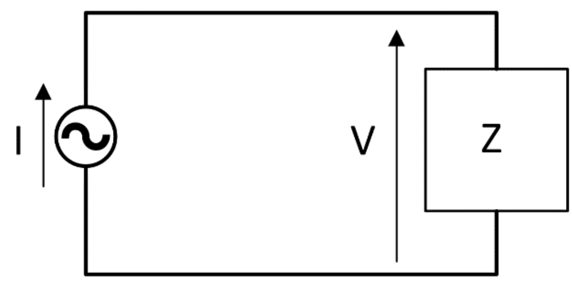

Figure 1 Bipole.

The impedance of the bipole at angular frequency ω is defined as the ratio between the phasor of the voltage V and the phasor of the current I:

$$Z = \frac{V}{I} \tag{8}$$

Here, Z is a complex quantity with units of Ohms [Ω]. By convention, the impedance can be expressed in terms of its real and imaginary components:

$$Z = R + jX \tag{9}$$

Where R is the resistance and X is the reactance of the bipole. Both R and X are generally functions of the angular frequency ω. While the resistance R is always a positive quantity, the reactance X can be either positive or negative, depending on whether inductive or capacitive behaviour dominates. Transmission lines, for example, typically exhibit a net inductive reactance, making X positive in most practical cases.

Impedance can be represented graphically in the complex plane, with resistance on the real axis and reactance on the imaginary axis. The magnitude of the impedance |Z| corresponds to the length of the vector from the origin, while the angle φ between this vector and the real axis is known as the impedance phase. This angle is determined by trigonometric relationships:

$$\cos\varphi = \frac{R}{Z} \qquad \sin\varphi = \frac{X}{Z} \qquad tg\varphi = \frac{X}{R} \tag{10}$$

Since R is always positive, the sign of φ depends solely on the sign of the reactance X. A positive reactance results in a positive phase angle, and vice versa. The power factor, defined as cos φ, plays a central role in evaluating the real power consumed by the bipole.

In sinusoidal steady-state conditions, Ohm’s law becomes:

$$V = Z \cdot I \tag{11}$$

This relationship implies that voltage and current share the same waveform frequency in steady-state sinusoidal conditions. However, this does not necessarily mean they are also in phase. In fact, the product of the complex impedance Z and the current phasor I yields another complex quantity whose magnitude is |Z||I|, and whose phase is the sum of the phases of Z and I. Therefore, even though the waveform shapes are identical, a phase difference can still exist between voltage and current. To better understand the implications of this phase shift, consider two fundamental cases: one in which the impedance has a positive phase angle, and one in which the phase angle is negative.

As illustrated in Figure 2, when the reactance component of the impedance is positive (i.e., inductive), the current lags behind the voltage. Conversely, when the reactance is negative (i.e., capacitive), the current leads the voltage. Voltage and current are in phase only when the impedance is purely real, that is, when the reactance is zero. According to the definition of the impedance angle φ, its sign directly reflects the nature of the reactance and thus determines the phase relationship between voltage and current.

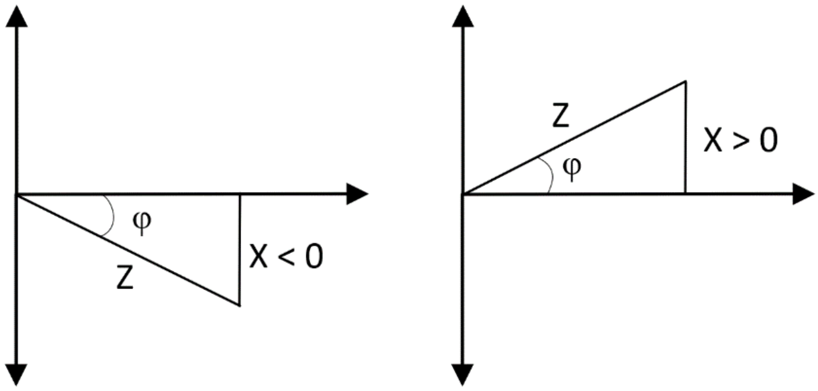

Figure 2 Impedance representation in the imaginary axis.

Two particularly relevant configurations can now be examined: an RLC series circuit and an RLC parallel circuit. In both cases, the total impedance includes a real part and an imaginary part, and the overall phase angle φ cannot be determined a priori without evaluating the frequency-dependent contributions of inductance and capacitance. Therefore, these configurations require a separate analysis of the resistive and reactive components to determine whether the circuit behaves in a predominantly inductive or capacitive manner.

In the case of a series RLC circuit, the voltage across the bipole is given by:

$$V = R \cdot I + j\left(\omega \cdot L - \frac{1}{\omega \cdot C}\right) \cdot I \tag{12}$$

Accordingly, the impedance can be expressed as:

$$Z = \frac{V}{I} = R + j\left(\omega \cdot L - \frac{1}{\omega \cdot C}\right) = R + jX \tag{13}$$

The impedance is composed of a real part R, which is independent of the angular frequency and corresponds to the physical resistance of the bipole, and an imaginary part X, which varies with frequency due to the inductive and capacitive components. Based on the sign of the reactance X, the bipole can be modelled as an RL or RC series circuit: a positive reactance indicates predominantly inductive behaviour, while a negative reactance reflects capacitive dominance.

In the parallel configuration, the total current can be expressed as:

$$I = \frac{V}{R} + \frac{V}{j\omega \cdot L} + j\omega \cdot C \cdot V \tag{14}$$

From this, the equivalent impedance becomes:

$$Z = \frac{V}{I} = \frac{\omega^2 \cdot R \cdot L^2}{\omega^2 \cdot L^2 + \left(\omega^2 \cdot R \cdot L \cdot C - R\right)^2} + j\frac{\omega \cdot L \cdot R^2 \cdot \left(1 - \omega \cdot L \cdot C\right)}{\omega^2 \cdot L^2 + \left(\omega^2 \cdot R \cdot L \cdot C - R\right)^2} = R + jX \tag{15}$$

In this configuration, both the real part R and the imaginary part X of the impedance are frequency dependent. Notably, the real part R no longer represents the physical resistance of a single resistor, but rather the equivalent resistive behaviour of the entire network. As in the series case, it is still possible to represent the bipole using a simplified equivalent model, either parallel RL or parallel RC, depending on whether the net reactance X is positive or negative.

This analytical distinction between inductive and capacitive behaviour is fundamental for designing appropriate impedance models in control and stability studies, particularly when evaluating resonance conditions or implementing damping strategies.

1.3 Motivation

In grid-tied applications, an accurate understanding of the grid impedance is fundamental to ensuring the stable and reliable operation of power electronic converters. Unlike in traditional centralized systems, where the grid could be considered relatively stiff and predictable, modern distribution networks are increasingly characterized by variability, decentralization, and dynamic interactions [9] [32] [5] [54]. This transformation is primarily due to the significant and growing presence of distributed energy resources, which fundamentally alter the nature of the grid's electrical behaviour. Under these conditions, the grid impedance becomes a key parameter that directly influences the performance of connected converters, particularly in terms of stability, control precision, and power quality. This is particularly evident in the impact of impedance on system stability. Inverter-based systems often rely on impedance-based criteria, such as the generalized Nyquist criterion, to assess whether the interaction between the inverter output impedance and the grid impedance will lead to stable operation under given conditions [12] [23] [6]. These criteria provide a framework for analysing the loop gain of the interconnected system in the frequency domain and are particularly valuable when dealing with weak or variable grids where traditional assumptions of grid stiffness no longer hold.

Beyond the issue of stability, accurate estimation of the grid impedance plays a central role in the tuning and adaptation of control parameters. In particular, the design and real-time adjustment of current controllers, phase-locked loops (PLLs), and voltage regulation loops must consider the actual electrical environment in which the converter operates [39] [9] [40]. Static tuning based on nominal or assumed parameters is no longer sufficient. For this reason, self-commissioning techniques have gained attention. These approaches rely on online estimation of the grid impedance to automatically adjust control gains, ensuring robust and responsive performance even during start-up phases or reconnections to unknown networks [24] [55] [15] [42].

Another essential area in which impedance estimation proves indispensable is harmonic compensation. Harmonic currents generated either by the inverter itself or by external loads propagate differently depending on the frequency-dependent nature of the grid impedance. Without proper knowledge of this behaviour, active filtering strategies may become ineffective or even counterproductive. Accurate modelling of impedance across a wide frequency range allows the inverter to selectively cancel targeted harmonics, improving power quality and compliance with standards such as IEEE 519 [4] [9]. Moreover, in systems that are prone to resonance phenomena, impedance estimation becomes a necessary condition for implementing effective damping control strategies. These resonances can occur due to the presence of long distribution cables, transformer inductances, or the interaction between inverter filters and the grid. Particularly in systems using LCL filters, the potential for oscillations is significant. Damping strategies based on real-time impedance estimation can suppress these oscillations without the need for energy-wasting passive components [20] [22] [15] [16] [56] [18] [21]. Such methods are crucial for preserving system efficiency and avoiding interactions with sensitive equipment or communication systems. The role of impedance estimation becomes even more significant when considering advanced applications such as railway electrification. In this context, traction systems and auxiliary converters frequently operate under constant power conditions, introducing dynamic behaviours that further complicate the system response. During regenerative braking, for instance, inverters inject energy back into the grid, and this injection must be carefully managed to avoid exciting unwanted resonances in the catenary network [57] [52] [53] [50] [49] [51]. Real-time impedance information enables the detection of these resonances and facilitates the application of active damping strategies that preserve stability while allowing effective energy recovery.

The increasing presence of constant power loads introduces additional challenges. These types of loads are characterized by negative incremental impedance, which can destabilize the system, especially in weak or resonant networks. Understanding their interaction with the grid is crucial for designing controllers capable of maintaining stability and ensuring safe operation. Impedance estimation contributes to this objective by providing the real-time data needed to implement impedance shaping and adaptive control. Given the wide-ranging implications of grid impedance on converter design, control, and system interaction, the following sections examine in more detail its role in three specific areas. Section 1.2.1 focuses on the assessment of grid strength through the Short-Circuit Ratio, a widely used indicator for identifying weak grid conditions and evaluating their impact on converter stability. Section 1.2.2 explores self-commissioning and active damping strategies, illustrating how these techniques make use of real-time impedance data to improve dynamic performance and suppress resonances. Finally, section 1.2.3 discusses the constant power load problem analysing its destabilizing effects and reviewing control methodologies capable of mitigating its influence. Through this structured analysis, it will become evident that real-time impedance estimation is not simply a useful diagnostic tool, but a foundational element in the design of advanced, flexible, and resilient power electronic systems.

Building upon the motivations outlined above, this thesis pursues a set of coherent research directions aimed at addressing the challenges introduced by variable grid conditions, frequency-dependent behaviours, and constant-power interactions. Specifically, the work investigates:

- **The development of real-time impedance estimation methods** capable of operating under practical converter constraints, both on the AC and DC sides, with the accuracy and bandwidth required for stability-critical applications.
- **The identification of computationally efficient algorithms for extracting resistive, inductive and resonance-related parameters**, suitable for implementation on embedded control hardware and compatible with high-speed sampling and low-latency operation.
- **The integration of impedance-derived information into adaptive control structures**, enabling automatic retuning of current controllers and the configuration of advanced damping strategies that maintain predefined dynamic performance across varying grid conditions.
- **The extension of impedance-aware techniques to railway energy-recovery systems**, where time-varying DC network resonance and constant-power behaviour demand selective, real-time damping actions to preserve stability and ensure effective energy reinjection.

By addressing these lines of investigation, the thesis establishes a unified framework in which impedance estimation is not merely a diagnostic tool but an operational enabler, supporting stability, adaptability, and performance across multiple converter-based applications.

1.3.1 Stability of an electrical grid

A fundamental parameter for assessing the strength of an electrical grid is the Short-Circuit Ratio (SCR) [34] [5], defined as:

$$SCR = \frac{V_g^2}{Z_g \cdot P_n} \tag{16}$$

where:

- V_g is the line-to-line RMS voltage of the grid,
- Z_g is the grid impedance at the Point of Common Coupling (PCC),
- P_n is the rated power of the inverter.

As the grid impedance increases, the SCR decreases, indicating a weaker grid. Grids with an SCR lower than 3 are typically classified as weak. These conditions are often found in rural or remote areas, where long power transmission lines introduce high inductive reactance. Similarly, when renewable energy generation systems are installed in isolated regions, the use of medium-voltage networks and power transformers further increases the inductive impedance. In addition to high impedance, weak grids are characterized by low inertia, especially in systems with a high penetration of distributed generation. This makes them more sensitive to sudden variations in load or generation, posing additional challenges to stability and control [5] [4]. A commonly used method to evaluate the stability of grid-connected inverters involves comparing the grid impedance Z_g with the output impedance of the inverter Z_o, which is generally known and determined by its output filter. According to Nyquist-based stability criteria, stable operation is ensured when the ratio Z_g/Z_o meets certain phase and magnitude conditions [9] [58] [23].

An equivalent circuit used for impedance-based stability analysis is shown in Figure 3.In this representation, the inverter is modelled as a current source in parallel with its output impedance Z_o, while the grid is represented as an ideal voltage source in series with its impedance Z_g.

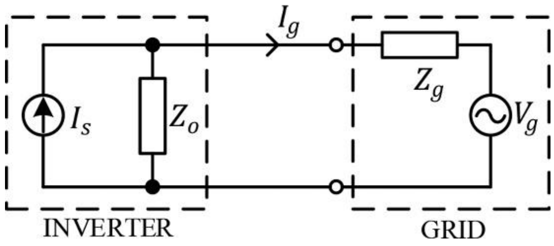

Figure 3 Equivalent circuit.

The expression for the grid current I_g is derived as follows:

$$I_g = \frac{I_g \cdot Z_0 - V_g}{Z_g + Z_0} = \left(I_g - \frac{V_g}{Z_0} \right) \cdot \frac{1}{1 + \frac{Z_g}{Z_0}} \tag{17}$$

where:

- I_s is the current output generated by the inverter,
- V_g is the grid voltage,
- Z_o and Z_g are the inverter and grid impedances, respectively.

This expression clearly shows that the system's behaviour depends on the ratio Z_g/Z_o. If the inverter's output impedance is known, and the grid impedance Z_g is estimated, the stability of the system can be evaluated by applying the Nyquist criterion.

The analysis assumes the following baseline conditions:

1 The grid is inherently stable when the inverter is disconnected.
2 The inverter is stable when connected to an ideal grid with zero impedance.

Under these assumptions, verifying whether the impedance ratio satisfies the Nyquist criterion allows for a reliable assessment of the system's stability margins under real operating conditions.

1.3.2 Self-Commissioning and Active Damping Control

In modern grid-tied power converter systems, particularly those using LCL filters, ensuring system stability across varying grid conditions is a primary concern. As previously discussed, variations in grid impedance, both in its resistive and inductive components, can significantly affect inverter performance. In this context, two strategies have emerged as crucial to maintaining robust and efficient operation: self-commissioning control and active damping.

Self-commissioning control refers to the capability of a converter to automatically tune its control parameters in real-time, based on online impedance estimation, without requiring manual calibration or prior knowledge of the grid conditions [55] [24] [56] [59] [6]. This functionality is particularly important in systems operating under weak or dynamically changing grid environments. By continuously monitoring the estimated grid impedance, the inverter can adapt key parameters, such as the proportional-integral (PI) gains in the current control loop, to maintain desired dynamic performance and phase margin. This results in increased resilience and responsiveness, especially during startup, grid reconnection, or transitions in operating conditions.

At the same time, active damping addresses one of the key challenges introduced by LCL filters: the presence of a resonance peak that can destabilize the current control loop. Unlike passive damping techniques, which rely on resistive elements that dissipate energy and reduce efficiency, active damping methods introduce virtual damping via feedback signals within the control architecture [20] [22] [15] [16] [56] [18] [21]. Among the various implementations, filter-based approaches using Butterworth filters have proven particularly effective, thanks to their tuneable frequency response and low sensitivity to parameter deviations. The combination of low-pass and high-pass filter stages, configured based on real-time impedance data, enables selective attenuation of resonance frequencies without compromising control bandwidth [60]. Recent research has demonstrated that these two strategies can be effectively integrated within a unified framework. These estimates are then fed into the self-commissioning logic to update both the PI controller gains and the active damping parameters. This integrated approach enables real-time adaptation to different grid conditions while ensuring that system stability and harmonic attenuation are preserved across a wide operating range [61] [62] [63] [47] [64].

In summary, self-commissioning control and active damping represent two complementary elements of modern grid-tied inverter design. Together, they provide the flexibility, robustness, and efficiency needed to meet the demands of advanced applications such as distributed generation, renewable integration, and smart grid compatibility. The next sections will delve deeper into their implementation, highlighting their mathematical formulation, filter design considerations, and experimental validation.

1.3.3 Constant Power Load

The increasing use of power electronic converters in both stationary and mobile applications has led to a growing presence of constant power loads (CPLs) in modern electrical systems. A CPL is characterized by its ability to maintain fixed power consumption regardless of input voltage variations. This means that any drop in supply voltage results in a proportional increase in input current, and vice versa, to keep the output power constant. While this behaviour is desirable from a load functionality standpoint, it introduces a fundamental problem at the system level: negative incremental impedance. From the perspective of the source, a CPL behaves as if it were an impedance with a negative slope in the voltage-current (V-I) characteristic curve. As a result, even small voltage fluctuations can lead to amplified current oscillations, potentially triggering instability in systems that are otherwise designed under the assumption of passive load behaviour [65] [42] [63] [66] [67].

This phenomenon is particularly relevant in railway electrification systems, where power converters in auxiliary services or traction applications are increasingly controlled to operate under a constant power regime. For example, during regenerative braking, traction inverters feed energy back into the supply network, often under the control of a DC-link that forces constant power transfer. In such scenarios, the line impedance and any local resonant phenomena interact with the CPL behaviour, potentially leading to low-frequency oscillations, reduced damping, or even unstable operation [57] [68] [50]. In these systems, the presence of a CPL can severely alter the dynamic impedance of the overall network, particularly in weak or resonant conditions such as those introduced by long cables, catenaries, or undersized filters. If not properly accounted for, these interactions can compromise not only the stability of the power interface, but also affect the reliability of railway signalling systems, the continuity of auxiliary services, and the efficiency of energy recovery during braking [49] [51].

Recent studies have emphasized the need for dedicated control strategies when CPLs are present, particularly in scenarios where multiple converters interact or where bidirectional substations and energy storage systems are involved. In such cases, active damping, impedance shaping, and adaptive control become essential tools to preserve system stability [69] [70] [71] [72] [73] [74]. Understanding nature and consequences of constant power load behaviour is therefore a prerequisite for designing robust, efficient, and resilient power electronic interfaces in modern electric transportation systems. The following sections will explore this concept in more detail, presenting the analytical models and experimental evidence that characterize CPL dynamics and their interaction with the surrounding electrical infrastructure [75].

1.4 State of the art

Grid-impedance estimation techniques generally comprise two main stages: first, the acquisition of voltage and current measurements at the grid interface, and second, the numerical processing of those data to extract impedance information with adequate speed, frequency resolution, and accuracy. In modern converters, processing is often carried out in the synchronous dq reference frame, where small-signal impedance is represented by a 2×2 matrix because of frequency coupling, and where many device and network parameters are unknown from a practical "black-box" perspective. This motivates measurement-based approaches that do not require internal models of the converter or external network [76] [23]. Estimation methods are commonly classified as offline or online, depending on when computation occurs relative to measurement. Offline methods process a complete dataset after acquisition and suit detailed analysis or model validation [55] [32]. Online methods operate in real-time, immediately after measuring voltage and current at the Point of Common Coupling during normal inverter operation, enabling controller retuning, stability supervision, and protection in weak or time-varying grids. Online techniques are further divided into passive and active. Passive methods analyse signals already present in the system, such as voltage and current waveforms, naturally occurring harmonics and transients, or switching-induced noise. Their primary advantages are simplicity and non-intrusiveness, since no deliberate disturbance is injected. Typical limitations are low signal-to-noise ratio, dependence on the richness of ambient excitation, and limited control over the identified frequency band. Representative passive approaches include:

- observer-based estimation via Extended Kalman Filter or Recursive Least Squares that track local Thevenin parameters [77] [78];
- methods that follow resonance peak shifts prompted by variations of network inductance or filter parameters [20];
- algebraic estimators in the stationary frame using successive samples of voltage and current [79] [80].
- PMU-based phasor techniques at the fundamental frequency and time–frequency tools such as wavelets are also used to enhance estimation robustness when transients are present [81] [41].

Active methods intentionally inject known disturbances and analyse the response to estimate impedance. They are generally more accurate and versatile, especially for broadband characterization, but they can increase THD, demand more computation, and must be engineered to avoid interference with grid codes and normal operation. The most used active techniques can be grouped into:

- transient signal injection, where short pulses of current or voltage are applied, often at the grid voltage zero-crossing, and the broadband response is processed by FFT or wavelet analysis; this yields rapid estimates but requires high-performance synchronization and acquisition [82];
- harmonic or wideband injection, including single or dual tones, Multi-Sine waveforms, and pseudorandom sequences such as PRBS, MLBS, or related designs; these support frequency-selective estimation with controlled spectral energy and improved SNR [83] [84] [85] [86] [73] [61] [62] [87];

- chirp-based sweeps with controllable spectral evolution and compact time footprint [88] [89] [90];
- power-modulation methods, which alter active and reactive power setpoints to infer the local Thevenin equivalent from pre/post perturbation measurements with minimal invasiveness at the fundamental frequency [91] [92] [93] [41].

While active methods typically outperform passive ones in precision and frequency coverage, practical deployment must balance accuracy, disturbance, and computation. Recent work also describes quasi-passive schemes that monitor a quality metric and trigger a brief active injection only when the ambient conditions no longer support a reliable passive estimate, thereby reducing disturbance frequency [94] [95].

Below is a summary table of some of the known techniques present in the literature.

Table I - Summary of main techniques present in the literature

Category	Method	Frequency range	Characteristics
Passive [96] [97] [82]	Switching-harmonic–based measurement	kHz around *f*sw sidebands	Uses intrinsic PWM ripple; FFT / spectral-line ratios; continuous; very low intrusiveness; **Pros:** no injected disturbance; simple. **Cons:** low SNR at switching bands; sensitive to noise/timing.
Passive [80] [20] [33]	Resonance peak tracking	Tens of Hz → few kHz	No injection; track resonance peaks / curve fitting over a window; very low intrusiveness; **Pros:** detects L/C drift. **Cons:** compute load; may interact with resonant modes.
Passive [55] [42] [77]	Observer-based EKF/RLS (Thévenin)	Fundamental and nearby	Ambient waveforms; EKF/RLS on Thévenin model; continuous; **Pros:** tracks time-varying R_th, X_th. **Cons:** covariance tuning; model mismatch bias.
Passive [34] [98]	Phasor / PMU-based (fundamental)	50/60 Hz fundamental	Synchrophasors; algebra/least-squares; cycle-level; very low intrusiveness; **Pros:** robust at 50/60 Hz. **Cons:** limited spectral coverage; phasor quality needed.
Passive [80] [81] [90]	Wavelet-assisted estimation	Event bands ~10–1000 Hz	Exploits transients; CWT/DWT time–frequency maps; event-driven; **Pros:** good on localized dynamics. **Cons:** needs informative events; design effort.

Active [82] [99] [100]	Zero-crossing transient pulse	Broad: tens of Hz → several kHz	Short i/v pulse at grid zero-cross; FFT/wavelet of transient; **Time:** ms; **Intrusiveness:** medium but brief; **Pros:** one-shot broadband. **Cons:** precise sync & fast A/D required.
Active [43] [85]	Single / dual-tone injection	Selected bins	Inject one/two sinusoids; DFT at injected bins; **Time:** hundreds of ms per tone; **Pros:** high accuracy at chosen points. **Cons:** multiple runs for sweep; added THD.
Active [43] [93]	Non-characteristic low-frequency tone	Near fundamental	E.g., 3rd-harmonic/75 Hz perturbation; Fourier extraction; low intrusiveness; **Use:** LF Z for PLL/voltage-loop tuning.
Active [83] [88] [101]	High-frequency tone(s)	Hundreds of Hz → kHz	Fixed HF tone(s); DFT/lock-in; **Pros:** frequency-selective, controllable amplitude. **Cons:** HF distortion/EMI concerns.
Active [84] [86] [102]	PRBS/MLBS wideband	Design-dependent wideband	Pseudorandom current sequence; FRF via FFT/ratio; short time with averaging; **Pros:** excellent coverage at small amplitudes; good SNR. **Cons:** sequence design & processing complexity.
Active [62] [48] [61]	Multi-Sine	User-selected grid (e.g., 10–1000 Hz)	Sum of many sinusoids with uniform spectral energy; multi-bin DFT/FRF; **Pros:** efficient multi-point estimation; tunable spectrum. **Cons:** signal design; windowing/sync critical.
Active [41] [91] [92]	Power-modulation (P/Q variations)	Fundamental, quasi-steady	Step/modulation of P and/or Q; solve Thévenin pre/post or RLS; minimal disturbance; **Cons:** limited frequency resolution.
Quasi-passive [94] [95]	Observer-triggered injection	As per chosen active method	Trigger a brief injection only when a quality metric degrades (hybrid observer + active method); **Pros:** fewer injections, balances accuracy & PQ. **Cons:** detection delay; extra logic.

2 Active Methods

2.1 Introduction

Active impedance estimation methods are based on the controlled injection of disturbances into the converter system to elicit a measurable and analysable response. Unlike passive techniques that rely on ambient variations or background harmonics, active methods deliberately perturb the system, typically by superimposing current or voltage signals over the nominal operation. These perturbations are designed to stimulate specific frequency components of interest, thereby enabling targeted and high-resolution impedance characterization. The main advantage of active methods lies in their controllability and accuracy. By defining the excitation profile, the designer can optimize the estimation process in terms of frequency coverage, signal-to-noise ratio, and computational requirements. However, these techniques must be carefully implemented to avoid degrading power quality or violating grid codes, especially when operating in sensitive environments such as weak grids or interconnected systems with high penetration of renewable energy. This section presents the active methods that have been studied and implemented as part of this research work. These include white noise injection strategies, multi-sinusoidal excitation methods, and integrated estimation-control architectures that enable simultaneous impedance estimation, self-commissioning, and damping control. Each method is evaluated based on experimental or simulated results, and its suitability for real-time deployment is critically discussed.

2.2 White Noise Based Impedance Estimation [87]

In this section, an active method is proposed to estimate the impedance of both the DC input and AC output sides with reference to a grid-tied three-phase front-end inverter. To this purpose, a White Noise (WN) disturbance is added to the current reference. The impedances are estimated by evaluating the changes in voltages and currents as a response to the disturbance, stimulating only on the AC side and obtaining a synchronous estimation on both AC and DC sides. Bandwidth-limited White Noise was chosen since its inherent simplicity in the generating procedure, compatibility with both Digital Signal Processor and FPGA, and minimal computational resources required. More importantly it has no, theoretically, constraints in bandwidth limitation or frequency generation, unlike the PRBS methodology.

This will increase the maximum estimation frequency when using high switching frequency power converters. Then, two different approaches achieve the result for the inductance and resistance. First, the Least SQuare (LSQ) method approximates the explicit formula of the impedance modulus to the curve derived from the Fourier transform. The proposed technique is a new recursive calculation methodology. In addition to reducing the computation time compared with techniques using the fitting curve method, it is interesting to note that the proposed methodology applies to any impedance estimation method, whether active or passive, that achieves the impedance trend as a function of frequency.

The benefits of the proposed impedance estimation algorithm can be summarized as follows:

Reduced computational effort; fast execution allows evaluating the impedance with higher throughput, which is helpful for time-varying systems; adopting a new recursive calculation approach; providing both the resistive and reactive impedance components; simultaneous estimation on both AC and DC-side.

2.2.1 System Description and Configuration

The equivalent circuit of the system under analysis consists of a three-phase inverter connected to the grid as shown in Figure 4, and having the parameters reported in Table II.

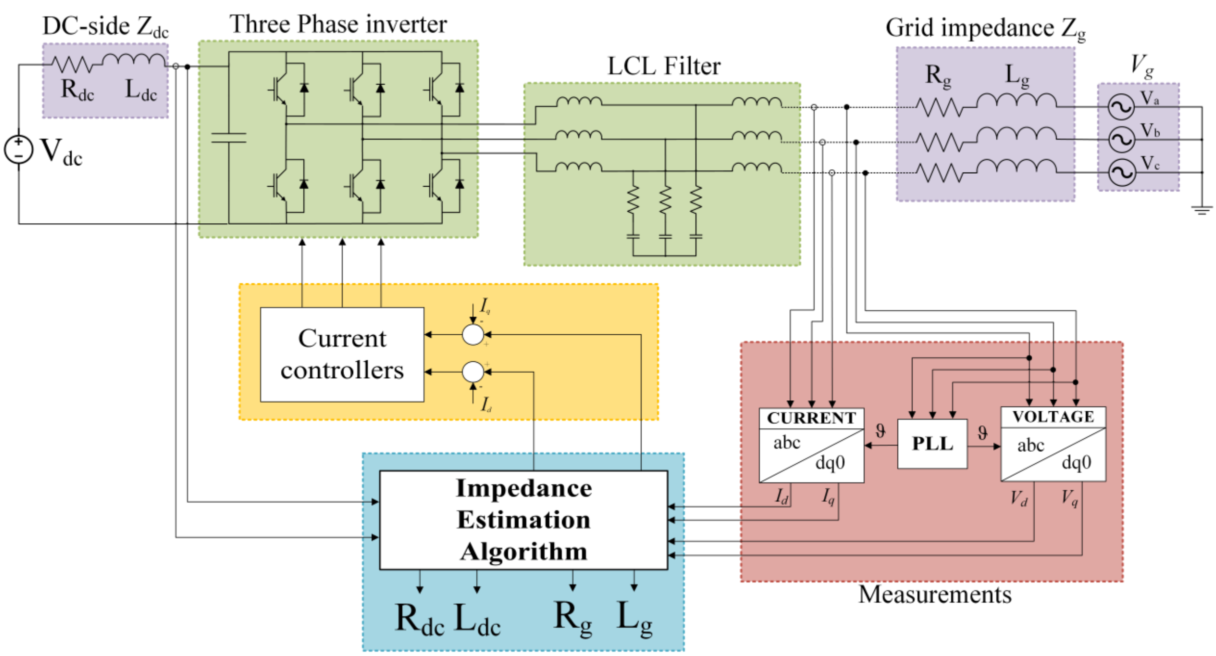

Figure 4 - System block diagram.

The grid was modelled as an equivalent Thevenin circuit with a voltage generator and a resistive-reactive (RL) impedance, neglecting the capacitive behaviour of the line. This approximation can be justified by the fact that the difference in impedance between the two approximations is indistinguishable at the grid frequency and slightly above.

Table II – System parameters

Parameters	Symbol	Value	Parameters	Symbol	Value
Grid voltage (line-to-line, RMS)	V_g	*380 V*	**Inverter-side filter inductance**	L_{fi}	*1 mH*
Grid inductance	L_g	*238.7 μH*	**Inverter-side parasitic resistance**	R_{pi}	*20 mΩ*
Grid resistance	R_g	*0.469 Ω*	**DC-link rate voltage**	V_{DC}	*750 V*
DC-side inductance	L_{dc}	*250 μH*	**DC-link capacitance**	C_i	*5 mF*
DC-side resistance	R_{dc}	*0.1 Ω*	**Switching frequency**	F_{sw}	*10 kHz*
System angular frequency	f_g	*50 Hz*	**Dead-Time**	DT	*3.3 μs*
Grid-side filter inductance	L_{fg}	*55 μH*	**Q-axis reference current**	I_q^*	*30 A*
Grid-side parasitic resistance	R_{pg}	*20 mΩ*	**D-axis reference current**	I_d^*	*0 A*
Filter capacitor	C_f	*5 μF*	**Current control gains**	$K_{p-i}K_{i-i}$	*0.0015* *2.5*
Parasitic capacitor resistance	R_d	*15 mΩ*	**PLL bandwidth (Kalman based)**	$\square_0$	*38 rad/s*
Parasitic capacitor resistance	R_d	*15 mΩ*			

Therefore, the expression of the impedance in the s-domain is:

$$Z = R + sL \qquad (18)$$

The inverter is a three-phase VSI topology current-controlled and connected to the grid by an LCL low-pass filter. Control of the inverter has been implemented in the synchronous reference on the dq-axes. Disturbances and variations used to estimate the grid impedance will be introduced by the control algorithm. The DC-side is again represented by an RL impedance as the capacitive effect of the line is considered negligible at the frequencies of interest.

2.2.2 Impedance Estimation Method

A. Generation of disturbance

The proposed technique is based on injecting a White Noise (WN) based disturbance into the grid via the inverter current reference; the noise magnitude will be proportional to the injected peak current. The parameters for generating the White Noise are two, and they can be considered unrelated to each other. The first parameter to select is the limitation of the WN bandwidth, F_{lbw}, from which the maximum frequency for the impedance estimation can be derived. When selecting the F_{lbw} value, the maximum speed that the current control loop can reach by performing the current tracking must be considered. Theoretically, the system can operate with disturbances up to the Nyquist frequency, whereas, in a experimental case condition the maximum synthesizable frequency is usually lower. In the present case, it was decided to impose the maximum estimation frequency at *2500 Hz*, slightly below the final value of F_{lbw}. Moreover, it will be shown that the maximum estimation frequency of the impedance is also closely related to the resonance frequency of the grid with the inverter output LCL filter on the AC-side, and of the DC line with the inverter capacitor on the DC-side. Therefore, the White Noise bandwidth limiting frequency has been selected to be:

$$F_{lbw} = 3kHz \tag{19}$$

That will be fairly assured of getting a reliable estimation up to *2.5 kHz*. The selected value of F_{lbw} is a good trade-off between the estimation range and the quality of the injected signal, considering that the upper frequency limit is lower between the Nyquist and the resonance frequency. In fact, by making an assessment on the Power Spectrum Density (PSD) as in Figure 5, the energy input to the system tends to cancel out at F_{lbw}.

The PSD has been achieved by sampling the injected WN. It will allow us to quantify the amount of disturbance vs. frequency that will be sent to the grid side. The second parameter to be selected is the noise amplitude, which has two degrees of freedom since it depends on both the amplitude of the WN and the percentage of the reference current by which the White Noise is multiplied. Therefore, the approach was to limit the White Noise amplitude to ± 1 (i.e. normalized output, A_{WN}) and focus on the maximum percentage $\%I_{q(set)}$ that the inverter injects into the grid with respect to the steady-state reference ($I_{q(set)}$). In this manner, the current reference $I_{q(r)}$ can be expressed as

$$I_{q(r)} = I_{q(set)} \cdot \left(1 + \%I_{q(set)} \cdot A_{WN}\right) \tag{20}$$

The choice of this parameter depends on the desired accuracy estimation and speed to be obtained. In fact, the greater the disturbance, the shorter the required sampling duration and then very fast estimation. Therefore, the ideal compromise is to inject a disturbance that is large enough to be tolerated by the grid but at the same time allows a rapid estimation.

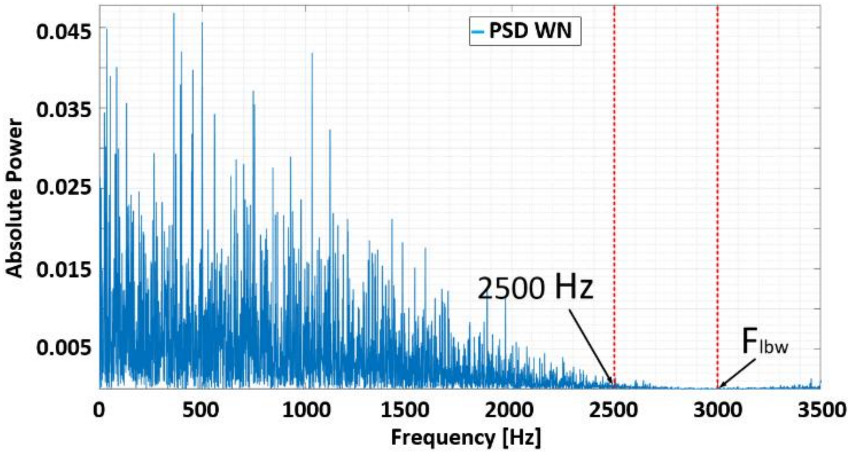

Figure 5 - Power Spectrum Density of the generated White Noise.

B. Disturbance injection and sampling

As the WN generation parameters have been selected, the disturbance is introduced into the grid by the modification of the inverter current reference, as shown in the block diagram of Figure 6. The feedback signals are acquired respectively from the grid and DC sides. The proposed analysis will consider the q-axis voltage and current for AC impedance estimation, and the DC voltage and current for the inverter input link impedance. Those values are then sent to the data-analysis and parameters identification block for the post-processing.

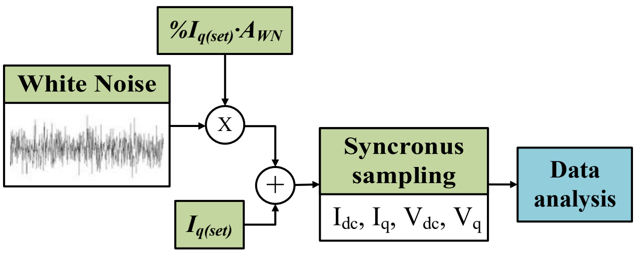

Figure 6 - Block diagram of the signal injection and sampling.

In Figure 7 are reported the collected instantaneous quantities for the q-axis current components, reference, and measured values.

The White Noise disturbance is clearly visible, as well as the relationship between the noise frequency and the capability of the control loop to track the reference. When the disturbance is introduced, a waiting period of *20 ms* is added before starting the sampling of voltage and current values on q-axis.

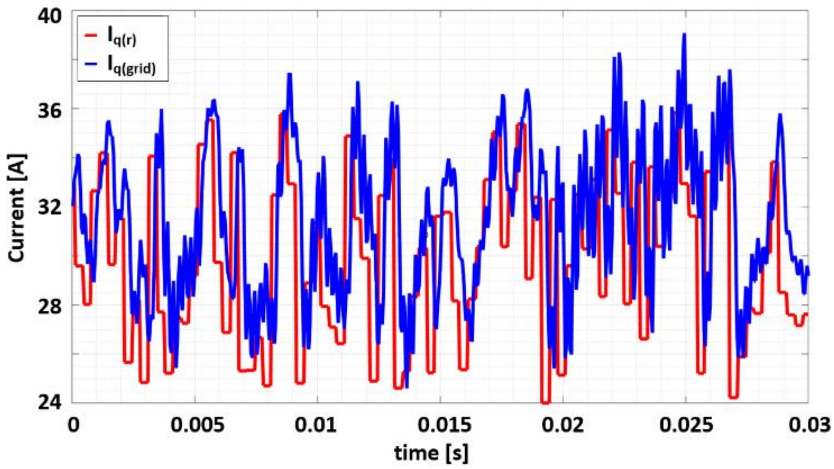

Figure 7 - Reference and grid current q-axis components, $I_{q(r)}$ and $I_{q(grid)}$.

The time of sampling duration t_{sam}, and the number of samples, depends on the resolution to be sought in the impedance estimation. In fact, the achievable frequency resolution in the impedance estimation, F_{res}, is linked to the sampling frequency F_{sam}, through the number of samples N, as:

$$\begin{pmatrix} F_{res} = \dfrac{N}{F_{sam}} \\ t_{sam} = \dfrac{F_{sam}}{N} \end{pmatrix} \rightarrow t_{sam} = \frac{1}{F_{res}} \tag{21}$$

C. *Data-analysis and parameters identification*

As illustrated in Figure 8, after sampling and buffering have been completed, the following steps are then taken:

1. Fourier transform of voltage and current arrays;
2. Impedance vs. frequency calculation;

3. Third-order median filter on the impedance array;
4. Estimation of R and L components
5. Search for R and L using the curve fitting technique based on LSQ;
6. Separate estimation of the R and L components using the proposed iterative technique.

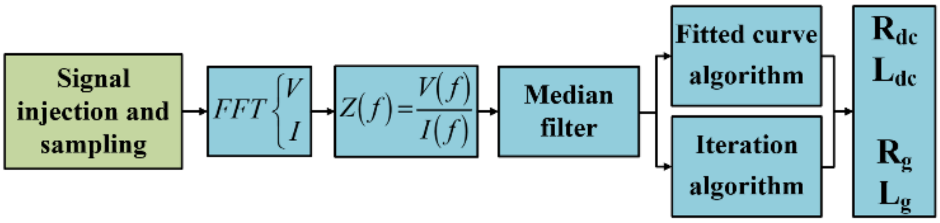

Figure 8 - Block diagram of the analysis and impedance identification.

By the Fourier transform, impedance values can be obtained directly from the q-axis voltage and current values, and in the frequency range that can be expressed as:

$$Z(f)=\frac{V(f)}{I(f)} \tag{22}$$

Hence, it is possible to plot the impedance trend from F_{res} to F_{lbw} in the case of AC-side impedance estimation and up to the DC resonance frequency in the case of DC-side analysis. To derive the resistive and inductive components of the impedance, two separate techniques have been used by introducing a redundant cross-check. The first method is based on the Least Squares technique where the explicit equation of the impedance magnitude is given:

$$Z=\sqrt{R^2+(2\pi fL)^2} \tag{23}$$

The values of R and L are obtained in order that they best approximate the impedance curve. The estimation method was chosen having the capabilities of working with a custom fitting curve. The proposed second method, which uses a completely new approach, takes advantage of an iterative scan of the sampled data that systematizes the previously estimated impedance values. The basic concept is shown in Figure 9. The proposed procedure will be used for both AC and DC impedance estimation.

Specifically, two nested loops have been proposed, where four different frequencies have been defined (f_1, f_2, f_3 and f_4), identifying two specific frequency ranges (f_1÷f_2 and f_3÷f_4). At each iteration of the outer loop (Loop1), a dedicated value of Z_a is evaluated: at the very first iteration Z_a is calculated at f_1.

Then, moving to the inner iterative loop (Loop2), keeping the previously achieved Z_a as a constant during Loop2 iterations, the values of L and R are calculated varying Z_b from f_3 to f_4 with an incremental step of F_{res} as shown in Figure 9 and with reference to (7) and (8). After the iterations of *Loop2*, the achieved arrays containing the L and R values (i.e. having n_2 iterations elements) are the input of a mean operator, which returns a single value for L and R (i.e. stored in L_0 and R_0 arrays shown in Figure 9). Hence, at the end of the n_1 iterations of Loop1, two arrays L_0 and R_0 are finally obtained. A new mean operator was then applied again to finally achieve the single values for L and R. In the specific case of AC impedance estimation, the four frequencies have been selected as f_1=*50 Hz*, f_2= *250 Hz*, f_3=*300 Hz* and f_4=*500 Hz*. For the DC side, the values are f_1=F_{res} *Hz*, f_2= *100 Hz*, f_3=*140 Hz* and f_4=*240 Hz*.

$$L = \sqrt{\frac{Z_b^2 - Z_a^2}{(2\pi f_{Zb})^2 - (2\pi f_{Za})^2}} \tag{24}$$

$$R = \sqrt{Z_a^2 - (2\pi f_{Za} L)^2} \tag{25}$$

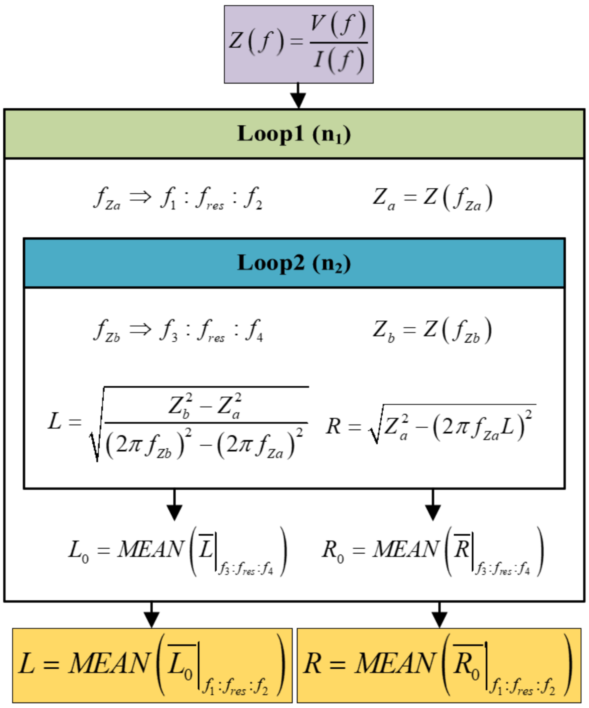

Figure 9 - Block diagram of the proposed RL estimation method used for both AC and DC parameters.

2.3 Multi-Sine Based Impedance Estimation [62]

This section introduces the active grid impedance estimation strategy adopted in this work and motivates the choice of the injected stimulus as a key design variable affecting both accuracy and grid invasiveness. In particular, it presents the proposed Multi-Sine excitation signal, specifically conceived to concentrate energy only at selected frequencies, and then uses it as the reference stimulus to discuss estimation performance and experimental validation.

The work introduces a series of advancements in the field of grid impedance estimation, focusing on accuracy, adaptability, and computational efficiency. The key contributions include:

- Development of a Multi-Sine Signal-Based Approach: The proposed methodology enhances the precision of impedance estimation by utilizing Multi-Sine signals, which provide uniform energy distribution across a specified frequency band. This approach minimizes grid invasiveness and eliminates the need for excessive harmonic distortion
- Using the Multi-Sine signal as a stimulus for the Active impedance estimation, comparing it with the other well-known stimuli: White Noise [87] PRBS. For a fair comparison, all stimuli are designed to have the same RMS value within the frequency range of 1 Hz to 5 kHz, with a frequency band around 5 kHz. The analysis involves examining the Fast Fourier Transforms (FFT) of these stimuli and of the resulting system current under their effect.
- Enabling precise identification of system dynamics across a broad frequency range, ensuring robust grid integration and effective active damping without the need for prior system knowledge or complex offline tuning processes
- Validating the proposed method through experimental tests using a 60 kW VSI connected to an Egston grid emulator, showcasing its effectiveness in a controlled impedance environment with unknown grid impedance.
- Practical Implementation for Grid-Connected Systems: The innovations introduced in this work provide a scalable solution for real-world applications. By integrating innovative signal injection techniques, optimizing spectral resolution, and validating methodologies under diverse conditions, this work lays a robust foundation for adaptive grid management and enhanced inverter performance.

This approach enhances the alignment between stimulus and estimation, improving the overall clarity and reliability of spectral analysis.

2.3.1 System Description

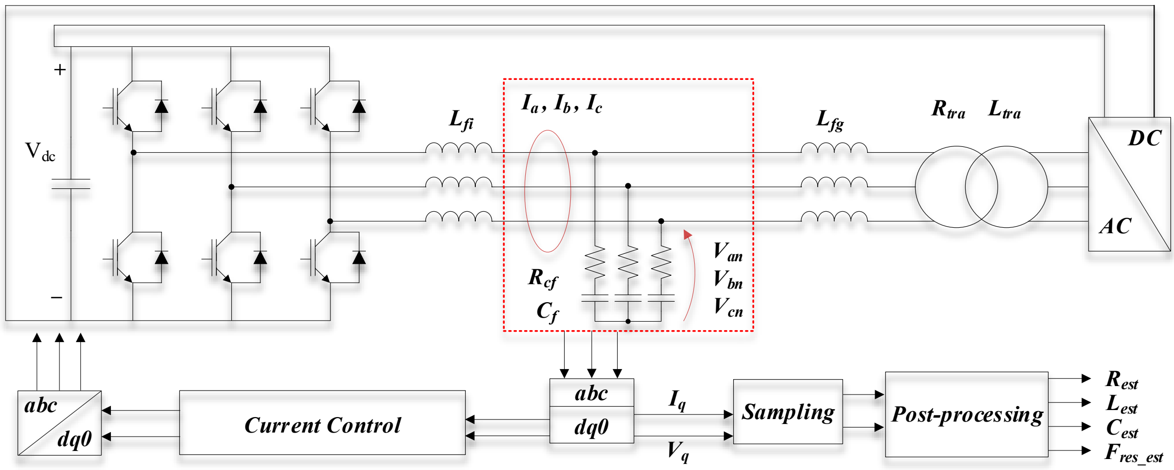

Figure 10 - System block diagram.

Figure 10 presents the complete schematic of the proposed system. It is composed by a three-phase Voltage Source Inverter (VSI) controlled with Pulse Width Modulation (PWM) with switching frequency f_{sw} and supplied by a dc source V_{dc}. L_{fi} is the inverter side inductance, L_{fg} is the grid side inductance, C_f is the capacitor and R_{Cf} is the damping resistance of the filter. R_{tr} and L_{tra} are the respective resistance and inductance of the transformer. The measurements of phase currents (i_a, i_b, i_c) and phase voltages (v_a, v_b, v_c) for the impedance estimation and control are measured respectively on the LCL filter inductance inverter-side and on the LCL filter capacitor. The grid is emulated by another VSI. The inverter current controlled is then connected to the grid through the LCL filter and the current control is implemented in the synchronous dq-axes, with the *d*-axis being 90 degrees leading the *q*-axis. The stimulus for the impedance estimation is added to the *q*-axis current setpoint $i_{q(set)}$. The measured currents and voltages at the PCC are sampled and sent to the online calculation of the estimated grid impedance. The sampling for the impedance estimation is synchronized with the sampling and frequency of the control system f_{ctrl}.

2.3.2 Impedance estimation method

The estimation of impedance strictly depends on the point where voltage and current samples are measured. In this case, the estimated impedance will be constituted by the capacitor of the filter C_f, the grid-side inductance of the filter L_{fg}, and the transformer R_{tra} and L_{tra}. The first step is to make the FFT of the voltage and current sampled. The FFT is used to have the transition from the time domain to the frequency domain, where k represents the frequency bins, as shown in (1), (2) and (3).

$$V[k]=\sum_{n=0}^{N-1} v[n]\cdot e^{-j\frac{2\pi}{N}kn} \tag{26}$$

$$I[k]=\sum_{n=0}^{N-1} i[n]\cdot e^{-j\frac{2\pi}{N}kn} \tag{27}$$

$$f_k=\frac{k\cdot f_{sam}}{N}, \qquad k=0,1,...,N-1 \tag{28}$$

Then the estimation of impedance magnitude and phase is defined as the pointwise ratio of voltage and current in the frequency domain (4)-(5):

$$|Z(f_k)|=\left|\frac{V(k)}{I(k)}\right| \tag{29}$$

$$\theta_Z=\angle V[k]-\angle I[k] \tag{30}$$

There is a correlation between the sampling frequency, the resolution frequency f_{res}, the observation time t_{sam}, and the number of samples N as expressed in (6). The FFT values are multiples of the minimum sampled frequency up to the Nyquist frequency, which is half the sampling frequency.

$$\begin{pmatrix} F_{res}=\dfrac{N}{F_{sam}} \\ t_{sam}=\dfrac{F_{sam}}{N} \end{pmatrix} \rightarrow t_{sam}=\frac{1}{F_{res}} \tag{31}$$

For example, if sampling is done for one-tenth of a second, the minimum sampleable frequency is 10 Hz. Therefore, values will be obtained ranging from 10 Hz and multiples up to the Nyquist frequency.

A. Impedance calculation methodology

The estimation method can be divided into two consecutive steps, as shown in Figure 11. In the first step, a disturbance is injected into the grid. Simultaneously, a synchronous sampling of voltage and current measurements is performed. The disturbance is injected directly into the grid as an addition to the current reference entering the current loop. It is important to note that the disturbance is summed within the current loop, neither before nor after. If it is summed up on the measurement before the current control, it will tend to attenuate it. If it is summed after the current loop, there is a risk of losing control over the reference. In the second step, the collected data is analysed. Firstly, the FFT of the current and voltage samples is performed. Then, the impedance is expressed as the pointwise ratio of the values obtained from the FFT. At this stage, misleading data could be present, possibly due to current or voltage spikes or unexpected harmonics that might compromise the accuracy of the measurement, then Savitzky-Golay filter is performed to reduce the average deviation. After this data cleaning process, the curve is analysed by an iterative algorithm, which will be presented later, to extract the parametric values of the impedance. The iterative algorithm used for impedance estimation has been implemented with the goal of optimizing computation time. Therefore, it is straightforward yet effective. As mentioned, impedance is essentially composed of three unknowns: the inductive component, the resistance component, and the frequency. Since the frequency is known, a system of two equations in two unknowns is obtained (17) and (18). After estimating the resistive and inductive components of the impedance, it can determine the resonance frequency by identifying the peak value of the impedance curve as in (19). From there, it can derive the capacitive component of the estimated impedance, which is due to the capacitor in the LCL filter as in (20).

$$R = Z(f_k) \cdot \cos(\varphi_k) \tag{32}$$

$$L = \frac{Z(f_k) \cdot \sin(\varphi_k)}{2 \cdot \pi \cdot f_k} \tag{33}$$

$$f_{resonance} = f \max\left(Z\left(f_k\right)\right) \tag{34}$$

$$C = \frac{1}{\left(2 \cdot \pi \cdot f_{resonance}\right)^2 \cdot L} \tag{35}$$

B. Multi-Sine Based Disturbance

The disturbance used was carefully studied and implemented according to the following guidelines:

1. obtaining an impedance vs frequency curve;
2. optimization of the estimation accuracy results;
3. minimization of the time required and the injected disturbance;

To satisfy point 1, it was necessary to use a frequency sweep. As it is well known, the accuracy of the estimate is closely related to the injected disturbance; therefore, to satisfy point 2, a disturbance was developed that injected the same intensity into all frequencies of interest. The estimate is valid only at the frequencies where the disturbance is injected. Regarding point 3, the Multi-Sine is an adaptive stimulus tailored to the needs of the application. Since it consists of a sum of sinusoids, only the necessary sinusoids are injected into the grid to estimate the impedance. As previously discussed, impedance is defined as the ratio of voltage to current in the frequency domain. Therefore, it makes practical sense to express impedance as the ratio of voltage and current only at the stimulated frequencies and introducing more harmonics than needed is not useful. To optimize the estimation, firstly it is necessary to choose the desired observation time. Keep in mind that increasing the observation time results in more samples, which improves frequency resolution and thus the estimation accuracy. However, this also increases the time required for both observation and computation, significantly raising computational effort. In conclusion, Multi-Sine stimulus was formed by summing several sinusoids of the same amplitude, but phase shifted in such a way that the final signal was still maintained within the +-1 range. This is the true strength of this stimulus compared to others present in literature. To substantiate this claim later a comparison with known stimuli is presented. Besides that, the maximum bandwidth is strictly related to the switching frequency of the inverter and the cutoff frequency of the current control loop. Firstly, a frequency higher than the Nyquist frequency of the switching frequency would not be attainable. Secondly, it doesn't make much sense to inject a disturbance at frequencies higher than the cutoff frequency of the control loop for two reasons: the first is that it would be attenuated, thereby reducing the accuracy of the estimation; the second is that at frequencies higher than the cutoff frequency of the control loop, there is a risk of unnecessarily exciting the resonance frequency. On the other hand, setting the maximum stimulus frequency too low is not advisable because it is known that inductance responds more effectively at higher frequencies. Therefore, the best compromise is to set the maximum bandwidth equal to the cutoff frequency of the control loop.

Figure 11 - Impedance estimation method flowchart.

2.4 Self-Commissioning and Active Damping Control Application [103]

This work proposes the use of a stimulus for the online active estimation of a resistive-inductive grid impedance. The result is then used for self-commissioning Proportional-Integral (PI) current controller and active damping in a LCL Three-Phase grid-tied Voltage Source Inverter (VSI). Since the grid current is already measured for the impedance estimation its measurement is then optimized and considered as controlled variable and feedback variable for the active damping, avoiding extra sensors in the system.

The contributions of the present work are:

- The control design concept. It considers the fact that for the low frequency range, the capacitor branch can be neglected and the LCL filter behaves like an equivalent L filter [16], [19], [104] of inductance equal to the sum of the LCL inductances plus the grid inductance, being the same valid for the resulting sum of the intrinsic resistances of the LCL inductors and the grid resistance. Then, the cut-off frequency and phase-margin are pre-defined as input parameters for the controller design and kept the same for different grid impedances through the self-commissioning process. This process uses the current grid impedance estimation to calculate the new PI gains based on the methodology proposed in [105], in which the gains for the current controller are explicitly defined to control a Permanent Magnet Synchronous Machine (PMSM).
- A second order Butterworth Low Pass Filter (LPF) followed by a second order Butterworth High Pass Filter (HPF) as feedback coefficient for the Active damping using the grid current as feedback variable, which also has self-commissioning of its parameters based on the actual grid impedance estimation. The current state-of-the-art strategy for using the grid current as feedback variable employs a fixed-parameters first

order HPF as feedback coefficient [106] [107], which may amplify high frequency noise and change the dynamics of the system when the time delay of digital implementation is added to the system. The proposed AD is able to avoid these problems respectively by limiting the band of the signal through the LPF and taking advantage of the higher negative gain at low frequencies and narrower transition of phase of the second order Butterworth HPF.

Compared to conventional impedance estimation and damping strategies, the proposed methodology combines accuracy, adaptability, and real-time feasibility in a unified control-oriented framework. For impedance estimation, the proposed Multi-Sine based approach introduces a deterministic and compact excitation composed of 99 sinusoids with fixed amplitude and controlled phase. This configuration allows wideband stimulation within a short time window and with minimal invasiveness. Unlike PseudoRandom Binary Sequence (PRBS) techniques, which require wideband excitation and high post-processing complexity (e.g., correlation, averaging), the Multi-Sine approach uses a fixed, fully known structure that simplifies analysis and implementation. Interharmonic injection methods often rely on sequential frequency steps or dual-frequency excitation, leading to longer injection durations and more complex synchronization. Power variation-based methods depend on changes in operating conditions and inverter control modes, reducing repeatability and controllability. Transient-based methods, while fast, require high sampling precision and are more susceptible to noise. By contrast, the proposed approach enables robust frequency-domain estimation without prior system identification or external excitation triggers. Regarding damping control, the proposed solution adopts a second-order Butterworth low-pass filter followed by a second-order Butterworth high-pass filter, applied to the grid current feedback, with parameters automatically tuned based on the estimated grid impedance. This design addresses key limitations found in other techniques. Passive damping is simple but inherently lossy and non-adaptive. Notch-filter-based damping lacks robustness to changes in the resonance frequency and may lose effectiveness under varying grid conditions. State-feedback-based approaches often require additional sensing (e.g., capacitor current or voltage) or estimators. The commonly used fixed first-order HPF damping based on grid current can amplify high-frequency noise and destabilize the system when digital delay is present. The proposed dual-filter architecture mitigates these effects, maintains phase consistency, and enhances selectivity, making it better suited for digital real-time implementation in dynamic environments.

2.4.1 Impedance Calculation Methodology

The estimation method can be divided into two consecutive steps, as shown in Figure 12. In the first step, a disturbance is injected into the grid for a limited time of 0.1 seconds. Simultaneously with the disturbance injection, a synchronous sampling of voltage and current measurements is performed. The disturbance is injected directly into the grid as an addition to the current reference entering the current loop. It is important to note that the disturbance is summed within the current loop, neither before nor after. Summing up, the disturbance before the current control may attenuate its effect, while adding it after the control loop risks losing reference control. In the second step, the collected data is analysed. Firstly, the Fourier transform of the current and voltage samples is performed. Then, the impedance is expressed as the pointwise ratio of the values obtained from the transformation. At this stage, misleading data could be present, possibly due to current or voltage spikes or unexpected harmonics that might compromise the accuracy of the measurement. Therefore, the impedance curve is filtered using the Savitzky-Golay filter to reduce the average deviation. After this data cleaning process, the curve is analyzed by an iterative algorithm, which will be presented later, to extract the parametric values of the impedance.

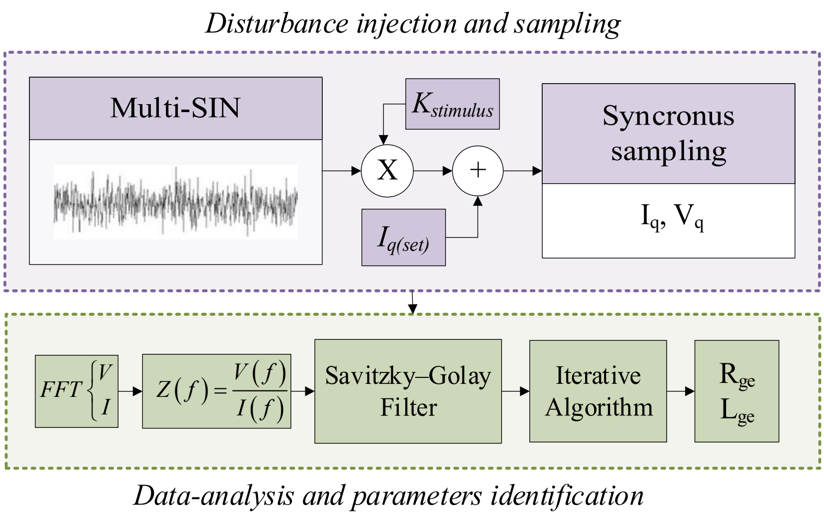

Figure 12 - Block diagram impedance estimation algorithm.

The impedance estimation algorithm is designed for computational efficiency, combining simplicity with effectiveness. As mentioned, impedance is essentially composed of three unknowns: the inductive component, the resistance component, and the frequency. Since the frequency is known, an equation with two unknowns is obtained. Subsequently, the impedance curve derived from the estimation is taken, and the values obtained from the estimation are systematically organized based on frequency, taking different points (a, b) as shown in Figure 13

$$L_{ge} = \sqrt{\frac{Z_b^2 - Z_a^2}{\left(2\pi f_{Zb}\right)^2 - \left(2\pi f_{Za}\right)^2}} \tag{36}$$

$$R_{ge} = \sqrt{Z_a^2 - \left(2\pi f_{Za} L\right)^2} \tag{37}$$

The impedance calculation method is summarized in Figure 13.

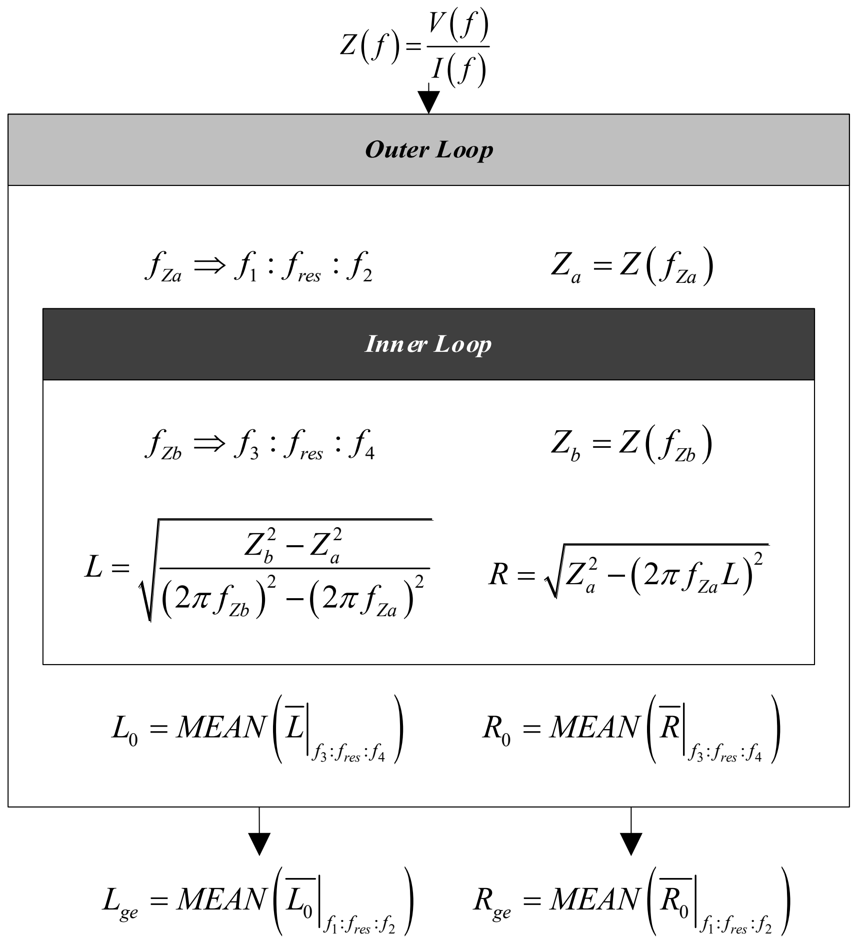

Figure 13 Impedance calculation method.

The methodology employs two nested loops involving four frequencies ($f_1 < f_2 < f_3 < f_4$) divided into two ranges: $f_1 \div f_2$ and $f_3 \div f_4$. The selected frequencies must lie within the excitation band of the Multi-Sine signal and should be distributed evenly across a range where the impedance shows dominant R-L behaviour. During each iteration of the outer loop, a dedicated value of Z_a is computed; specifically, Z_a is calculated at f_1 during the initial iteration. Progressing to the inner iterative loop while maintaining Z_a constant, the values of L and R are determined by varying Z_b within the range of f_3 to f_4. Following the iterations of the inner loop, the resulting arrays containing the values of L and R (elements from iterations spanning f_3 to f_4) serve as input for a mean operator, yielding a singular value for both L and R. Concluding the iterations of the outer loop (ranging from f_1 to f_2), two arrays are eventually formed, comprising the values of L_0 and R_0 derived from the cycles of the outer loop subsequent to the inner loop. Ultimately, an additional average operator is applied to derive the individual values for L_{ge} and R_{ge}.

2.4.2 Self-Commissioning Control System and Active Damping

This subsection explains the control system and the proposed Active Damping method on the q-axis in detail. Following, in Figure 14, a flowchart of the proposed methodology is shown. The control system for the *d*-axis is not shown since it has the same architecture of the explained *q*-axis. It is also important to highlight that the control-loop of the V_{dc} voltage is not considered in this work, since the contributions are related to the current-control scheme. The block diagram of the current-control system is presented in Figure 15.

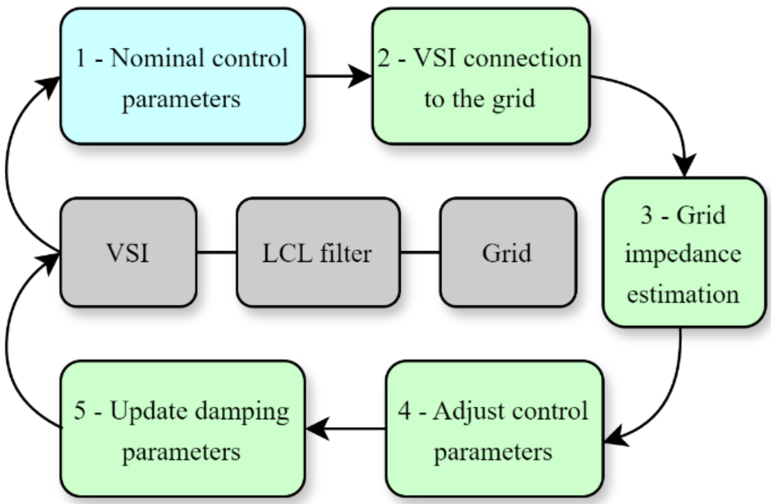

Figure 14. Proposed methodology flowchart.

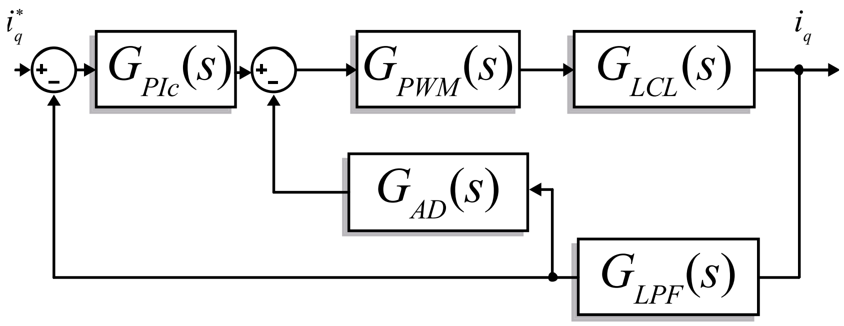

Figure 15 Current-control system block diagram.

The transfer functions in Figure 15 are defined as follows:

$$G_{PIc}(s) = K_{pc} + \frac{K_{ic}}{s} \tag{38}$$

$$G_{PWM}(s) = \frac{V_{dc}}{2}\frac{1}{sT_{sw}+1} \tag{39}$$

$$G_{AD}(s) = \frac{K_{AD}s^2}{s^2 + \sqrt{2}\omega_{AD}s + \omega^2_{AD}} \tag{40}$$

$$G_{LPF}(s) = \frac{\omega^2_{LPF}}{s^2 + \sqrt{2}\omega_{LPF}s + \omega^2_{LPF}} \tag{41}$$

where $G_{PIc}(s)$ is the transfer function of the PI current controller with gains K_{ic} and K_{pc}, $G_{PWM}(s)$ is the inverter transfer function with T_{sw} being the inverter switching period and represents the delay associated to the digital implementation of the system, $G_{AD}(s)$ is the II-order Butterworth HPF Active Damping feedback transfer function with gain K_{AD} and cut-off frequency ω_{AD}, and $G_{LPF}(s)$ is the II-order Butterworth LPF with cut-off frequency ω_{LPF} and $G_{LCL}(s)$ (defined on the bottom of the page) is the LCL filte$_r$ transfer function between the applied voltage by the inverter and the grid current.

$$G_{LCL}(s) = \frac{1}{C_f L_{fi} L_{fg} s^3 + (L_{fi} + L_{fg})s} \tag{42}$$

The resonance frequency f_{res} taking into consideration the estimated grid impedance is defined as:

$$f_{res} = \frac{\omega_{res}}{2\pi} = \frac{1}{2\pi}\sqrt{\frac{L_{fi} + (L_{fg} + L_{ge})}{L_{fi}(L_{fg} + L_{ge})C_f}} \tag{43}$$

A. Self-Commissioning PI Controller

As mentioned previously, for the low frequency range, the capacitor can be neglected and the LCL filter can be approximated to an equivalent L filter of inductance equal to the sum of the LCL inductances plus the grid inductance, on the other hand, only the network resistance has been considered for the equivalent resistance, intrinsic resistances being negligible. Taking this into consideration for the PI design process, the equivalent synchronous inductance and resistance defined in [105] are redefined as:

$$L_s = L_{fi} + L_{fg} + L_{ge} \tag{44}$$

$$R_s = R_{ge} \tag{45}$$

These parameters are, then, applied to the following calculation of K_{ic} and K_{pc} for a given cut-off frequency ω_c (rad/s) and Phase Margin φ_{PM} (rad) [105]:

$$K_{ic} = \sqrt{\frac{R_s^2\omega_c^2\left(1+\omega_c^2\frac{L_s^2}{R_s^2}\right)Q_{amp}}{Q_c+1}}\,\frac{2}{V_{dc}} \tag{46}$$

$$K_{pc} = \sqrt{R_s^2\left(1+\omega_c^2\frac{L_s^2}{R_s^2}\right)Q_{amp}\frac{Q_c}{Q_c+1}}\,\frac{2}{V_{dc}} \tag{47}$$

$$Q_c = tg^2\left[\varphi_{PM} - \frac{\pi}{2} + Q_{phase} + atg\left(\frac{L_s\omega_c}{R_s}\right)\right] \tag{48}$$

$$Q_{phase} = atg\left(\omega_c T_{sw}\right) + atg\left(\omega_c T_{dt}\right) + atg\left(\frac{\sqrt{2}F}{1-F^2}\right) \tag{49}$$

$$Q_{amp} = \left[\left(1-F^2\right)^2 + 2F^2\right]\left(1+\omega_c^2T_{sw}^2\right) + \left(1+\omega_c^2T_{dt}^2\right) \tag{50}$$

with $F = \omega_c / \omega_{LPF}$ and Tdt being the dead-time of the Three-Phase PWM Inverter. For simplicity, the cut-off frequency in Hertz will be represented by f_c and the Phase Margin in degrees by θ_{PM}.

The cut-off frequency and phase-margin are pre-defined as input parameters for the controller design and kept the same and this self-commissioning process is executed every time a new grid impedance estimation is performed by the system for different grid impedances. The PI controller design excludes the influence of Active Damping, which is responsible for maintaining the controller's dynamics.

B. Self-Commissioning Active Damping

The Active Damping itself is, in a few words, realized by feedbacking the controlled grid current to the system through an II-order Butterworth LPF plus an II-order Butterworth HPF. The main goal of the LPF is to limit high frequencies that are not in the range of interest on the inverter's operation, avoiding amplification of noise on the HPF stage as well. Besides that, it takes advantage that the chosen control loop already considers this LPF on the feedback path of the controlled variable.

$G_{AD}(s)$ is chosen to operate with a negative K_{AD}, so the function can have a phase of 180° at high frequencies and ω_{AD} smaller than ω_{res}, so the output of the function contains adequate information on the resonance frequency range.

The chosen value of K_{AD} needs to be divided by $V_{dc}/2$ because $G_{PWM}(s)$ considers this factor to properly design the controller output between 0 and 1. It has been chosen to use K_{AD} equal to:

$$K_{AD} = \frac{20}{\frac{V_{dc}}{2}} \tag{51}$$

In this way, adequate attenuation at the resonance frequency is ensured. ω_{AD} on the other hand, must be set such as significant information at the ω_{res} range is not attenuated while being sufficiently higher than the controller cut-off frequency ω_c. ω_{AD} is defined as:

$$\omega_{AD} = K_\omega \omega_{res} \tag{52}$$

being K_ω always equal to *0.85* in this work, to ensure that the principle is respected, whereby the resonance is damped without compromising the phase.

With the presented parameters it is possible to ensure that the Active Damping system will not interfere with the controller dynamics and will attenuate the resonance.

Just like for the PI controller design, the self-commissioning Active Damping is executed every time a new grid impedance estimation is performed.

C. Stability analysis

To assess the stability of the system, the open loop transfer function of the system needs to be defined. To highlight the effect of the AD, both open loop transfer functions (with and without it) are defined respectively in Figure 16 and Figure 17.

$$G_{OL}(s) = G_{PIc}(s)G_{PWM}(s)G_{LCL}(s)G_{LPF}(s) \tag{53}$$

$$G_{OL(AD)}(s) = \frac{G_{PIc}(s)G_{PWM}(s)G_{LCL}(s)G_{LPF}(s)}{1+G_{PWM}(s)G_{LCL}(s)G_{LPF}(s)G_{AD}(s)} \tag{54}$$

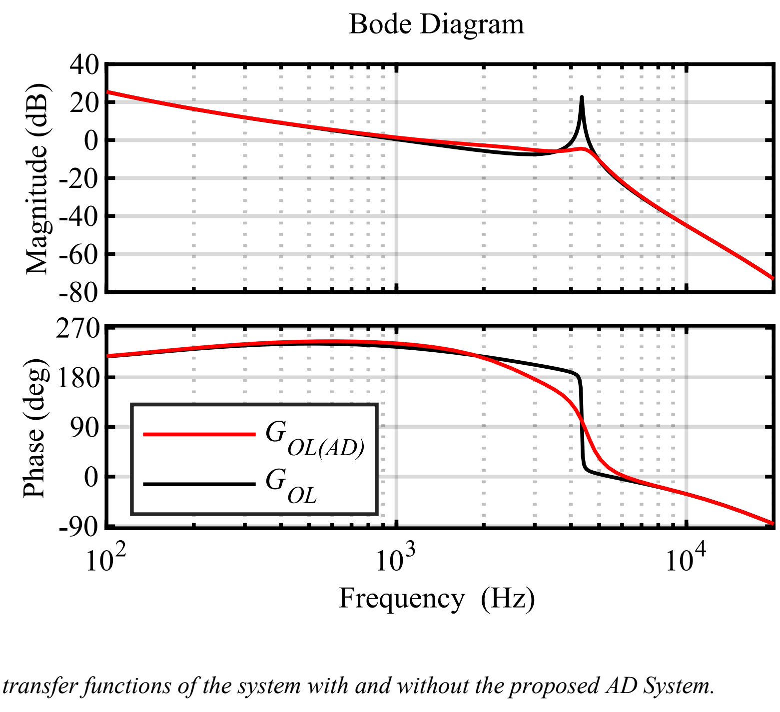

Figure 16 Open loop transfer functions of the system with and without the proposed AD System.

With the parameters defined on Table XII, $G_{OL}(s)$ and $G_{OL(AD)}(s)$ are plotted in Figure 16. From this Bode Diagram, it is possible to check that:

- The utilized control design methodology is valid. On $G_{OL}(s)$, the obtained f_c is 611 Hz and the obtained θ_{PM} is 59.9°.

- The AD damps the resonance and has a low effect in the control frequency range. The newly obtained f_c is 638 Hz and the obtained θ_{PM} is 64.7°.

Another important aspect of stability is the behaviour of the open loop system when a grid impedance is added to the system. The system must remain stable even before executing the Self-Commissioning process and while using its initial design parameters. The worst case for the controller is when the grid is purely inductive, and the considered maximum value of this inductance is equal to 2.16 mH. Figure 17 presents the Bode Diagram of $G_{OL(AD)}(s)$ when the grid inductance is equal to 2.16 mH for two cases. The one where no self-commissioning process has been engaged. Although the system is still stable, f_c is 282 Hz, and the Phase Margin is 55.3°. This case is important as the system needs stability when connected to a weak grid at start-up.

The Self-Commissioned case is when the Self-Commissioning has been realized using a grid inductance of 2.16 mH. Now the f_c is 662 Hz, and the Phase Margin is 63.8°. It is possible to notice that the resulting f_c is slightly higher than the f_c =638 Hz of Figure 16. This is since with a greater grid inductance, the resonance frequency is smaller, which implies in an ω_{AD} closer to the low frequency behaviour of the controller.

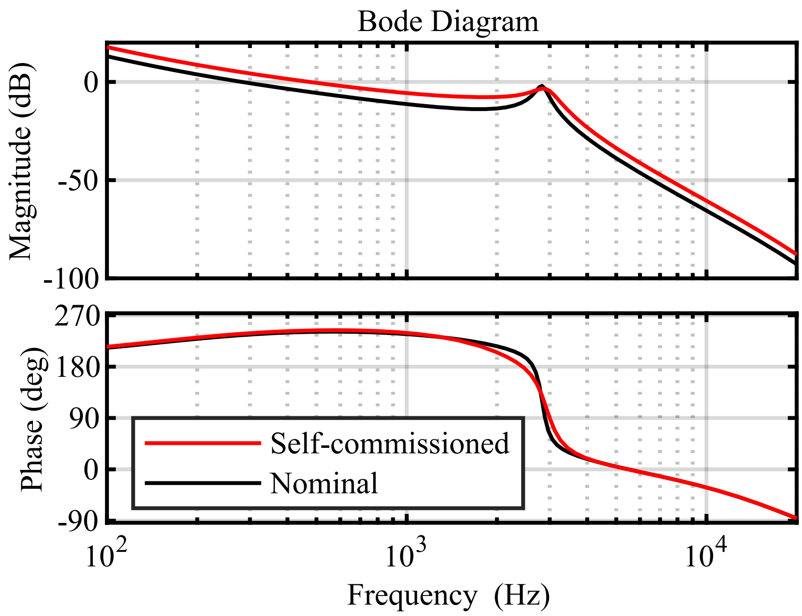

Figure 17 $G_{OL(AD)}(s)$ when the grid inductance is equal to 2.16 mH. The nominal case represents that no self-commissioning has occurred. The Self-Commissioned represents the resulting $G_{OL(AD)}(s)$ after $G_{AD}(s)$ and $G_{PIc}(s)$ are self-commissioned using the grid inductance.

D. The delay effects

One final effect that should be highlighted is the interaction between the delay in the control system introduced by its digital implementation and active damping. The delay has already been inserted into the system through $G_{PWM}(s)$. In [106], the authors propose a methodology of implementation of a first order HPF as feedback function for the AD system. As presented in the paper mentioned, the insertion of a delay in the control loop system causes the Phase Margin to decrease abruptly. Figure 18 shows a comparison between the proposed Active Damping system with the one proposed in [106] using the same PI Controller.

For this, $G_{AD}(s)$ is replaced by $-K_c/(s+\omega_h)$ and $G_{LPF}(s)$ is removed from $G_{OL(AD)}(s)$. For the AD proposed in [106], f_c is 982 Hz and θ_{PM} is 24.6°. For the AD proposed in this work, as already presented, f_c is 638 Hz and θ_{PM} is 64.7°. This shows that when considering the delay effect of digital implementation, using the proposed method has less impact on the cut-off frequency and phase margin of the controller.

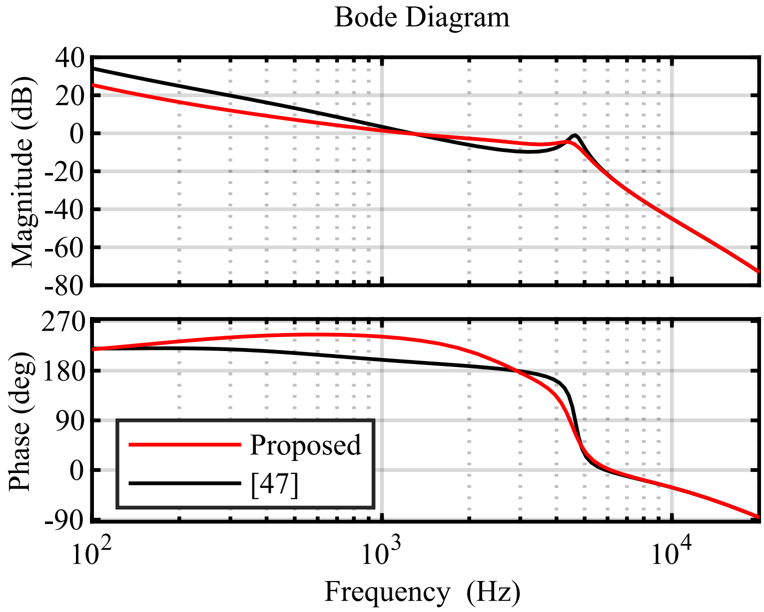

Figure 18 Comparison the proposed AD system with the proposed in [106]. *For the system in* [106], *k = 0.85, resulting, accordingly to the methodology, in $\omega_h = 4592 \cdot 2\pi$ rad/s and $k_c = 27.6449$.*

To provide a more comprehensive stability assessment, an analysis in the discrete domain has also been conducted to evaluate the effects of the delay introduced by discretization. Delay can significantly impact system stability, altering the frequency response compared to the continuous-time case. To highlight these differences, the following Figure 19 presents a comparison between the Bode diagram of the transfer function in continuous time and its discrete counterpart.

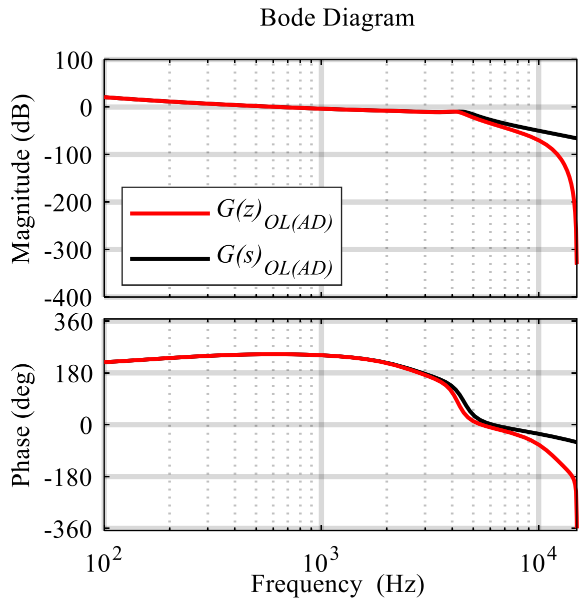

Figure 19 Comparison Bode Diagram between active damping control transfer function in continuous and discrete domain.

This analysis illustrates how the frequency behaviour changes due to discretization, allowing us to assess how the delay affects system performance but does not alter stability.

2.5 Experimental Results

In this section will be present the results of the 2.2, 2.3 and 2.4 sections covering white-noise-based impedance estimation, Multi-Sine impedance estimation, and the implementation of the damping control strategy under real operating conditions.

2.5.1 Experimental Results of estimation based on White Noise

The validation of the proposed impedance estimation methodology has been carried out using a Hardware-In-The-Loop (HIL) real-time emulator, which allows to obtain proof of the proposed algorithm, being the environment under a controlled impedance state (i.e. the grid impedance would have been unknown). The power inverter and the AC and DC side impedances have been real-time emulated by the eHS64 FPGA solver from OPAL-RT. The high-fidelity, OP4610XG Hardware-In-the-Loop platform allowed to correctly represent the power converter behaviour when connected to the grid. The control structure, the data acquisition and buffering scheme have been implemented on the PED-Board controller directly on the FPGA taking advantage of the LabVIEW graphical environment. The PED-Board is based on the System-on-Module sbRIO-9651 from National Instruments incorporating a Xilinx Zynq7020. Thanks to the FPGA implementation, data and sent directly to the on-board □Processor for real-time analysis, resulting in a very fast (i.e. on-line) estimation methodology. The experimental set-up used for the verification is shown in Figure 20.

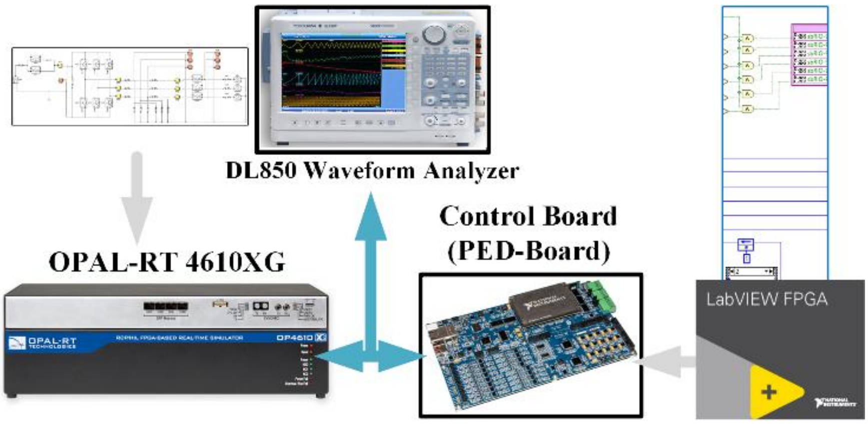

Figure 20 - HIL arrangement.

The parameters used to validate the effectiveness of the proposed method are summarized in Table III.

Table III – Simulation parameters

Parameters	Symbol	Value
WN Band-limitation	F_{lbw}	*3 kHz*
Inverter switching frequency	F_{sw}	*10 kHz*
Algorithm sampling frequency	F_{sam}	*20 kHz*
Resolution frequency	F_{res}	*2 Hz*
Number of samples	N	*10000*
Sampling duration	t_{sam}	*0.5 s*
Current percentage	$\%I_q$	*20*

The disturbance parameters selection results from a trade-off between the estimation accuracy, the computational effort, and the minimum stimulus necessary to discriminate useful information. Specifically, as t_{sam} increases, the disturbance duration, the number of samples, and the FFT computational burden FFT increase accordingly. Concerning the variation of the q-axis current reference ($\%I_q$), the detailed comparison between accuracy and magnitude of disturbance is reported.

A. AC and DC side reaction under White Noise injection

In this section the post-processing of the data acquired from the grid-side is discussed as response to the injected disturbance. This task will be necessary to estimate the desired impedance values. The voltage and current measurements on both AC and DC sides are presented, with particular attention at the time when the White Noise starts to be injected. Specifically, Figure 21 shows the q-axis currents on the AC-side before and after the LCL filter, when the WN injection starts.

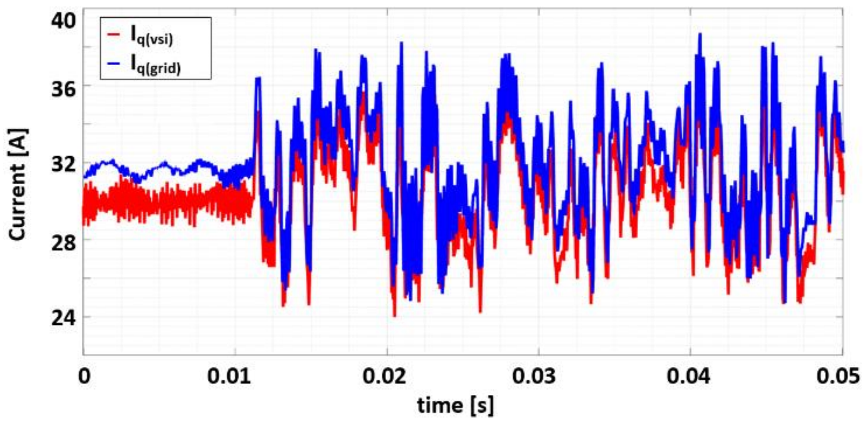

Figure 21 - Inverter-side and grid-side q-axis currents, $I_{q(vsi)}$ and $I_{q(grid)}$.

Figure 22 highlights the q-axis voltage component from the grid side 3-phase voltages, which is time-coherent with the q-axis current, representing the instant of WN injection.

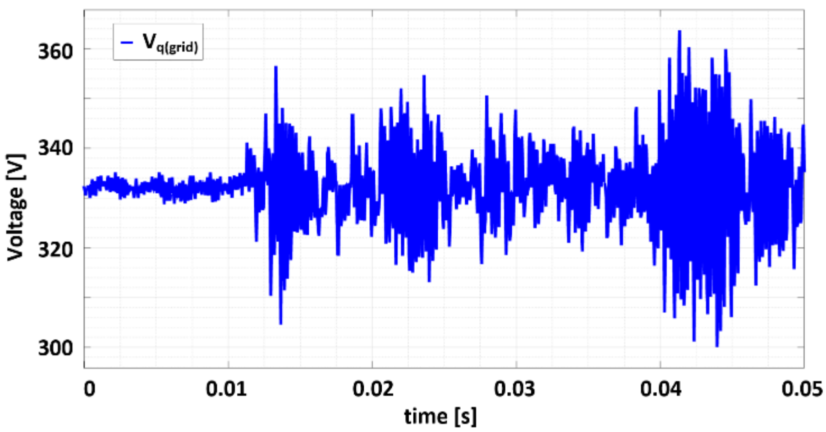

Figure 22 - Grid-side q-axis voltage, $V_{q(grid)}$.

Whereas, in Figure 23 and in Figure 24 are shown respectively the DC side current and voltage resulting from the injected WN on the AC side. Those quantities will be used for estimating both the DC and the AC impedances.

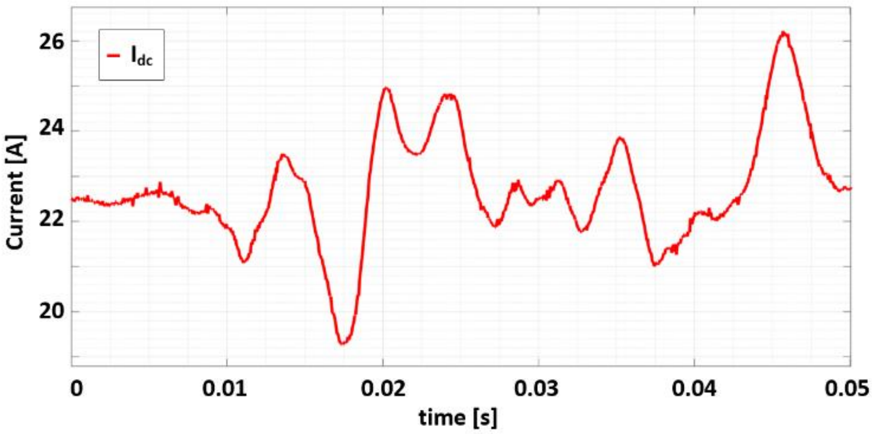

Figure 23 - DC-side current, I_{dc}.

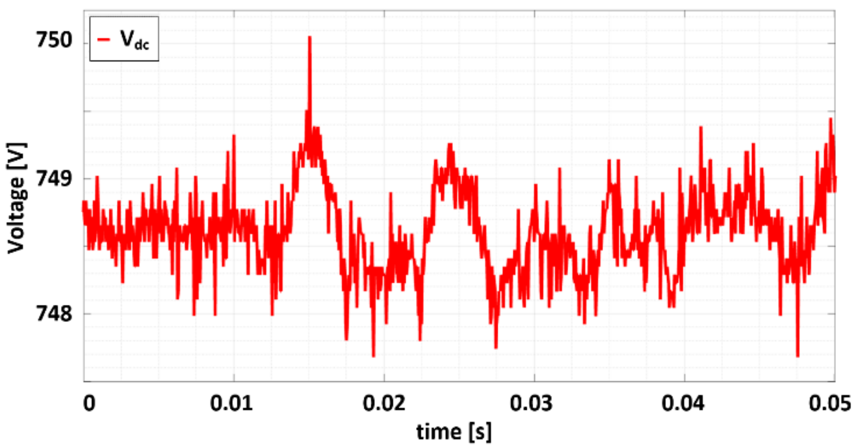

Figure 24 - DC-side voltage, V_{dc}.

B. Power Spectrum Density

The analysis of the results starts by verifying how much power of the injected disturbance is received, and then it can be considered for the analysis. To perform this verification, the PSD of the injected disturbance which is considered as the inverter side q-axis current, and the same quantity measured on the grid side, where the mean value has been removed. The results are shown in Figure 25, where the PSD is directly obtained from the control board using the LabVIEW Real-Time computational capabilities.

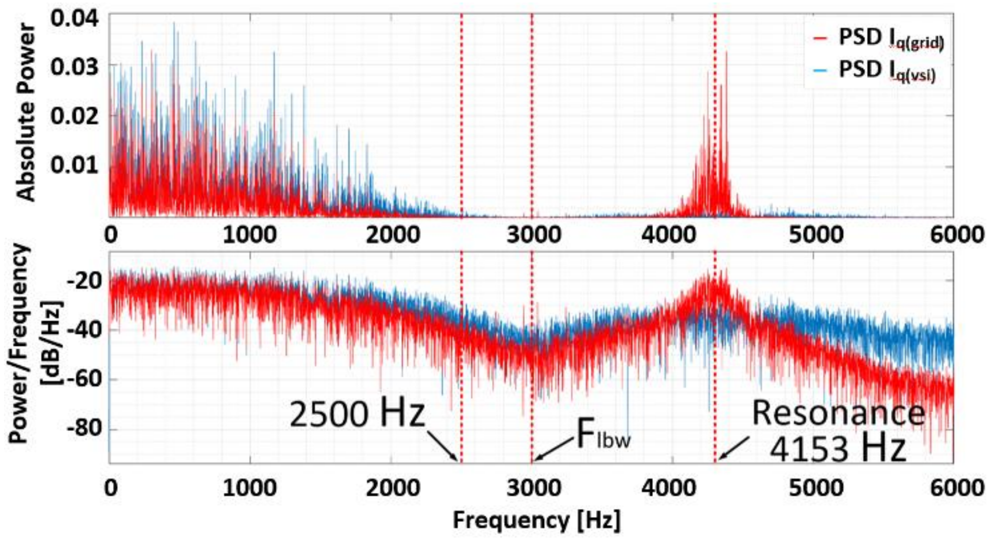

Figure 25 - Comparison of q-axis current PSD.

From the analysis of the PSD, it can be noticed that the disturbance received from the grid decreases as the frequency increases. Hence, it is expected to decrease in estimation accuracy as the frequency increases, up to the selected White Noise bandwidth (F_{lbw}). Figure 25 provides additional information to be noticed, which is of interest when the inverter draws or pushes power to the grid. The highlighted grid resonance which is achieved by the proposed method from the PSD, gives the knowledge of the frequency limit in the impedance estimation, and, more important, provides the grid resonance to be damped to about any possible instability or oscillations. On the AC-side, the resonant frequency f_0 is determined by the filter and grid inductances and the filter capacitance. With reference to the parameters' nomenclature and values reported in Table II, the value for f_0 can be numerically evaluated as:

$$f_0 = \frac{1}{2\pi\sqrt{\left(L_g + L_{fg}\right)C_f}} \approx 4153 Hz \tag{55}$$

As it can be observed, the value of the calculated f_0 is perfectly agrees with the obtained PSD, where the amplification of the injected signal can be clearly recognized. With a similar procedure, the PSD has been evaluated for the acquired DC-side current, and the result is shown in Figure 26. It can be noticed that above *250 Hz* the power level tends to smooth out, which is the common behaviour after the circuit resonance. It will then limit the maximum frequency of the impedance estimation, that can be assumed to be accurate right up to *250 Hz*. However, the resonance highlighted by the PSD, which is calculated in real-time by the control platform, allows to determine in a very accurate way any possible instability or DC current oscillations which are triggered be the resonance. The DC-side resonance is triggered by the interaction between the line inductance and the inverter DC-bus capacitors, which exhibit a common value that is larger than the AC filter capacitance, resulting in a lower resonant frequency. In the specific case, with reference to the system parameters reported in Table II, it can be evaluated as:

$$f_0 = \frac{1}{2\pi\sqrt{L_{dc}C_i}} \approx 142Hz \tag{56}$$

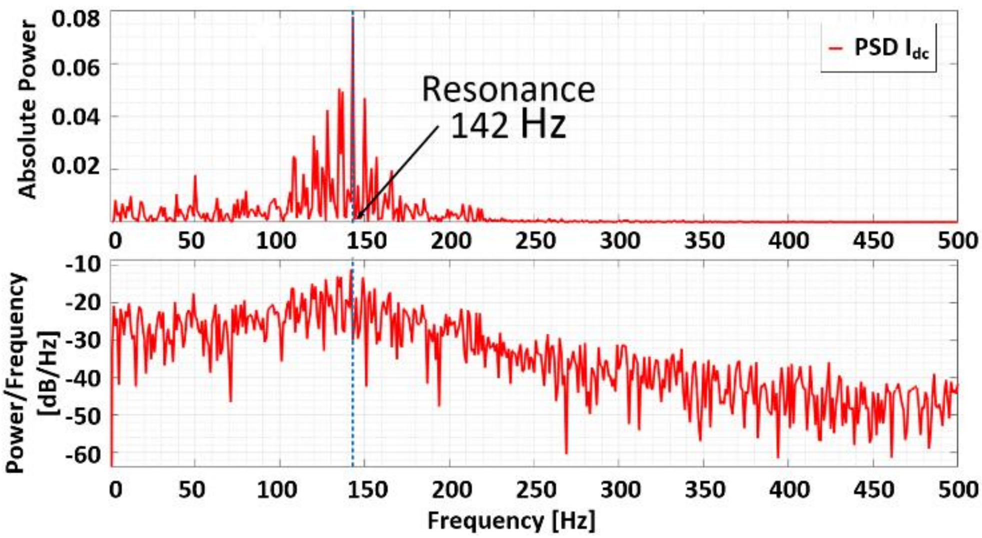

Figure 26 - DC-side current PSD.

The results obtained by performing the estimation on both AC and DC-side are reported in this section. shown the results related to the estimation of the AC impedance. Specifically, it highlights the impedance samples which are directly achieved from the data, the estimation curve obtained with the proposed methodology and finally, the actual frequency behaviour of the grid impedance. The accuracy in the estimation process exhibits a behaviour which results in an incremental error as the frequency increases. It can be noted that the estimation error increases when the frequency approaches the F_{lbw} value.

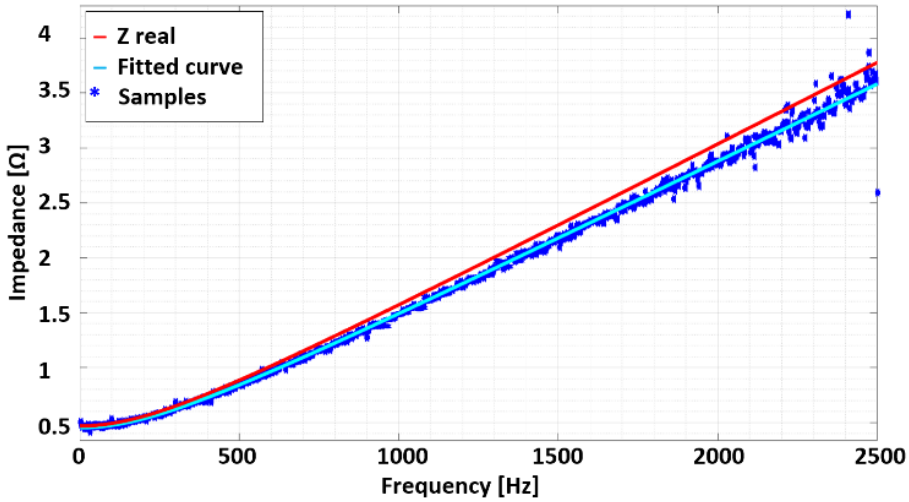

Figure 27 - AC-side impedance curve vs. frequency.

This result is in accordance with respect to the PSD of Figure 25; in fact, the received disturbance signal exhibits a frequency defendant power, which reduce the feedback and then the estimating capabilities. However, even if the estimation process must deal with that behaviour, Figure 28 shows the percentage of the estimation error with respect to the frequency. The validity of the reported approach is proved from the relatively small error vs. the estimation frequency, which makes the analytical derivation useful for industrial applications. Finally, the AC impedance estimated final values obtained with both methods are reported in Table IV, jointly with the related estimation error. It shows the effectiveness of the illustrated approach, especially the double averaging and double samples scan procedure of Figure 9, which results in a lower estimation error.

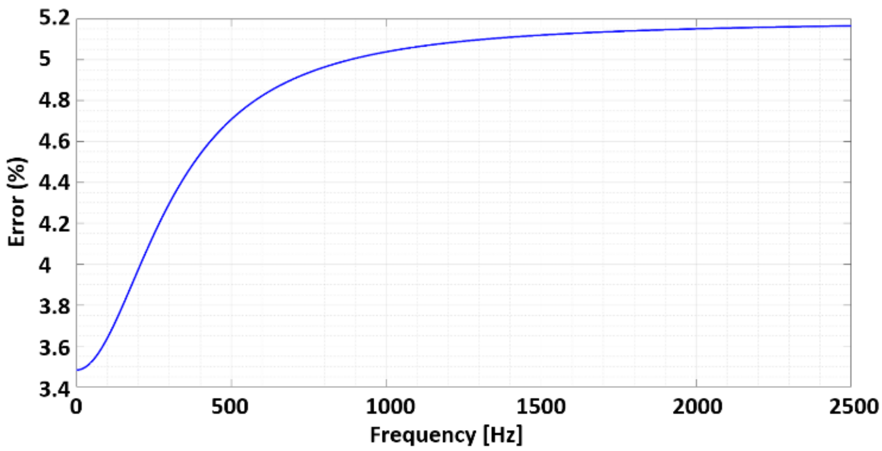

Figure 28 - AC-side impedance estimation error vs. frequency.

Table IV - AC-side impedance estimation results

	Estimation		Error (%)	
Method	LSQ	Proposed	LSQ	Proposed
R [Ω]	0.4527	0.4574	3.4825	2.4724
L [μH]	226.31	227.27	5.1920	4.7877

The results obtained for the DC-side impedance estimation are shown Figure 29, where the actual impedance frequency behaviour is compared with the estimated points and finally, with the proposed curve fitting. As already mentioned and illustrated in the Power Spectrum Density of Figure 26, the feedback noise power from the DC-side is circumscribed up to *250 Hz* and consequently the estimation tends to diverges approaching that frequency as clearly shown in Figure 29. Figure 30 reports the DC percentage error in the estimated impedance. It is monotonic, and it increases with frequency due to the low-pass behaviour of the DC system, which reduces the signals received as feedback.

summarizes the estimated resistive and inductive parts of the DC-side impedance, obtained with the suggested arithmetical method. The estimation error with respect to the LSQ curve fitting is lower, emphasizing the behaviour of the proposed methodology.

Table V - DC-side impedance estimation results

	Estimation		Error (%)	
Method	LSQ	Proposed	LSQ	Proposed
R [Ω]	0.09178	0.0993	0.8221	0.6609
L [μH]	252.02	249.58	0.8077	0.1675

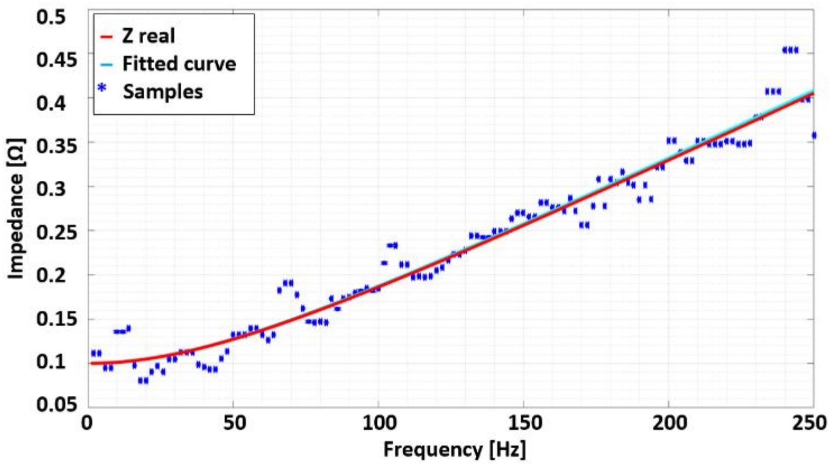

Figure 29 - DC-side impedance curve vs. frequency.

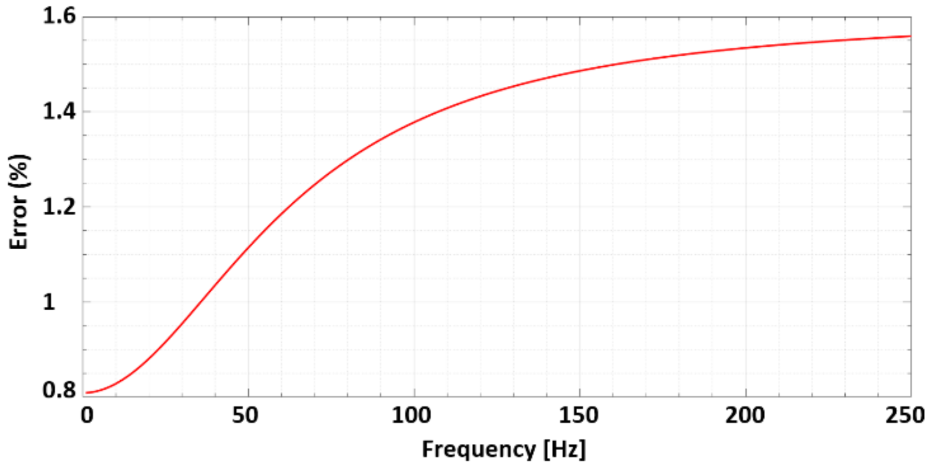

Figure 30. DC-side impedance estimation error vs. frequency.

C. *Analysis of the estimation performance*

Estimation performance has been evaluated under different operating conditions. First, the magnitude of the injected White Noise disturbance is taken into consideration. The magnitude is intended as the percentage of the noise current with respect to the steady-state value (i.e. White Noise generation is normalized between ±1). First, the curves obtained by estimating the AC-side impedance are analysed as in Figure 31. The percentage of White Noise current multiplier is changed from *10%* to *40%* with the purpose of making a comparative evaluation for the estimation performance. Z_{ac} estimation is reported up to *2500 Hz*, slightly below the F_{lbw} frequency, and it can be noticed that the accuracy does not exhibit a clear dependence by the magnitude of the injected disturbance. Moreover, even if the estimation error increases as the frequency increases, that does not seem to be linked to the noise magnitude. Accordingly, it would be more convenient to inject a smaller disturbance into the grid avoiding any possible compliance issue. With respect to the impedance estimation on the DC-side, some differences arise. Results related to the evaluation accuracy with respect to the amount of noise injected on the AC-side are reported in Figure 32. Being the DC side indirectly stimulated, acting from the AC part of the converter, when the noise magnitude is reduced at very small values, the impedance assessment suffers from low stimulus, resulting in a greater error. However, from a noise amplitude of 20%, the estimate is accurate over the entire frequency range. It can be notice that even if the DC resonance is about *142 Hz*, the PSD of Figure 26 shows that a certain amount of noise power is still available after the resonance, which helps in the estimation process.

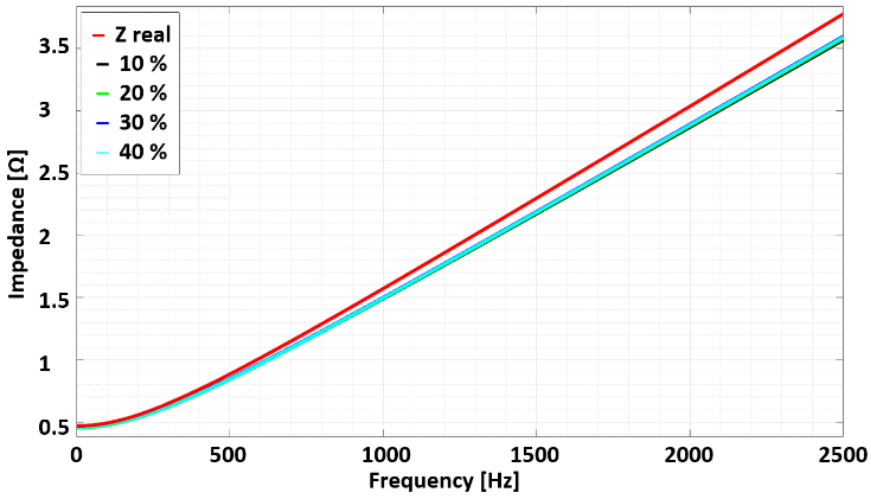

Figure 31. Estimation accuracy for the AC-side impedance as function of the noise magnitude.

This analysis shows that above a certain value of disturbance amplitude the accuracy remains almost constant while the noise injected into the grid increases. Therefore, after these considerations, it was decided to introduce the normalized White Noise multiplied by *20%* of the reference current. Table VI highlights the main characteristics of the methods reported in the literature concerning some performance indicators such as implementation feasibility, computational burden, providing separate estimation of the resistive and reactive impedance components, estimating the impedance vs. frequency, and introducing grid disturbances or reactive power even for a limited time. Features such as bandwidth constraints and simultaneous DC and AC side impedance estimation are also considered.

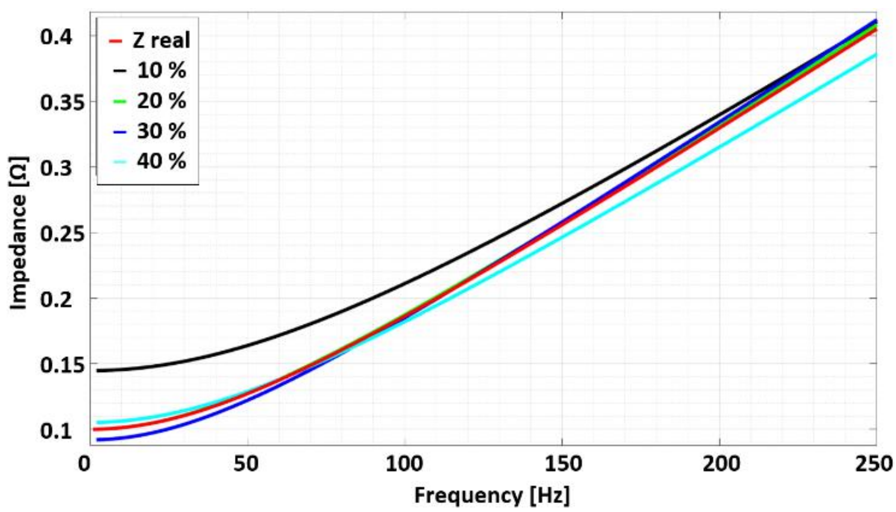

Figure 32. DC-side: comparison of estimation results.

Table VI – Preliminary Comparative Analysis

	Proposed (WN and estimation)	PRBS with proposed estimation	PRBS	PQ Variation	V and I transients	Single or double tone injected
Implementation	+	+	+	+	-	+
Computational burden	+	+	+	+	-	+
Separate R & L	+	+	-	-	-	-
Grid disturbance	-	-	-	+	-	-
Z vs. Frequency	+	+	+	-	-	-
Reactive power	+	+	+	-	+	+
Bandwidth constraints	+	-	-	-	+	+
AC and DC-side estimation	+	+	-	-	-	-

The computational time is strictly related to the calculation capacity of the used µProcessor and the number of elements in the FFT, which are strictly related to both the resolution and the maximum estimation frequencies. In the proposed case an array of 2500 samples is considered for the AC-side impedance estimation, whereas in the case of DC-side the length of the array can be reduced to 250 samples. The number of samples is strictly related to the resonance frequency, which limits the maximum usable frequency. The impedance estimation algorithm run on a dual-core ARM µProcessor operating at *666 MHz*. The calculation of the time required for estimation was performed separately for the two methods using the available µProcessor timers. Specifically, it was considered the time between the instant the impedance estimation algorithm receives the voltage and current arrays from the FPGA and the moment the results are available. Table VII summarizes the results achieved by estimating the impedance using the LSQ and the proposed method. It can be noticed that the proposed method allows to achieve a faster rate.

Table VII – Estimation of the computational burden

	Estimation time [s]	
Method	LSQ	Proposed
AC-side	3 ÷ 4	0.3 ÷ 0.4
DC-side	0.3 ÷ 0.4	0.01 ÷ 0.04

The broadband excitation produced by the disturbance allows identifying the impedance trend over a wide frequency interval within a limited observation time, which is advantageous in applications where rapid characterization is required while maintaining converter operation under realistic conditions. The resulting impedance profile, together with the automatically identified resonance frequencies on both AC and DC sides, supports tasks such as controller tuning, assessment of stability margins, and verification of filter performance. Furthermore, the reduced computational burden demonstrated in Table VII confirms the suitability of the method for embedded implementations, where memory constraints and execution time represent critical factors.

The results also highlight the intrinsic limitations of the approach. At higher frequencies, the estimation accuracy decreases due to the reduced spectral energy effectively transferred through the grid and to the limited tracking capability of the current control loop. On the DC side, the low-pass behaviour of the network constrains the frequency range in which meaningful information is available, making the method reliable only up to the resonance region. These aspects imply that the estimator provides its best performance when used to obtain a broadband and moderately accurate impedance trend, while it is less suitable for applications requiring high-precision estimation at isolated frequency points.

Based on the collected results, the method is valid under the following conditions:

- the converter must be able to track the injected disturbance within the frequency band of interest;
- the grid or DC-link conditions should remain stationary during the acquisition window;
- the signal-to-noise ratio must be sufficient across the frequencies relevant to the estimation;
- the objective is the extraction of impedance trends rather than the high-resolution estimation of narrow-band components.

Under these assumptions, the methodology provides an effective balance between implementation simplicity, computational efficiency, and estimation accuracy, confirming its applicability to real-time impedance characterization in practical converter-based systems.

2.5.2 Experimental Results of impedance estimation based on Multi-Sine

At the end of the Multi-Sine Based Disturbance section, it was stated that the maximum bandwidth is related to the cutoff frequency of the current control. However, in the analysed case, the most comprehensive scenario was shown, creating a signal that encompassed all possible frequencies, from the minimum to the Nyquist frequency of the switching frequency. This section will initially present the experimental setup, followed by the impedance estimation results. The proposed impedance estimation method was validated using a 60 kW Voltage Source Inverter (VSI) connected to an Egston grid emulator. The converter is a three-phase VSI topology with current control, linked to the grid through an LCL low-pass filter. Figure 33 and Figure 34 show the schematic of the basic setup and images of the actual components, respectively. Sampling for impedance estimation is performed at 10 kHz and synchronized with the control system's 10 kHz frequency. The DC bus of the grid emulator and the VSI is shared, while on the AC side, there is galvanic isolation between the VSI and the grid emulator through a three-phase transformer. This setup allowed for the validation of the algorithm's effectiveness in a controlled impedance environment with unknown grid impedance. Table VIII reports the setup parameters.

Table VIII - System parameters

Parameters	Symbol	Value
Grid voltage (line-to-line, RMS)	$V_a\ V_b\ V_c$	100 V
DC-link rate voltage	V_{DC}	300 V
System angular frequency	f_g	50 HZ
Algorithm sampling frequency	$\mathrm{F_{sam}}$	10 kHz
Inverter control frequency	f_{ctrl}	10 kHz
Inverter switching frequency	f_{sw}	10 kHz
LCL filter inductance grid side	L_{fg}	200 µH
LCL filter inductance inverter side	L_{fi}	450 µH
LCL filter capacitance	C_f	50 µF
LCL damping resistance	R_{Cf}	0.3 Ω
Transformer resistance	R_{tra}	0.065 Ω
Transformer inductance	L_{tra}	340 µH
Dead-Time	DT	3.3 µS
Q-axis reference current	I_q^*	20 A
D-axis reference current	I_d^*	0 A

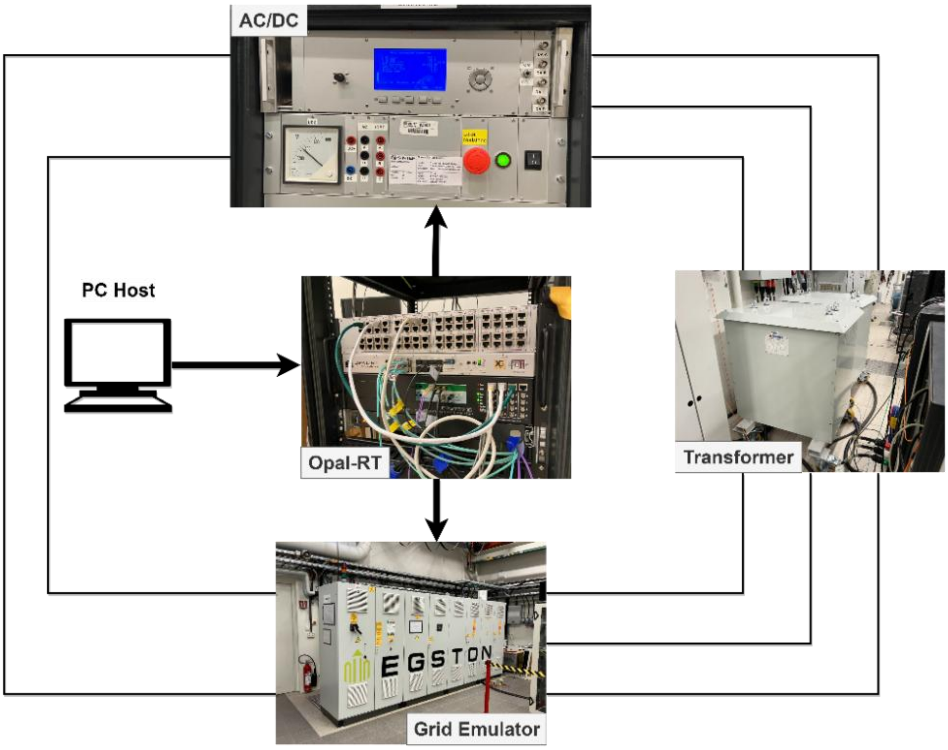

Figure 33 - Test setup graphical representation.

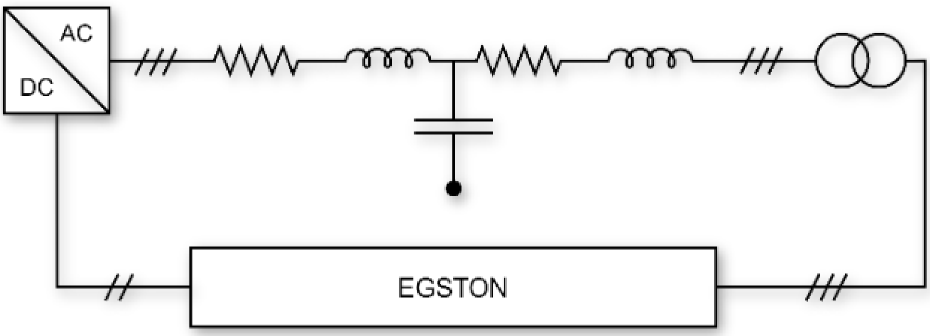

Figure 34 - Equivalent circuit of the test setup.

A. Comparison between different stimuli

To best show the advantages in using the proposed stimulus, it made a comparison among other stimuli known in the literature. PRBS [36] [47] and White Noise [87] are the most relevant to Multi-Sine Signals, as they also aim to achieve broadband impedance estimation. This similarity underpins their selection for comparative studies with Multi-Sine. The comparison criteria are as follows: all stimuli have the same RMS value calculated over the FFT of the current from 1 Hz to 5 kHz, with the frequency band approximately at the Nyquist frequency, i.e., 5 kHz. The frequency resolutions are 1 Hz and 50 Hz. Figure 35 shows the FFT of the four injected stimuli. To clarify the use of the Multi-Sine, two different stimuli named MS1 and MS50 were created. These two stimuli are composed of the sum of 5000 and 100 sinusoids, respectively. The difference lies mainly in the frequency resolution. The reason for this diversification is to demonstrate how it is possible to obtain a similar result using more or fewer sinusoids and sampling time, which will be clearer later. As can be observed from Figure 35, they all have a cutoff frequency around 5 kHz. Unlike the Multi-Sine, which has a constant magnitude, the WN and PRBS follow a descending trend. Additionally, the PRBS, by its nature, is composed of a series of delays and logic gates that, although representing a pseudo-random signal, have cutoff frequencies tied to the bits constituting the signal. Therefore, a specific cutoff frequency cannot be chosen but only approximated. For example, in this case, the PRBS signal has a cutoff frequency of $2^{12} - 1 = 4095$ Hz. Figure 36 shows the time evolution of the proposed stimuli, i.e., the values that will be added to the current reference on the active power. Figure 37 shows the FFTs of the measured currents after introducing the stimulus for one second and sampling for one second.

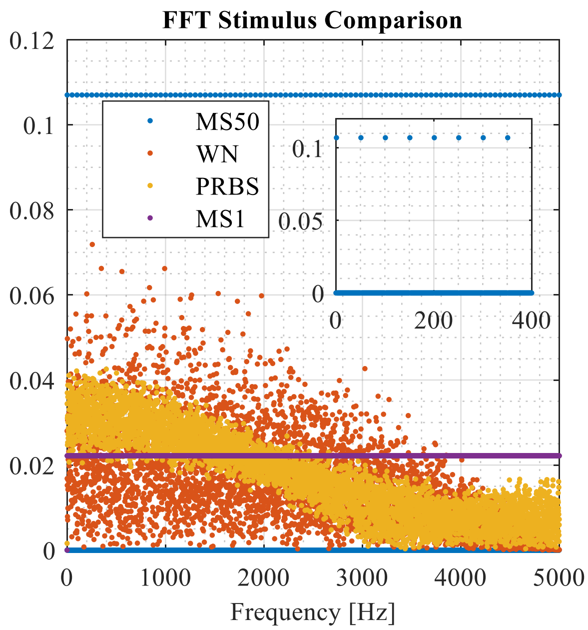

Figure 35 - FFT Stimuli: MS50 in blue, PRBS in yellow, White Noise in orange, MS1 in purple.

It is worth noting that the informational content of the MS50 signal is significantly higher than the other stimuli, given the same RMS value of the injected disturbance. This point is particularly interesting in large-scale applications where the sensor's full scale is high compared to the measurement used for estimation. Thus, since the estimation is performed on quantities significantly lower than those expected for the measurement sensors, having sample accuracy, given the same other parameters, favours better estimation accuracy. To explain better, in this application, the maximum current of the inverter is 100 A, and the signals used for the estimation are of the order of decimals, as visible in Figure 37. So, summarizing, the benefits of the proposed method can be described as follows: the main advantage derived from the use of this stimulus lies not so much in the accuracy of the estimation but in the ability to stimulate the system to the minimum necessary extent.

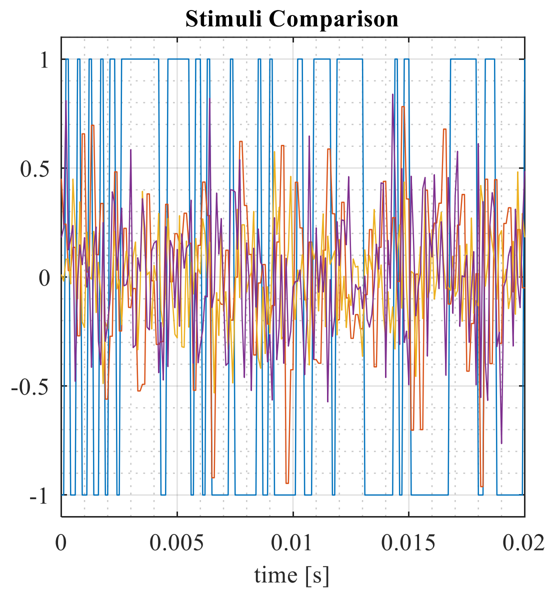

Figure 36 - Stimuli evolution: MS50 in blue, PRBS in yellow, White Noise in orange, MS1 in purple.

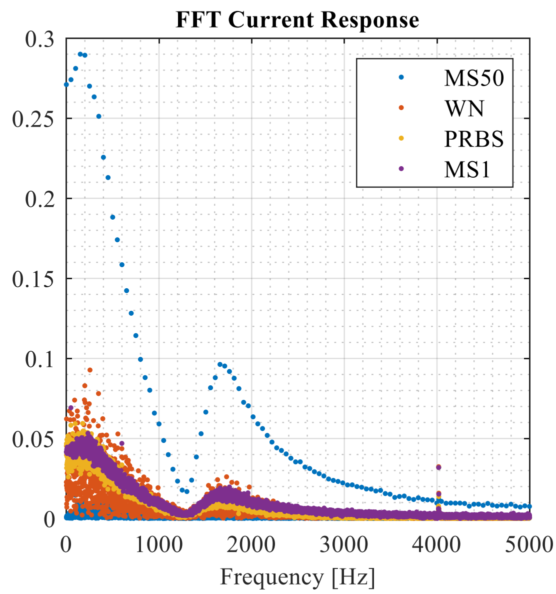

Figure 37 - FFT current response by stimuli: MS50 in blue, PRBS in yellow, White Noise in orange, MS1 in purple.

B. Impedance Estimation

In this subsection, the estimated values for different stimuli are presented and compared to their experimental values. Figure 38 shows voltage and current sampled during the stimulus injection when the system was in a steady state. Then, using these measurements, the FFTs were performed, and the phase and magnitude of the impedance were expressed. In Figure 39, the result with a resolution frequency of 50 Hz is shown, which means that 100 samples were used since the sampling was done for 0.1 seconds at 10 kHz In Figure 40, the impedance with a resolution frequency of 1 Hz is shown. This was obtained by sampling for one second, thus using 10000 samples. From the Figure 40, it is evident that the estimation performed with the MS50 stimulus calculated with a resolution of 1 Hz cannot be reliable. As previously mentioned, this is because it considers points that are not stimulated in frequency, where the FFT value is essentially tied to measurement noise. Another notable aspect from the figures is that as the frequency increases, the accuracy of the estimate decreases. This is due to the fact that the LCL filter attenuates harmonics beyond the cutoff frequency, consequently reducing their informational content.

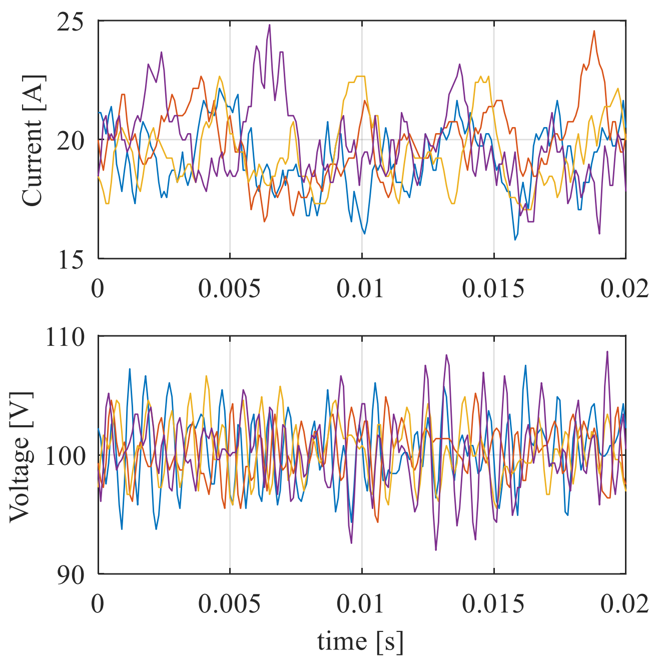

Figure 38 - Voltage and current sampling: MS50 in blue, PRBS in yellow, White Noise in orange, MS1 in purple.

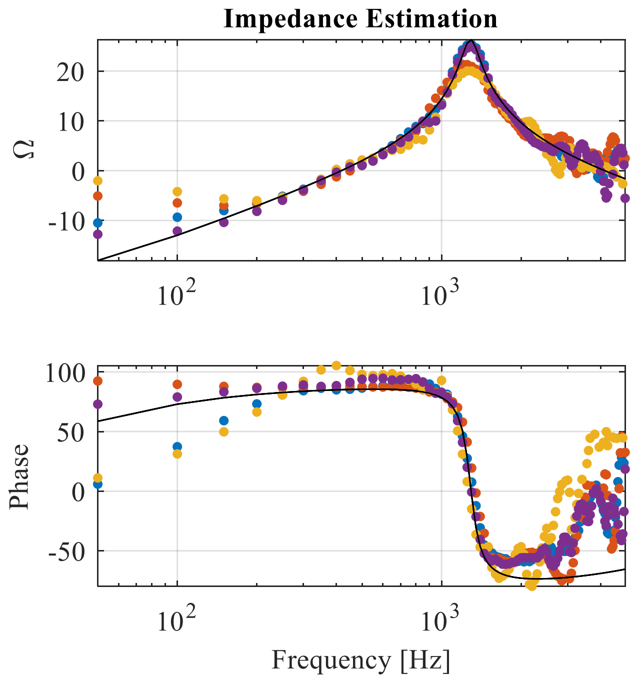

Figure 39 - Impedance estimation results - resolution frequency = 50 Hz: MS50 in blue, PRBS in yellow, White Noise in orange, MS1 in purple.

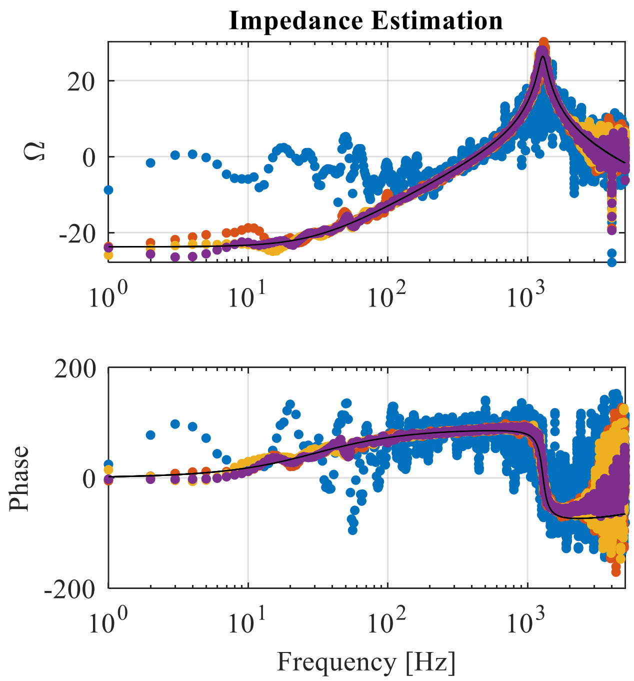

Figure 40 - Impedance estimation results - resolution frequency = 1 Hz: MS50 in blue, PRBS in yellow, White Noise in orange, MS1 in purple.

C. Multi-Sine impedance estimation and considerations

In this final section, the results obtained with MS1 and MS50 at resolution frequencies of 1 Hz and 50 Hz, respectively, are presented in Table IX and Table X. Additionally, considerations regarding impedance estimation are discussed.

Table IX - Estimation results - resolution frequency = 1 Hz

	MS 1	MS 50
R experimental [mΩ]	65	65
R estimated [mΩ]	**64**	**496**
L experimental [µH]	340	340
L estimated [µH]	**350**	**432**
C experimental [µF]	45	45
C estimated [µF]	**41**	**187**
Resonance experimental [Hz]	1287	1287
Resonance estimated [Hz]	**1282**	**1237**

Table X- Estimation results - resolution frequency = 50 Hz

	MS 1	MS 50
R experimental [mΩ]	65	65
R estimated [mΩ]	**51**	**81**
L experimental [µH]	340	340
L estimated [µH]	**385**	**368**
C experimental [µF]	45	45
C estimated [µF]	**39**	**41**
Resonance experimental [Hz]	1287	1287
Resonance estimated [Hz]	**1300**	**1300**

The objective of this study is to present a stimulus and an adaptive method tailored to specific needs. Several key points must be considered when estimating impedance:

1 Accuracy.
2 Estimation time.
3 Frequency range of estimation.
4 Computational power is available on the control board.
5 Measurement sensor range.

These factors necessitate a trade-off: the accuracy of the estimate largely depends on the quality of the measurement and the number of samples available. Increased noise in the measurement naturally leads to greater deviation from the true value, but increasing the number of samples helps average out aberrant values caused by measurement errors. However, more samples require greater computational power and longer estimation times. For instance, performing two Fourier transforms on 10000 samples versus 200 samples. Additionally, the number of samples is closely tied to the sampling frequency. Beyond this, it is necessary to consider not only the time required for estimation and computation but also for signal introduction: a resolution frequency of 1 Hz requires one second of stimulus injection and sampling, whereas a resolution frequency of 50 Hz requires 20 milliseconds. Another consideration is the maximum estimation frequency; if only the resistive and inductive components are of interest, it is advantageous to limit the stimulus bandwidth, for example, matching it to the cutoff frequency of the control loop. If, on the other hand, the resonance frequency is also to be known, it will be necessary to increase the bandwidth of the stimulus. Below, in Table XI is a summary of the effects related to the resolution frequency of impedance estimation.

Table XI - Effects of the resolution frequency

	Increasing Resolution Frequency	**Decreasing Resolution Frequency**
Number of samples	-	+
Computational effort	-	+
Estimation time	-	+
Resolution of impedance estimation	+	-
Susceptibility to measurement errors	+	-
Frequency range coverage	-	+
Data storage requirements	-	+
Impact on system stability	-	+
Real-time applicability	+	-

2.5.3 Experimental Results of active damping control application

This section will initially present the results obtained for impedance estimation, then the operation of damping, and finally the application of self-commissioning is shown. Table XIII reports the parameters used in the simulation. The proposed impedance estimation method was validated using a real-time Hardware-In-The-Loop (HIL) emulator. This allowed for proof of the algorithm's effectiveness in a controlled impedance environment (i.e., unknown grid impedance). The eHS64 Gen5 FPGA solver from OPAL-RT emulated the power inverter and the impedance in real-time with a time-step of 125 ns. The OP4610XG HIL platform accurately represented power converter behaviour connected to the grid. The control structure, data acquisition, and buffering were implemented on the PED-Board® controller's FPGA using the

LabVIEW environment. The PED-Board, based on National Instruments' sbRIO-9651 System-on-Module with a Xilinx Zynq7020, facilitated real-time analysis by sending data directly to the on-board microprocessor. This resulted in a rapid online estimation method. Figure 41 illustrates the experimental setup for verification.

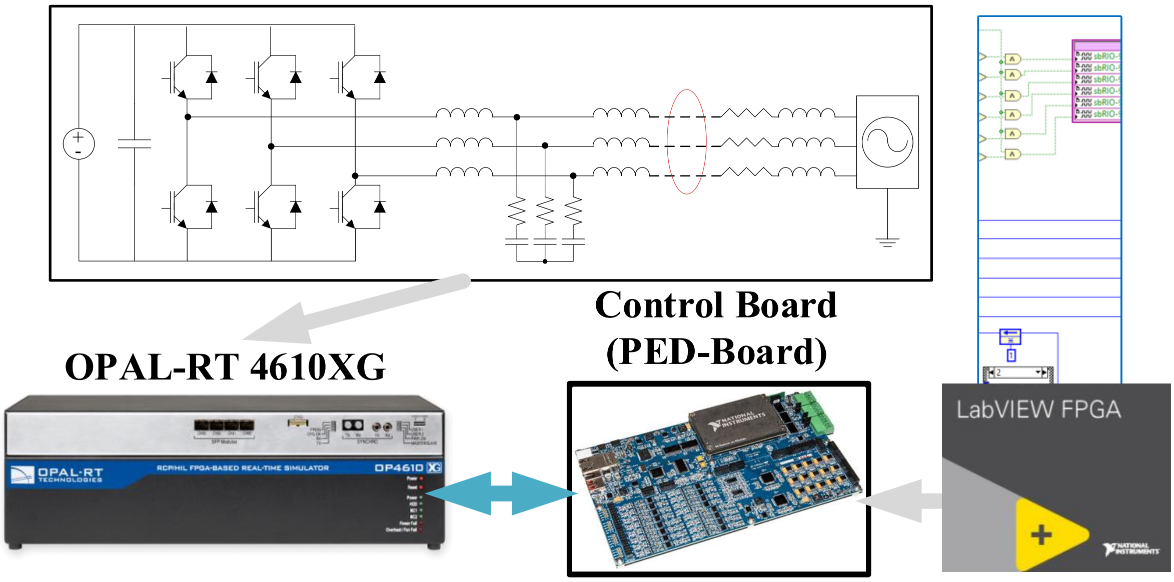

Figure 41 HIL arrangement.

Table XII - System parameters

Parameters	Symbol	Value
Multi-Sine maximum bandwidth	F_{max}	1 kHz
Algorithm sampling frequency	F_{sam}	30 kHz
Frequency resolution	F_{resol}	10 Hz
Number of samples	N	3000
Sampling duration	Δt_{sam}	0.1 s
Noise factor	$K_{stimulus}$	5
LCL filter inductance grid side	L_{fg}	500 µH
LCL filter inductance inverter side	L_{fi}	1 mH
LCL filter capacitance	C_f	4 µF
Inverter control frequency	f_{ctrl}	30 kHz
Inverter switching frequency	f_{sw}	15 kHz

A. Impedance Estimation

In this subsection, the estimated values for different grid impedances are presented and compared to their actual values. Figure 42 shows voltage and current sampled during the stimulus injection when the system was in a steady state. In this image, on one hand, the aim is to illustrate how the current appears with stimulus, and on the other hand, to demonstrate that the disturbance is not particularly intrusive given its limited duration.

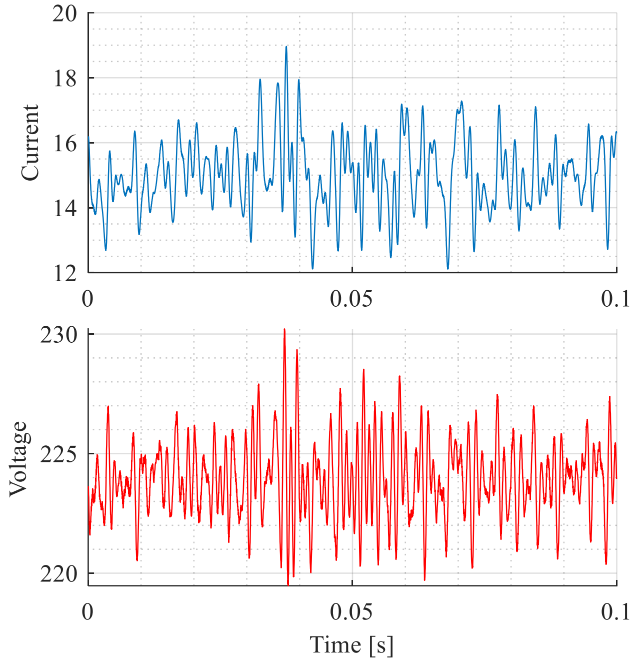

Figure 42 I_q Current and V_q voltage sampled.

Figure 43 shows the FFT of the measurements shown in Figure 42. This result demonstrates the goal of the stimulus design: introducing exactly 99 harmonics (from 10 Hz to 990 Hz), all of which contribute to the impedance estimation. So, substantially no harmonics are introduced that are not necessary for the result sought.

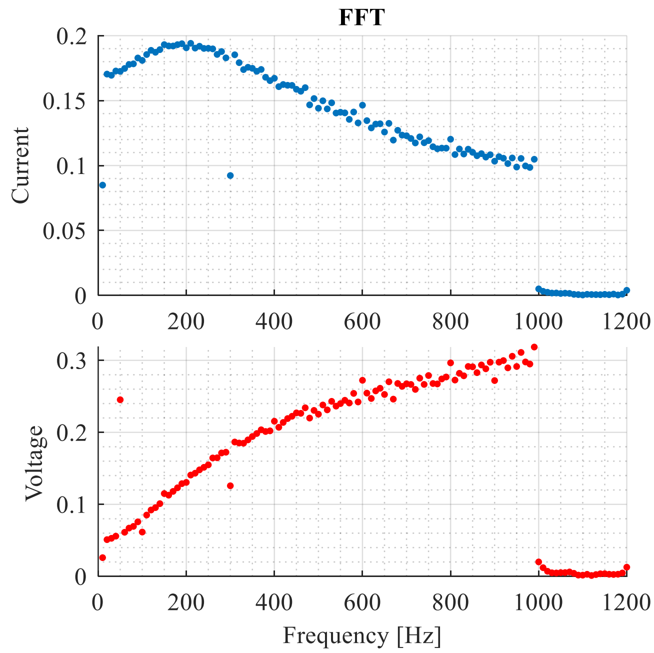

Figure 43 FFT of current and voltage used to estimate the impedance.

In order to generalize the result, two types of grids have been hypothesized, one weak and one strong, which respond to the extremes of the package of tests performed and the results are shown in Figure 44. A total of 12 tests were carried out with impedance values ranging from a strong to a weak grid network. Figure 44 depicts the estimation result in blue and yellow and the experimental impedance in red. The impedance values are the result of the ratio of the voltage and current FFTs shown in Figure 43 after being filtered as described above. This image aims to emphasize that the points used for estimating the impedance correspond to the 99 harmonics introduced by the stimulus. In Figure 45, Figure 46, in Table XIII and Table XIV are shown the experimental values and the impedance estimations results. From the results obtained as the resistance increases, the percentage error increases, the accuracy may depend on various factors, for example control, but one hypothesis is that as the resistance increases, the damping increases and the information content of the network about the resistive component decreases. On the other hand, as the inductance increases, the results improve, this can be explained by a greater information content of the network due to a higher inductance which leads to resonance at lower frequencies and greater gain.

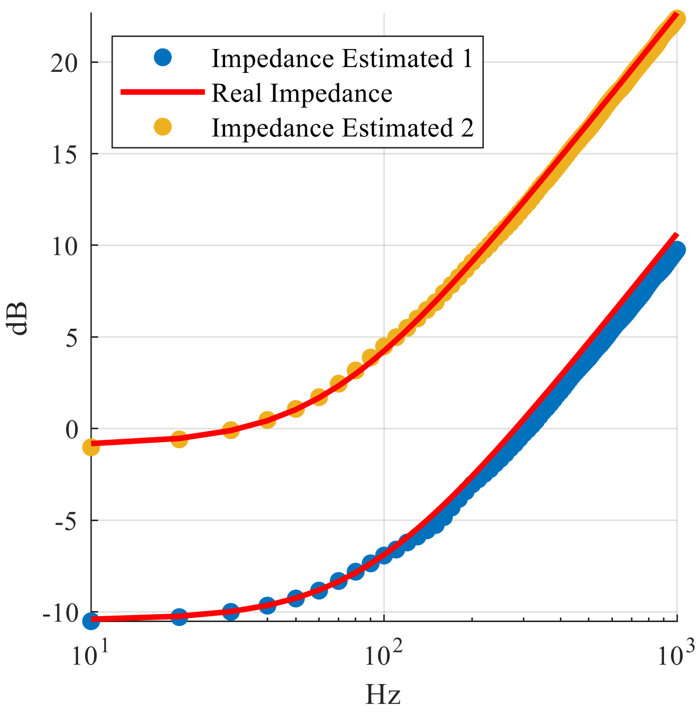

Figure 44 Impedance estimation results.

Table XIII - Inductive component results

L Actual [µH]	L Estimated [µH]	Error (%)
540	487	9.877
600	545	9.167
660	603	8.636
720	662	8.102
1080	1014	6.142
1200	1134	5.500
1320	1251	5.202
1440	1369	4.954
1620	1547	4.506
1800	1725	4.148
1980	1903	3.906
2160	2081	3.673

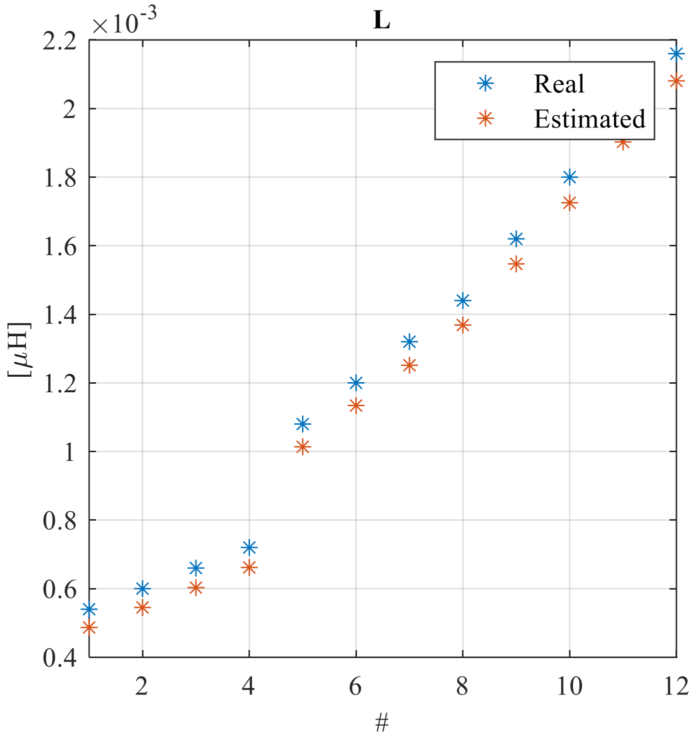

Figure 45 Percentage error of the inductive component of impedance.

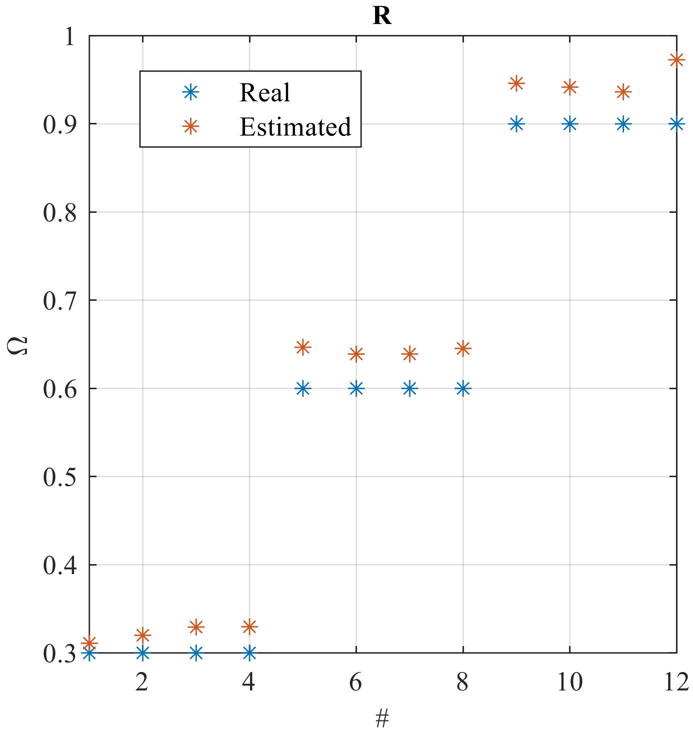

Figure 46 Percentage error of the resistive component of impedance.

Table XIV - Resistive component results

R Experimental [Ω]	R Estimated [Ω]	Error (%)
0.3	0.311	3.667
0.3	0.320	6.667
0.3	0.329	9.778
0.3	0.330	9.889
0.6	0.647	7.778
0.6	0.639	6.500
0.6	0.639	6.500
0.6	0.645	7.556
0.9	0.946	5.111
0.9	0.942	4.630
0.9	0.936	4.037
0.9	0.973	8.074

B. Self-Commissioning and Active Damping

Figure 47 presents the system current on phase and the computed q-axis current in steady state with no grid impedance considered. The system is stable thanks to the active damping system. Figure 48 depicts the same currents for the step response of the system from a current q reference change from 10 A to 15 A.

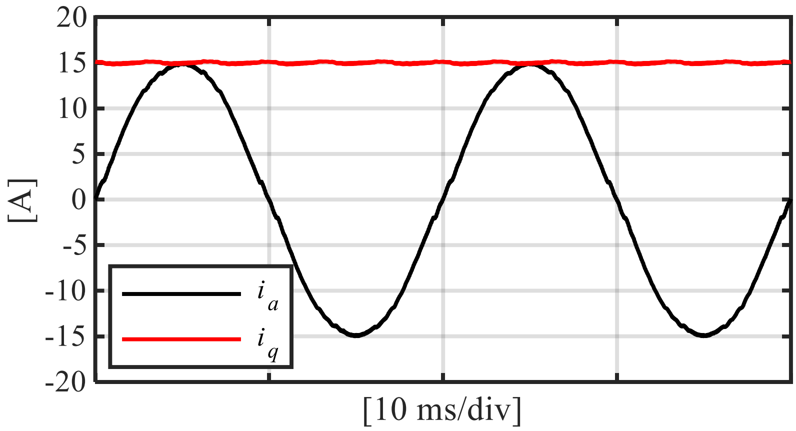

Figure 47 Grid current on phase A and i_q in steady state operation for i_q reference of 15 A.

Figure 49 and Figure 50 present the step response comparison of the system currents for different grid impedances. The Nominal case represents the step response while the controller still presents its original gains designed for the grid without impedance. The self-commissioned case presents the response of the system after the impedance estimation has been realized. In both cases, when the system presents a grid impedance and the nominal controller gains, the response is slightly slower, due to the decrease in bandwidth caused by the connection of the grid impedance, as explained before. With the self-commissioning of the controller after the grid impedance estimation, the responses again with the desired bandwidth, even though they oscillate a bit more due to the presence of the grid impedance.

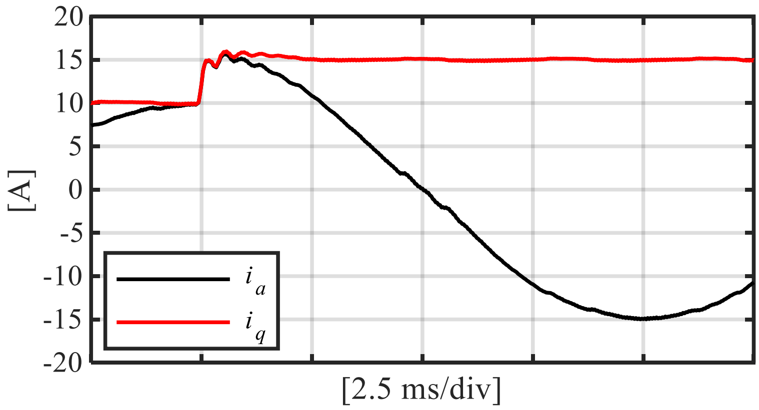

Figure 48 Step response for i_q from 10 to 15A nominal case.

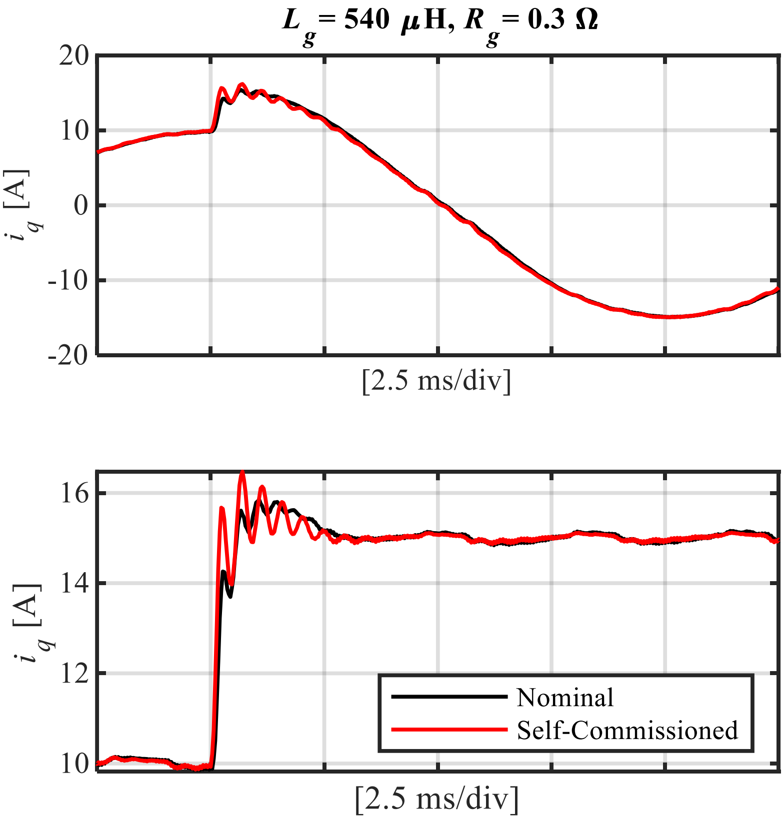

Figure 49 Step response comparison of the nominal control system and the resulting self-commissioned control for a grid impedance of 540 μH and 0.3 Ω.

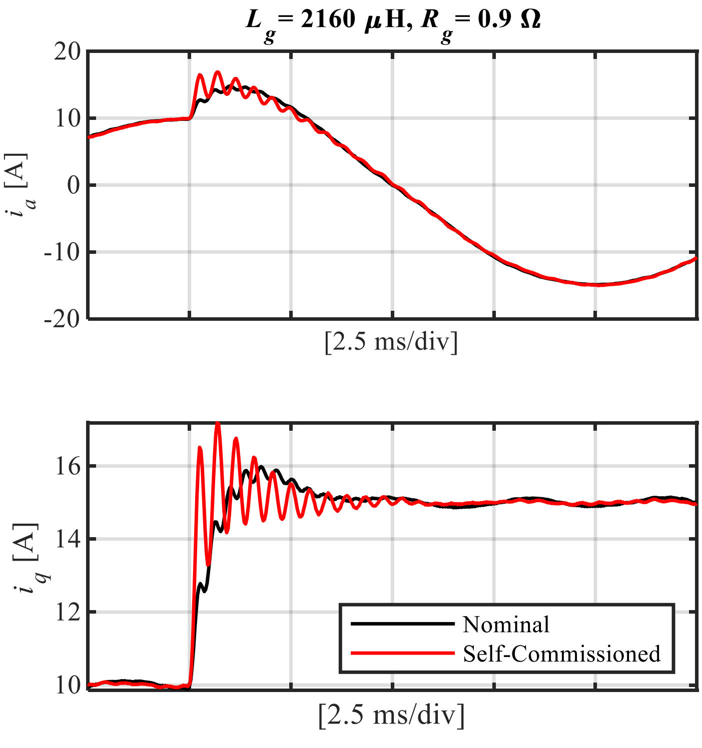

Figure 50 Step response comparison of the nominal control system and the resulting self-commissioned control for a grid impedance of 2160 μH and 0.9 Ω.

C. Experimental setup test

To further validate the proposed approach, tests were conducted on a experimental setup. The test system includes an inverter connected to the grid through an LCL filter and a 1:1 transformer for galvanic isolation. The control board used is the same as the one employed in the HIL simulations, ensuring continuity between the simulated environment tests and the experimental hardware tests. Figure 51 shows an image of the experimental setup, while Table XV lists the characteristic parameters of the system, including those of the LCL filter and the transformer.

Table XV . Experimental set up parameters

Parameters	Symbol	Value
LCL filter inductance grid side	L_{fg}	690 µH
LCL filter inductance inverter side	L_{fi}	2.2 mH
LCL filter capacitance	C_f	92 pF
LCL filter resistance grid side	R_{Lfg}	0.23 Ω
Transformer inductance	L_{tr}	440 µH
Transformer resistance	R_{tr}	0.49 Ω

The main system parameters are presented in Table XVI and Figure 52 shows the impedance estimation of the grid performed by the system. In this figure, the red curve represents the experimental impedance measured with an LCR meter, while the blue points show the values estimated by the proposed method.

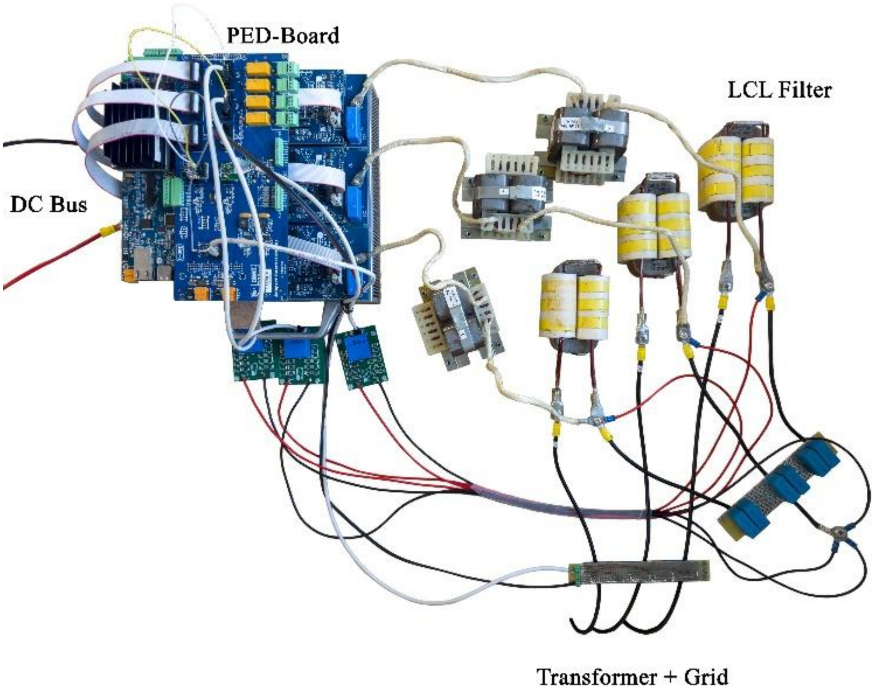

Figure 51 Experimental setup.

Table XVI - Experimental set up impedance estimation

R Measured [Ω]	R Estimated [Ω]	Error (%)
0.72	0.77	6.95
L Measured [µH]	**L Estimated [µH]**	**Error (%)**
1130	1185	4.87

A good correspondence between the estimation and the real measurement is observed, especially at the frequencies relevant for control. Subsequently, dynamic tests were carried out to evaluate the effectiveness of the self-commissioning control. Figure 53 presents a step response comparison between the system with nominal control and the self-commissioned system. It is observed that the self-commissioned system restores a faster response with the desired bandwidth, compensating for the effects of grid impedance variation. Finally, Figure 54 highlights the system's behaviour under a limit stability condition, comparing the results with and without active damping. Without damping, the system shows significant oscillations and a tendency towards instability, while with active damping, the behaviour becomes more damped and stable, confirming the effectiveness of the proposed approach.

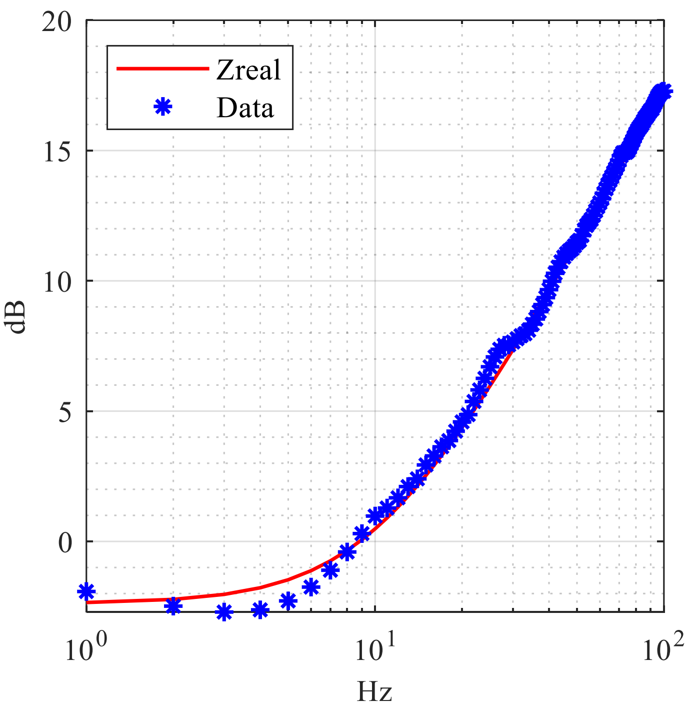

Figure 52 Experimental setup impedance estimation.

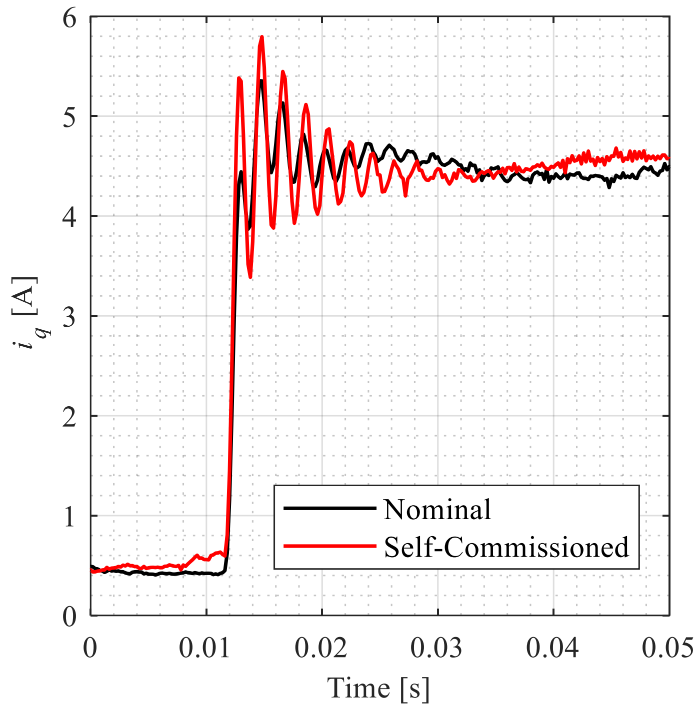

Figure 53 Step response comparison of the nominal control system and the resulting self-commissioned control in the experimental setup.

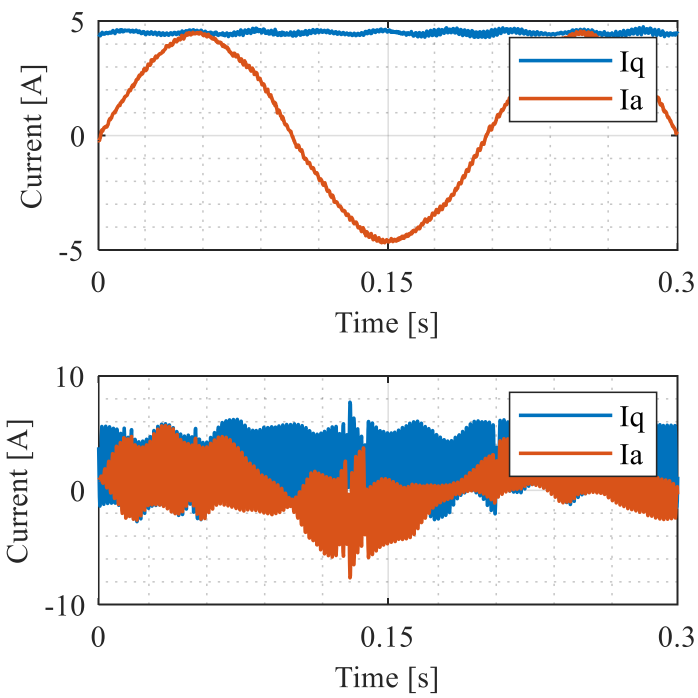

Figure 54 - Comparison between with and without damping in a limit stable condition in experimental setup.

The impedance estimation procedure allows identifying, with limited computational effort, the effective inductive and resistive grid components that directly influence the resonance location and the achievable control bandwidth. This information enables the controller to maintain a consistent dynamic response across a wide range of grid conditions, as evidenced by the step-response comparisons. The ability to restore the intended bandwidth after significant variations in grid inductance demonstrates the method's suitability for applications in which the converter may operate in networks of variable strength.

The results also show that the damping algorithm is able to stabilize the system under conditions approaching the stability limit, reducing oscillatory behaviour without requiring additional sensing hardware. The use of the grid current as feedback variable simplifies implementation and ensures compatibility with existing converter platforms. Furthermore, the experimental tests confirm that the updated damping parameters do not introduce adverse effects in nominal operating conditions, making the approach suitable for continuous operation.

However, some limitations emerge from the analysis. The estimation accuracy decreases as the resistive component becomes dominant, which reduces the information content of the current response around resonance. In addition, the damping performance is influenced by the proximity between the resonance frequency and the controller bandwidth; large shifts in resonance location may require retuning to prevent excessive phase lag. The applicability of the method is therefore linked to the assumption that the control bandwidth remains sufficiently separated from the resonance frequency and that the converter can reliably track the injected stimuli within the selected frequency range.

Within these constraints, the combination of impedance estimation, self-commissioning and active damping constitutes a practical solution for maintaining stable operation in converters connected to grids of varying impedance. The experimental tests, both in HIL and on hardware, confirm that the methodology provides predictable improvements in stability margins and transient performance, supporting its use in real-time control of LCL-filtered inverters and similar architectures.

3 Quasi-Passive Method

3.1 Introduction

Quasi-passive techniques can be interpreted as hybrid schemes that combine an observer with a conventional active impedance estimation method. The observer runs continuously in the background, processing measured voltages and currents to track the grid behaviour and to compute a simple quality or residual index that reflects how well the current impedance estimate explains the measurements. If this index remains below a predefined threshold, the system operates in a purely passive mode, and no deliberate disturbance is injected. When a grid event or slow drift causes the estimate to become outdated, the mismatch between predicted and measured quantities grows; once the residual exceeds the threshold, the active estimation routine is triggered. In this way the number of injections is reduced, and a compromise is achieved between maintaining a high-quality estimate and minimizing the occurrence of disturbance injections, at the cost of an additional detection delay associated with the observer window. The Quasi-Passive estimation approach introduced in this chapter is conceived as an auxiliary mechanism within the broader Finite Control Set Model Predictive Control (FCS-MPC) framework adopted in this work. Its purpose is to update the grid parameters required by the predictive controller without relying on continuous active excitation, thereby maintaining compatibility with normal converter operation. By providing the MPC with refreshed resistance and inductance values only when meaningful variations occur, the method contributes to preserving stability margins, ensuring adequate prediction accuracy, and mitigating harmonic amplification under time-varying grid conditions. The experimental results presented in Section 3.3 , together with the harmonic analysis reported in Subsection D, illustrate how this event-driven update mechanism supports the controller in sustaining the expected dynamic and steady-state behaviour.

3.2 PQ variations

The estimation method is based on measuring three operating points of the system. These points are generated by applying small, intentional variations ΔP and ΔQ to the inverter's reference signals. The impedance is then computed by analysing the resulting changes in voltage and current in the dq reference frame. The grid impedance is assumed to be represented by an RL model:

$$Z_g = R_g + j\omega L_g \tag{57}$$

Where R_g and L_g are the experimental grid resistance and inductance at the PCC. The inverter's reference currents in the dq reference frame are computed from the perturbed power references as:

$$\begin{bmatrix} I_d^* \\ I_q^* \end{bmatrix} = \frac{2}{3} \cdot \frac{1}{V_d^2 + V_q^2} \begin{bmatrix} V_d & -V_q \\ V_q & V_d \end{bmatrix} \begin{bmatrix} P^* - \Delta P \\ Q^* + \Delta Q \end{bmatrix} \tag{58}$$

Three snapshots of the system response are collected at times Δt_1, Δt_2, and Δt_3, corresponding to the nominal, perturbed active power, and perturbed reactive power operating points. The total estimation interval is $\Delta T = \Delta t_1 + \Delta t_2 + \Delta t_3$. The impedance is estimated using the complex ratio of the change in voltage to the change in current in the positive sequence dq components:

$$Z_g^+ = \frac{\Delta V_{dq}^+}{\Delta I_{dq}^+} \tag{59}$$

From the real and imaginary parts of Z^+_g, the following quantities are computed:

$$R_{est} = \Re \left[\frac{\Delta V_{dq}^+}{\Delta I_{dq}^+} \right] \tag{60}$$

$$L_{est} = \frac{1}{\omega} \Im \left[\frac{\Delta V_{dq}^+}{\Delta I_{dq}^+} \right] \tag{61}$$

Expanded expressions in the dq reference frame are:

$$R_{est} = \frac{\Delta V_d \cdot \Delta I_d + \Delta V_q \cdot \Delta I_q}{\Delta I_d^2 + \Delta I_q^2} \tag{62}$$

$$L_{est} = \frac{1}{\omega} \frac{\Delta V_q \cdot \Delta I_d - \Delta V_d \cdot \Delta I_q}{\Delta I_d^2 + \Delta I_q^2} \tag{63}$$

The voltage and current used for the estimation are measured across the filter capacitor (V_c) and through the grid-side inductor (i_o). Thus, the estimated impedance corresponds to the series connection of the grid impedance and the grid-side inductor of the LCL filter:

$$Z_{est} = \left(R_g + R_2\right) + j\omega\left(L_g + L_2\right) \tag{64}$$

where: R_2 and L_2 are the known resistance and inductance of the filter inductor on the grid side. The experimental grid parameters are obtained by subtracting the known filter components:

$$R_g = R_{est} - R_2 \tag{65}$$

$$L_g = L_{est} - L_2 \tag{66}$$

However, the control algorithm directly adopts the compensated values, which coincide with the actual grid parameters under ideal conditions.

It is also important to note that the proposed estimation method assumes quasi-stationary conditions during the perturbation interval $\Delta T = \Delta t_1 + \Delta t_2 + \Delta t_3$. Fast variations in active or reactive load that occur during this window could potentially compromise the accuracy of the impedance estimate, as the power deviations would not be due solely to the applied ΔP and ΔQ. However, the short duration of the estimation sequence (on the order of a few milliseconds) ensures sufficient immunity to typical load transients in practical grid-tied systems.

Trigger Conditions:

The estimation routine is enabled only when specific operating conditions shows the occurrence of a significant change in the grid impedance. Two independent parameters are evaluated:

- Voltage deviation: The RMS grid voltage is continuously monitored and compared to its nominal reference. The deviation is computed as:

$$Error = \left| mean\left(V_{gRMS} - V_{nom} \right) \right| \tag{67}$$

  The estimation is triggered if:

$$Error > Error_{\max} \tag{68}$$

  The resistance of the grid R_g is particularly sensitive to variations in the voltage of the grid, therefore, voltage fluctuations directly influence its accuracy.

- Total Harmonic Distortion of the phase-A current: The THD of the phase-A output current $i_{o,a}$ is used as an indicator of inductive impedance variations. It is computed over one grid period:

$$THD_{io,a} = \frac{\sqrt{\sum_{n=2}^{N} I_{o,a,n}^2}}{I_{o,a,1}} \cdot 100 \tag{69}$$

The estimation is triggered if:

$$THD_{io,a} > THD_{\max} \tag{70}$$

Variations in L_g are generally correlated with an increase or decrease in the output current THD, making it a reliable indicator of inductive changes in the grid.

The routine starts if at least one of the two conditions is satisfied:

$$Error > Error_{\max} \quad \vee \quad THD_{io,a} > THD_{\max} \tag{71}$$

Once activated, the step-based procedure is executed, updating R_{est} and L_{est} in the control model. The selection of thresholds Error max and THD max plays a crucial role in balancing the responsiveness and stability of the estimation routine. If these thresholds are set too low, the system may trigger unnecessary estimations due to minor transients or measurement noise; if these thresholds are set too high, it may fail to react promptly to significant grid variations. In this work, the thresholds were empirically tuned to ensure that the estimation is activated only when waveform degradation or voltage shifts materially affect the control performance. This trade-off was validated through multiple test scenarios to ensure robustness without excessive unnecessary trigger

3.3 Experimental Results

The effectiveness of the proposed impedance estimation and self-tuning MPC strategy is validated through two levels of experimental testing. First, a Real-Time Hardware-In-the Loop (HIL) setup is used to test the control algorithm under various dynamic scenarios. Then, the method is evaluated on a physical inverter connected to the actual grid. Finally, all results are summarized to highlight accuracy and reliability across different conditions.

A. HIL-Based Validation

To validate the proposed impedance estimation method in a real-time environment, a Hardware-in-the-Loop (HIL) setup was implemented using two Typhoon HIL platforms:

- Typhoon HIL 606: simulates the complete grid-tied inverter system, including power stage, LCL filter, grid, and load, and provides real-time measurements of capacitor voltage and output current.
- Typhoon HIL 402: executes the FCS-MPC algorithm and the impedance estimation logic (coded in C) and returns control signals to the simulated hardware.

The two platforms are interconnected via dedicated breakout boards, ensuring deterministic closed-loop behaviour, Figure 55. The nominal parameters used in the HIL setup are reported in Table XVII.

The estimation routine is activated based on one of two conditions: a voltage deviation from the nominal value (Error> Error max), or a rise in the total harmonic distortion of the phase-A output current (THD i_{oa} > THDmax). A timeout of 1 s is introduced between two consecutive estimations to avoid unnecessary retriggering.

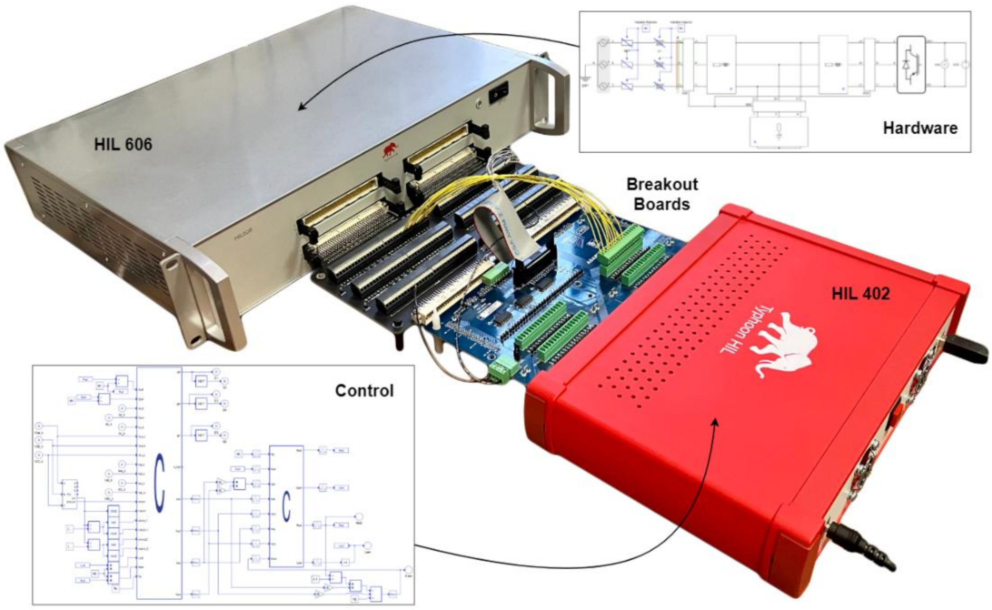

Figure 55 - HIL architecture: Typhoon 606 simulates the power stage and measurement blocks, while the Typhoon 402 runs the FCS-MPC controller and the impedance estimator.

Table XVII - Nominal parameters of the system

	LCL Filter		
L_1	5 mH	L_2	155 μH
R_1	0.16 Ω	R_2	0.08 Ω
C_f	5 μF	R_d	10 Ω
	System Parameters		
f_0	50 Hz	f_s	40 kHz
V_{grid}	230 V_{rms}	V_{dc}	440 V_{dc}
Load		***Grid Impedance***	
P^*	10 kW	R_g	0.24 Ω
Q^*	0 VAr	Lg	440 μH
	Impedance Estimation Trigger Parameters		
THD_{max}	15	$Error_{max}$	3

Case 1 – Initial Estimation at Startup (HIL):

In this first test scenario, the system is powered up with an initial grid impedance of $R_g = 0.24$ Ω and $L_g = 440$ μH. Shortly after startup, a voltage deviation occurs due to a mismatch between the assumed and actual grid model. This causes the measured voltage error to exceed the predefined maximum threshold, thereby triggering the impedance estimation routine. The estimation algorithm promptly reacts to the trigger and is able to identify the correct impedance values with high fidelity. Figure 56 provides a detailed view of the internal variables involved in the process: it plots the measured and threshold values for the voltage error and the THD of the output current, as well as the evolution of the estimated resistance and inductance compared to their experimental values. This figure not only confirms the accuracy of the estimator but also highlights the responsiveness of the dual-trigger mechanism, which allows activation only under relevant grid variations. Once the estimation is complete and the new R_g and L_g values are updated in the internal model, the controller quickly recovers optimal operating conditions. Figure 57 shows the output current and the voltage across the filter capacitor before and after the estimation update. The waveforms clearly remain sinusoidal and stable throughout the transition, with a noticeable improvement in harmonic quality after the model correction, as reflected in the reduction of current THD. This result validates the ability of the proposed method to operate non-invasively, maintain power quality, and ensure real-time adaptive control during system transients.

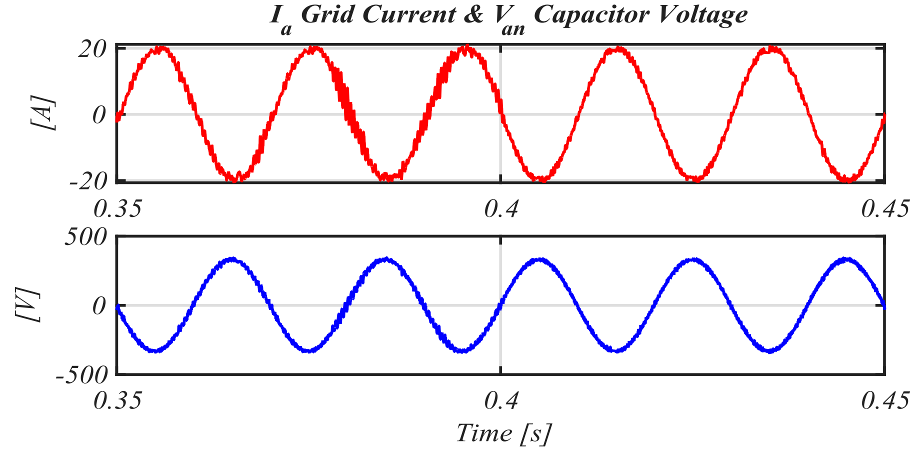

Figure 56 - Case 1 (HIL): Estimated parameters and trigger variables at startup.

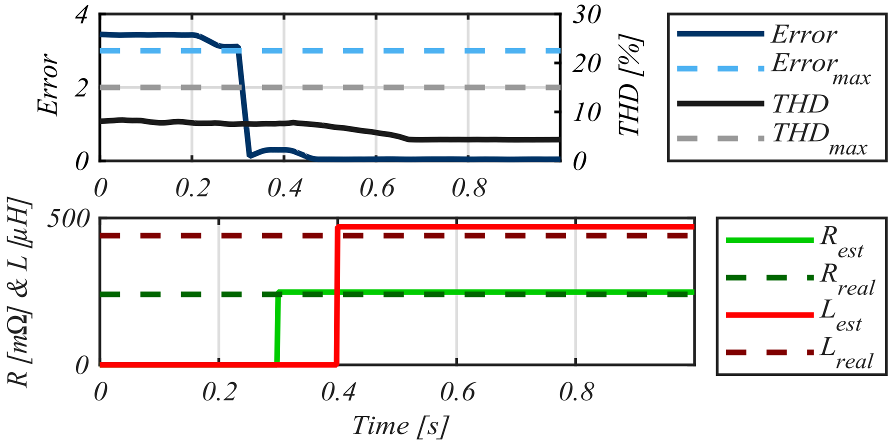

Figure 57 - Case 1 (HIL): Grid current and capacitor voltage after startup. non-invasively, maintain power quality, and ensure real-time adaptive control during system transients.

Case 2 – Resistive Step (HIL):

In this test, a step change is introduced on the grid resistance, increasing R_g from 0.24 Ω to 0.5 Ω, while the inductance remains constant at L_g = 440 µH. The increased resistive component leads to a more significant voltage drop across the PCC, which is promptly detected by the voltage error monitor. Once the measured error exceeds the predefined maximum threshold, the estimation routine is triggered. The algorithm performs the estimation and successfully detects the new resistance value, updating R_g in the predictive model used by the MPC controller. Since the inductance has not changed, the system's dynamic behaviour and harmonic profile are only marginally affected by the resistive step. This is reflected in the waveform of the output current and capacitor voltage, shown in Figure 58, which remain essentially undistorted throughout the transition.

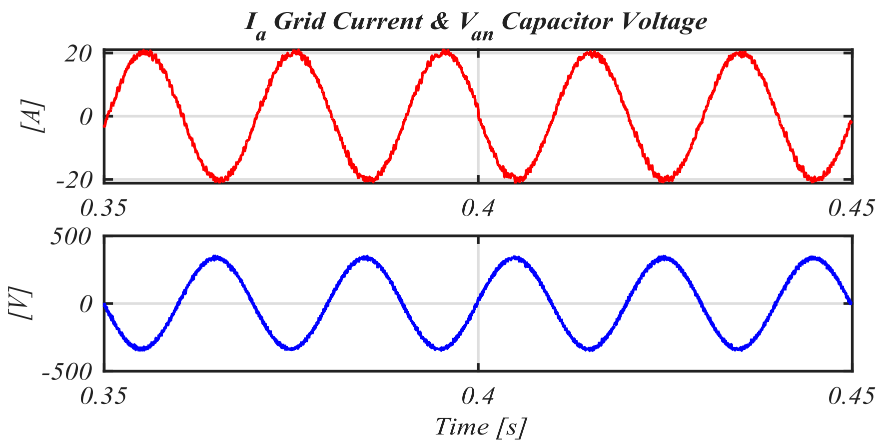

Figure 58 - Case 2 (HIL): Output current and capacitor voltage before and after estimation.

Figure 59 illustrates the evolution of the estimated impedance values and the corresponding trigger conditions.

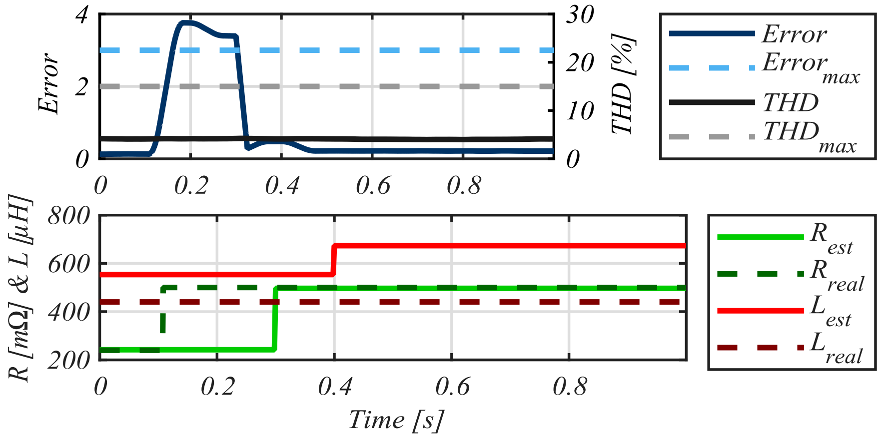

Figure 59 - Case 2 (HIL): Estimated resistance and voltage deviation after the resistive step.

It confirms that the resistive change alone does not significantly impact the THD, and therefore only the voltage-based trigger is activated. This test case further confirms the robustness of the trigger logic and the capability of the estimator to track impedance changes selectively, without unnecessary updates or disturbances to the waveform quality.

Case 3 – Inductive Step (HIL):

In the third test scenario, the grid inductance L_g is abruptly increased from 440 µH to 880 µH, while the grid resistance R_g is kept constant at 0.24 **Ω**. Unlike the previous case, this change has a much more noticeable impact on the system dynamics. The increased inductive component alters the impedance profile seen at the PCC and results in a degradation of the output current waveform, Figure 60 and Figure 61. As shown in Figure 60, immediately after the inductance step, the current phase becomes visibly distorted. This distortion leads to a rise in the THD of the current, which is promptly detected by the control logic. Once the THD exceeds its predefined threshold, the trigger activates the estimation procedure. The estimation algorithm responds effectively, correctly identifying the new inductance value. After the updated L_g is incorporated into the predictive model of the MPC controller, the current waveform stabilizes again. This recovery is evident in Figure 61, where the improved sinusoidal shape of the output current confirms the success of the adaptive update. Figure 62 shows the evolution of the estimation process, including the trigger conditions and the estimated impedance values. This test case highlights the importance of including both resistive and inductive components in the estimation and demonstrates the effectiveness of the THD-based trigger in addressing harmonic-related degradations caused by dynamic grid changes.

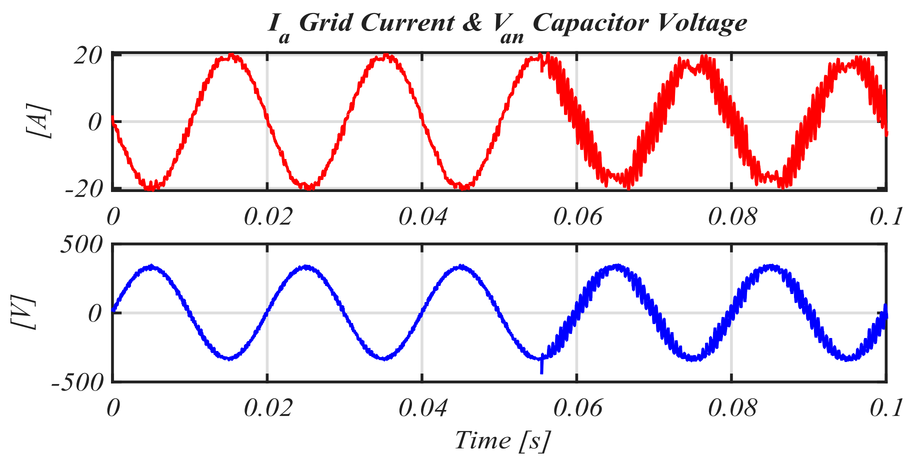

Figure 60 - Case 3 (HIL): Distorted output current after inductance increase.

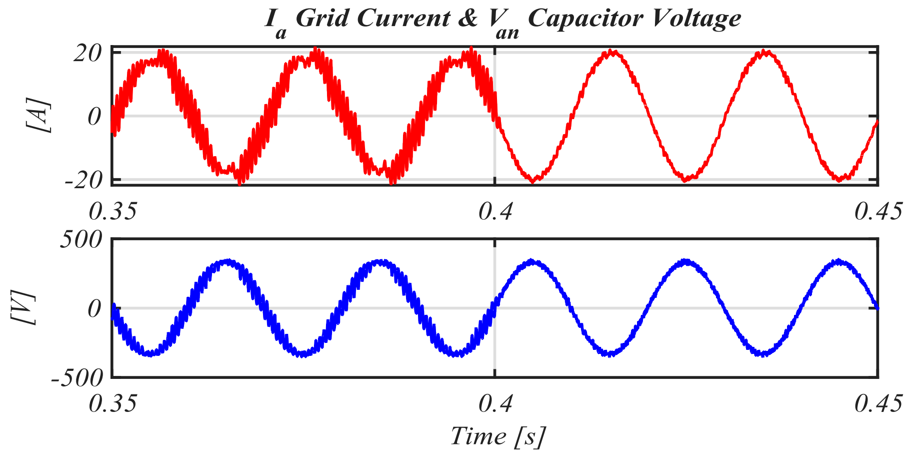

Figure 61 - Case 3 (HIL): Restored waveform after estimation update.

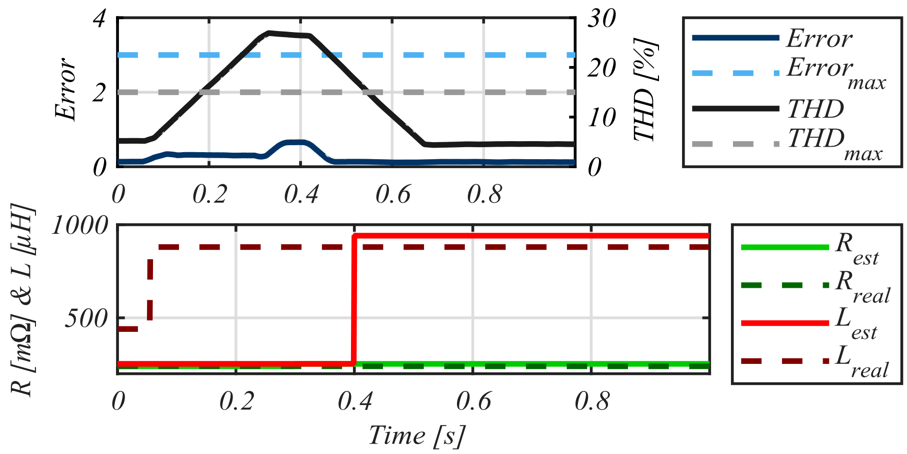

Figure 62 - Case 3 (HIL): Trigger and impedance estimation evolution. B.

B. Experimental-System Validation

The estimation algorithm was also validated on experimental hardware. The Typhoon HIL 402 platform was directly connected to the SiC-V3 three-phase grid-connected inverter through a custom-designed adapter board, allowing closed-loop operation without any external microcontroller. The setup is illustrated in Figure 63.

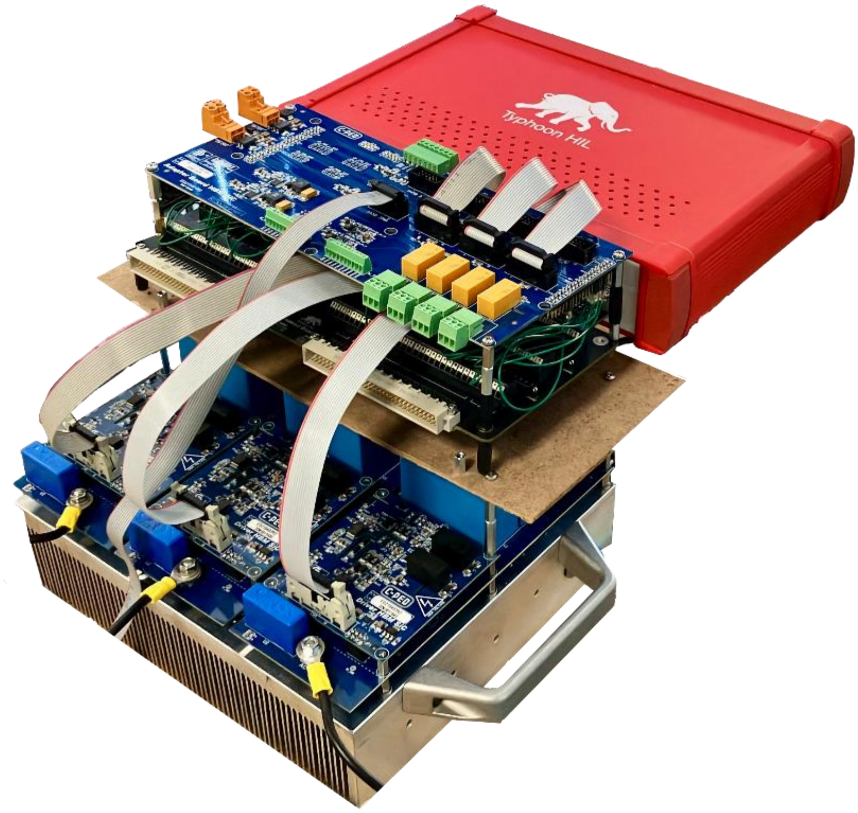

Figure 63 - Experimental-hardware setup: Typhoon HIL 402 connected to the SiC-V3 inverter through a dedicated adapter board. In this experimental configuration, the inverter is connected to the grid via galvanic isolation transformer.

Prior to the test, the impedance of the transformer as seen from the inverter terminals was accurately measured using an impedance analyser. The measured values were $R_g = 0.24\ \Omega$ and $L_g = 440\ \mu H$ and were used as reference for configuring the estimation scenario. To maintain consistency with the earlier simulations, the same impedance values were employed in HIL Case 1, enabling direct comparison between the real-hardware setup and the HIL validation. This provides a clear assessment of the estimator's performance across different platforms. During system startup, a mismatch between the measured and expected grid voltage triggers the estimation routine. As shown in Figure 64, the algorithm successfully identifies the correct grid parameters, with minimal deviation from the measured reference values. The resulting model update improves prediction accuracy within the MPC loop. Figure 65 illustrates the output current and filter voltage after estimation, confirming stable and high-quality waveforms. This test further demonstrates the applicability of the proposed method in real-world grid-connected inverter systems.

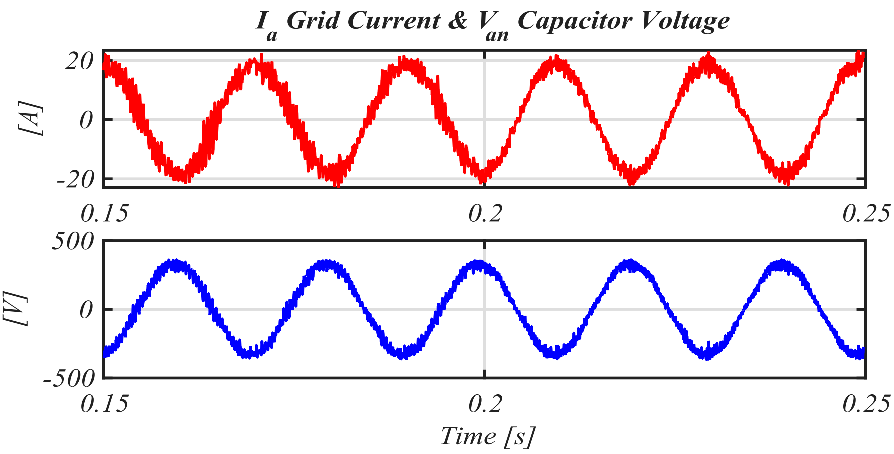

Figure 64 - Experimental test: estimated impedance and voltage deviation.

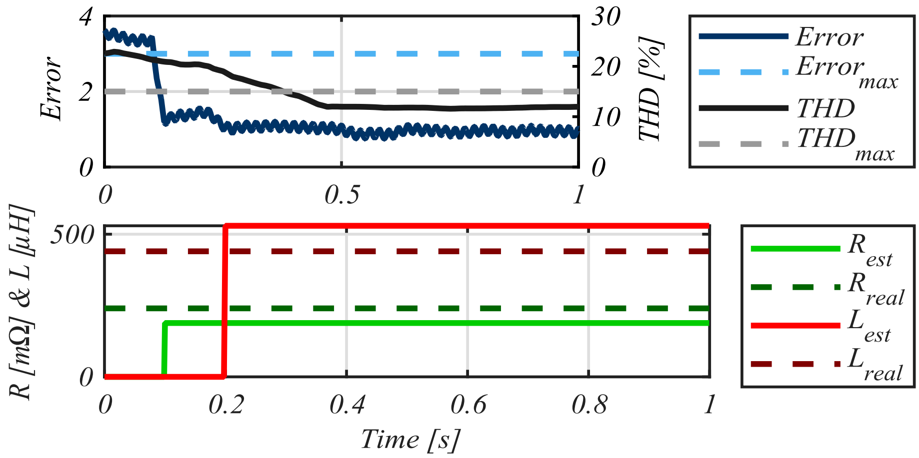

Figure 65 - Experimental test: phase-A output current and Van after estimation.

C. Summary of Estimation Results

The results of all test cases are summarized in Table XVIII. The table highlights the accuracy of the proposed technique under varying conditions: resistive steps, inductive steps, and real grid operation. The estimation always converges to the true impedance values within acceptable error margins and updates the MPC model in real-time. The method demonstrates excellent responsiveness and robustness to disturbances, making it suitable for adaptive control under realistic grid dynamics.

Table XVIII - Summary of estimation resultsfor all test cases

Case	$R_{g,experimental}$	$L_{g,exrimental}$	$R_{g,est}$	$L_{g,est}$

HIL 1	0.24 Ω	440 µH	0.25 Ω	470 µH
HIL 2	0.5 Ω	440 µH	0.49 Ω	670 µH
HIL 3	0.24 Ω	880 µH	0.25 Ω	940 µH
Experimental 1	0.24 Ω	440 µH	0.19 Ω	530 µH

As highlighted in Table XVIII, the inductance estimation in Case HIL 2 shows a notable deviation from the experimental value: $L_{gexperimental}$ = 440 µH versus L_{gest} = 670µH. This discrepancy, more pronounced than in other test cases, is attributed to transient measurement inaccuracies during the perturbation window, possibly caused by residual oscillations or sampling delays immediately after the resistive step. Despite this, the output current quality remained acceptable, and the control objectives were met without degradation. This confirms that the proposed estimation framework is not overly sensitive to individual estimation errors, as the control performance is inherently regulated by the THD and voltage error metrics. These metrics serve as indirect indicators of model fidelity: if the updated impedance values caused poor performance, the estimation would be re-triggered, ensuring convergence toward accurate values over time. Therefore, while occasional deviations can occur, they do not compromise the robustness of the overall control strategy.

D. Power Quality and Current Harmonics Responses

The power quality indicators obtained from all test cases, before and after the impedance estimation update, are reported in Table XIX. The table includes the RMS voltage and current, the active and apparent power, and the power factor, allowing a direct comparison of the steady-state behaviour of the system under both HIL and grid-tie conditions. The variations between the two operating conditions remain limited, confirming that the impedance update does not introduce distortions in the controlled variables and does not negatively affect the overall steady-state performance. From the comparison of the power quality indicators, it can be observed that the impedance update improves the power factor in all cases, particularly in the HIL 3 and Real 1 datasets. Before the estimation, these two tests exhibit the lowest PF values (0.953 and 0.973, respectively), which is consistent with the presence of a larger inductive component in the grid impedance. After the update, both PF values increase (0.995 for HIL 3 and 0.989 for Real 1), indicating that the updated model allows the controller to compensate more effectively for the reactive component of the grid, thus restoring a more favourable operating point. The rest of the variables (V_{RMS}, I_{RMS} and P) show limited deviations, confirming that the estimation procedure does not introduce steady-state distortions.

Table XIX - Effects of the resolution frequency Power quality indicators before and after the impedance estimation update.

Dataset	V_{RMS}	I_{RMS}	P [W]	S [VA]	PF
Before Impedance Estimation					
HIL 1	234.81	13.77	3214.09	3232.95	0.994
HIL 2	238.10	14.01	3324.63	3336.48	0.996
HIL 3	237.86	12.92	2929.47	3072.47	0.953
Real 1	236.96	13.03	3002.38	3086.90	0.973
After Impedance Estimation					
HIL 1	234.85	14.18	3317.59	3330.07	0.996
HIL 2	238.50	14.19	3372.06	3385.08	0.996
HIL 3	235.09	14.06	3291.16	3306.33	0.995
Real 1	235.97	13.21	3083.34	3116.86	0.989

Figure 66 reports the current harmonics response over the entire observation window. Each figure compares the spectral content of the output current before and after the estimation update. Since the purpose of this figure is to highlight the impact of the impedance variation on the harmonic content, only the most representative cases are shown, HIL 3 and Real 1. These two cases exhibit the most significant variations from the harmonic point of view, as they correspond to scenarios involving an inductive change (HIL 3) and grid-tie dynamics (Real 1), where the inductance plays a dominant role in shaping the harmonic profile.

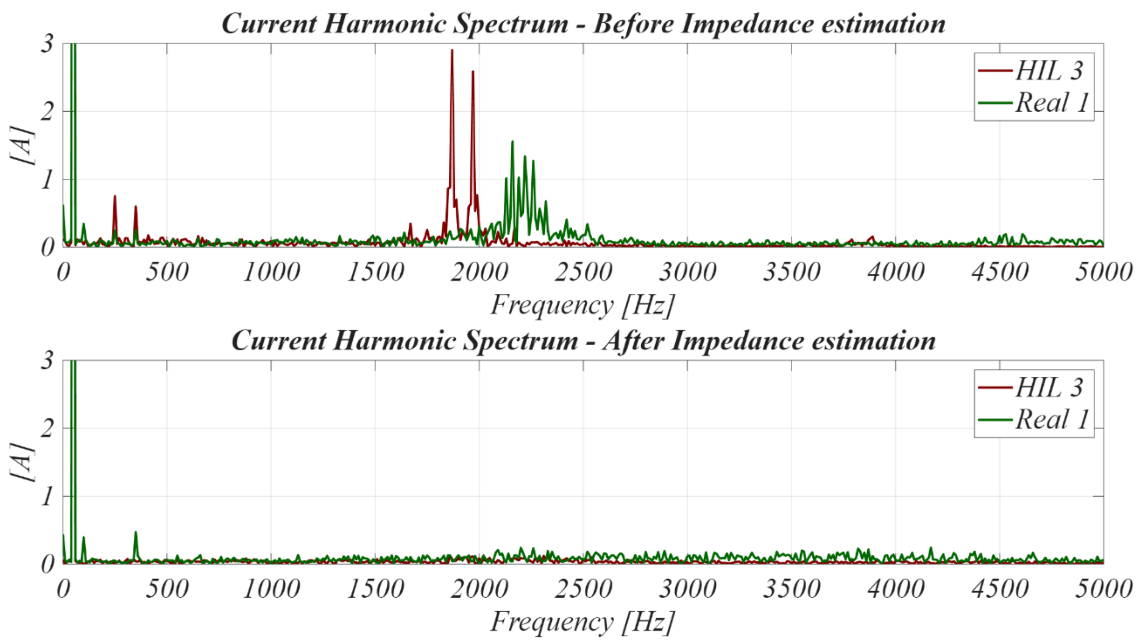

Figure 66 - Current harmonic spectrum for the most representative cases (HIL 3 and Real 1), comparing the spectral content before and after the impedance estimation update.

4 Passive Method

4.1 Introduction

Passive grid impedance estimation techniques exploit the natural dynamics of the power system without injecting any external disturbance. These methods rely on analysing signals that are already present in the grid or generated by the converter under normal operating conditions. Typically, harmonic components, transient variations, or load fluctuations are observed and processed to infer the equivalent impedance seen at the Point of Common Coupling (PCC). The non-intrusive nature of passive methods makes them attractive for applications where power quality constraints are stringent or where system disturbance must be minimized. However, their effectiveness is highly dependent on the richness of the ambient signal content. In cases where the harmonic distortion or dynamic variation is minimal, the resulting estimation may suffer from low resolution or high uncertainty. This section introduces and evaluates several passive techniques investigated during this doctoral project. A particular focus is placed on methods that leverage load-induced variations and frequency-domain analysis to extract impedance information. These approaches have been tested in both simulation and experimental setups, and their performance is compared with that of active techniques to highlight their respective strengths and limitations.

4.2 Impedance Estimation Method in Exploiting Variable Operating Conditions [33]

The method proposed for impedance estimation can be considered a passive method because it exploits intrinsic system disturbances due to changes in the operating conditions. Specifically, the changes could be caused by load variations such as a ramp or a step. The introduction of frequency harmonics due to load variations over time is shown in Figure 67. This harmonic disturbance is then utilized for impedance estimation. The algorithm operates in the background by recording and saving voltage and current values at the point of common coupling. When a current variation is detected for at least one second, the data saved in the past second is used for impedance estimation, following the flowchart in Figure 68, in which ΔI_q on represents the minimum current variation chosen to activate the parametric impedance estimation algorithm. The latter is performed by calculating the inductive and resistive components of Z_{grid} using two different methods to provide redundancy and ensure reliability in the estimation. The parameters that will be estimated include the resistive R_{pg} and inductive L_{fg} components of the grid-side LCL filter since the measurements for the impedance estimation are taken before the inductors. These values, assumed to be known, are subtracted from the estimate.

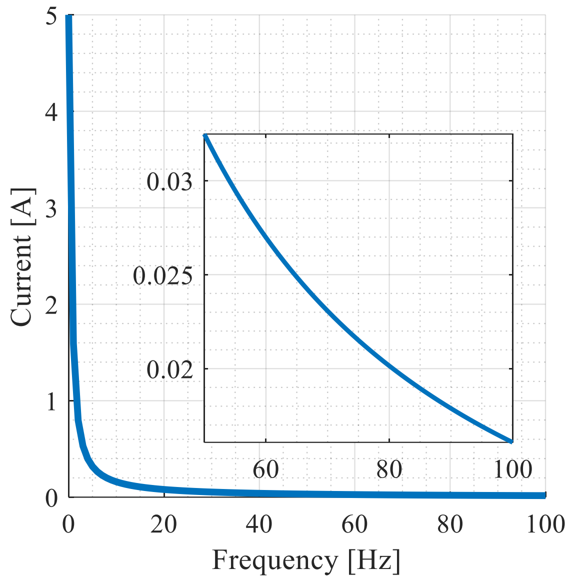

Figure 67 - FFT waveform due to a ramp variation of the load.

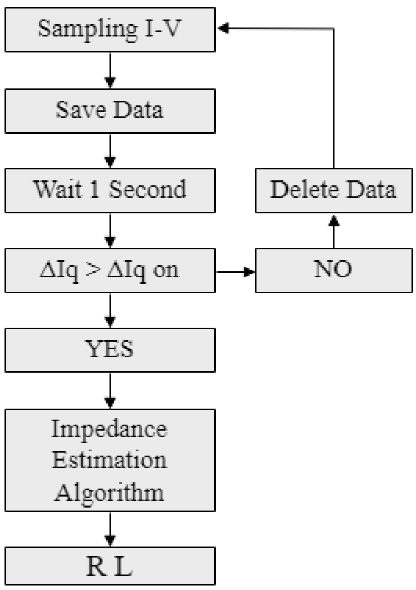

Figure 68 - Flowchart of the proposed passive impedance estimation algorithm.

The first estimation method for the resistive component is based on the voltage drop along the line, using current and voltage values in the dq reference frame at the beginning and end of the load variation.

$$R_1 = \frac{\left(\Delta V_q \cdot \Delta I_q + \Delta V_d \cdot \Delta I_d\right)}{\Delta I_q^{\ 2} + \Delta I_d^{\ 2}} - R_{pg} \tag{72}$$

The second method is based on the impedance triangle, in which Z(f) is the Fourier transform of the grid impedance. It is expressed as the pointwise ratio between voltage and current, using voltage and phase current samples for one second. Once the frequency-dependent impedance is obtained, the modulus and phase are derived, and consequently, the resistive component of the impedance.

$$R_2 = Z(f) * \cos(\varphi(f)) - R_{pg} \tag{73}$$

$$Z(f) = \frac{V(f)}{I(f)} \tag{74}$$

Once the resistive component is obtained, the estimation of the inductive component proceeds using two distinct methods. The first is based on the explicit expression of the impedance modulus. The second method derives the inductive component from the impedance triangle by considering the imaginary component.

$$L_1 = \frac{\sqrt{Z(f)^2 - R^2}}{(2 \cdot \pi \cdot f)} - L_{fg} \tag{75}$$

$$L_2 = Z(f) * \sin(\varphi(f)) - L_{fg} \tag{76}$$

The redundancy of the two methods has been used to evaluate the accuracy of the parametric impedance estimation: if the estimates R_1 and R_2 for the resistive component, and L_1 and L_2 for the inductive one, differ by more than the Desired Reliability Rate (DRR), the algorithm refutes the overall estimate's validity and discards the values.

$$DRR = \frac{abs(R_1 - R_2)}{\frac{(R_1 + R_2)}{2}} \cdot 100 \tag{77}$$

On the other hand, if the estimates fall within the range established by the DRR value, the estimation is validated, and the estimated R and L are calculated.

$$R = \frac{R_1 + R_2}{2} \tag{78}$$

$$L = \frac{L_1 + L_2}{2} \tag{79}$$

The DRR is set by the user depending on the application: it can be 5% or lower if the accuracy is critical, as in fault detection, or it can be higher, for example, to estimate and avoid the resonance frequency. In this work, the DRR has been set to 20%. Clearly, the choice of DRR is a trade-off, where a more stringent DRR leads to greater reliability versus a lower probability of obtaining an estimate.

4.3 Experimental Results

This section will present the set-up, how a load variation affects the system, and finally the results obtained with various operating condition points and different impedances.

A. Test experimental setup

The system under analysis comprises a three-phase inverter connected to the grid, with the parameters provided in Table XX. The grid is represented as a Thevenin equivalent featuring a voltage generator and a resistive-inductive (RL) impedance. The capacitive behaviour of the line is disregarded in this model, as its effect is negligible at the frequencies considered in this study. Thus, the impedance expression in the s-domain is given by:

$$Z_{grid} = R + sL \tag{80}$$

The considered converter is a three-phase Voltage Source Inverter (VSI) topology with current control, linked to the grid through an LCL low-pass filter. The inverter current control is implemented in the synchronous dq-axes, with the d-axis being 90 degrees leading the q-axis.

Voltage and current measurements that are used for both control and impedance estimation are taken before the grid-side filter inductance. Specifically, the voltage on the filter capacitor and the current in the converters side filter inductor has been sampled and considered for the impedance evaluation. The sampling for the impedance estimation is performed at 10 kHz and synchronized with the 10 kHz frequency of the control system. The proposed method for estimating the impedance has been validated using a 60 kW inverter connected to the EGSTON grid simulator. Between the inverter and the grid simulator, there is an LCL filter and a three-phase transformer. The inverter control is in current mode and is implemented in OPAL-RT.

The measurements for control are taken on the inverter-side inductor for the current and on the filter capacitor for the voltage

Table XX - System parameters

Parameters	Symbol	Value
Grid voltage (line-to-line, RMS)	V_a, V_b, V_c	*100 V*
System angular frequency	f_g	*50 Hz*
Grid-side filter inductance	L_{fg}	*200 µH*
Filter capacitor	C_f	*50 µF*
Inverter-side filter inductance	L_{fi}	*500 µH*
DC-link rate voltage	V_{dc}	*300 V*
Switching frequency	F_{sw}	*10 kHz*
Dead-Time	DT	*3.3 µs*
Q-axis reference current	I_q^*	*20 A*
D-axis reference current	I_d^*	*0 A*

. The inverter switching frequency is 10 kHz, as is the control frequency. Figure 69 shows the rough schematic of the basic set-up used to validate the results, while Figure 70 shows images of the actual components.

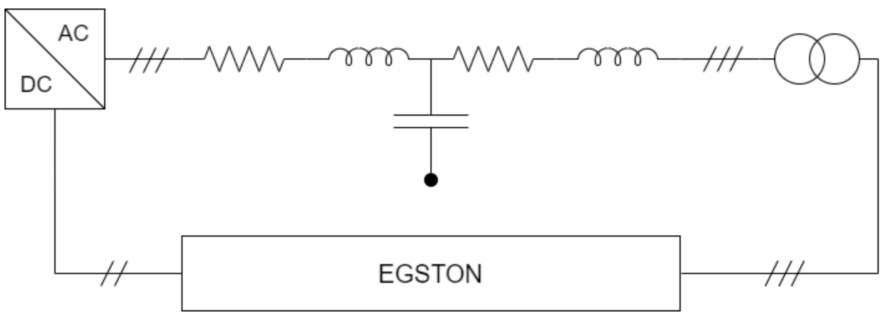

Figure 69: Equivalent circuit of the test setup.

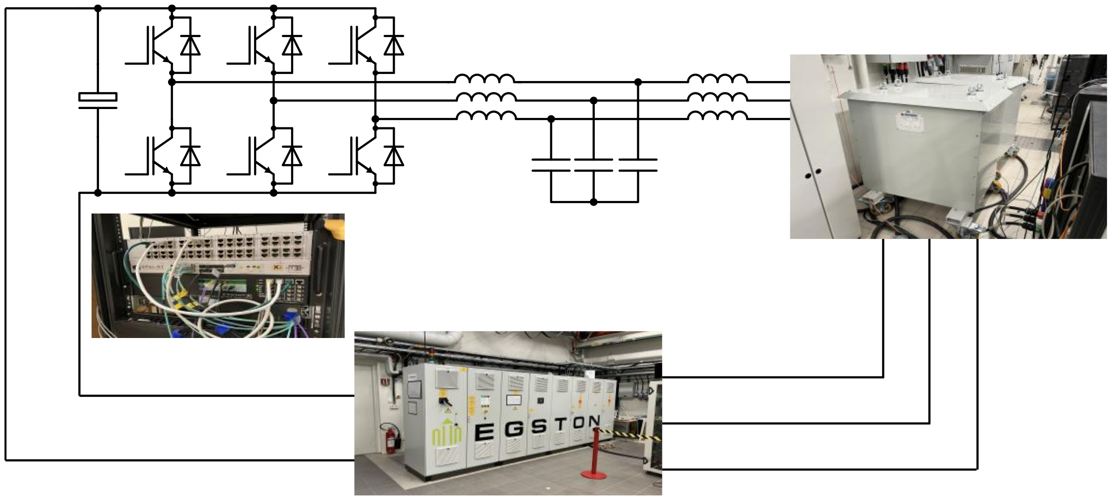

Figure 70 - Test setup graphical representation.

B. Data Management and Processing

The parameters used in the simulation are reported in Table XXI. The sampling frequency is the same as the switching frequency since the sampling is synchronous with the current control cycle. The control acquires the samples in double update mode, when the value of the modulating signal is either minimum or maximum. Therefore, for each second of sampling, 10,000 samples are obtained. The data have been sampled and saved using OPAL-RT logger. Later, the data was analysed by Matlab.

Table XXI - Algorithm settings and main parameters

Parameters	**Symbol**	**Value**
Inverter switching frequency	F_{sw}	*10 kHz*
Algorithm sampling frequency	F_{sam}	*10 kHz*
Frequency resolution	F_{res}	*1 Hz*
Number of samples	N	*10000*
Sampling duration	t_{sam}	*1 s*

C. Discussion of Results

The validation of the proposed method has been carried out assuming that the linear load variation generates a ramp effect in the current variation. Figure 71 shows the current change detected by the downstream control, which the algorithm then uses to plot results on the impedance estimate. In the example case, the ramp has a slope of 10 A/s.

In Figure 72, the transfer function of an ideal ramp is shown in red, and the FFT realized with the current samples in Figure 71 is represented in blue. With the data obtained from the FFT, the impedance is estimated. First, a ΔI_q on is chosen, which is the minimum start and end sampling value of I_q such that the algorithm works. The DRR is the second parameter to be chosen a priori. If the estimation algorithm receives the input of activation, it runs and, if the calculated DRR satisfies the imposed limitation, the results are obtained. To have more than one case study, three different impedances have been tested with three different ΔI_q on, three different operating conditions, and the DRR set to 20%. The results obtained show that a good impedance estimation is achieved, validating the proposed method as a powerful passive grid impedance estimation method.

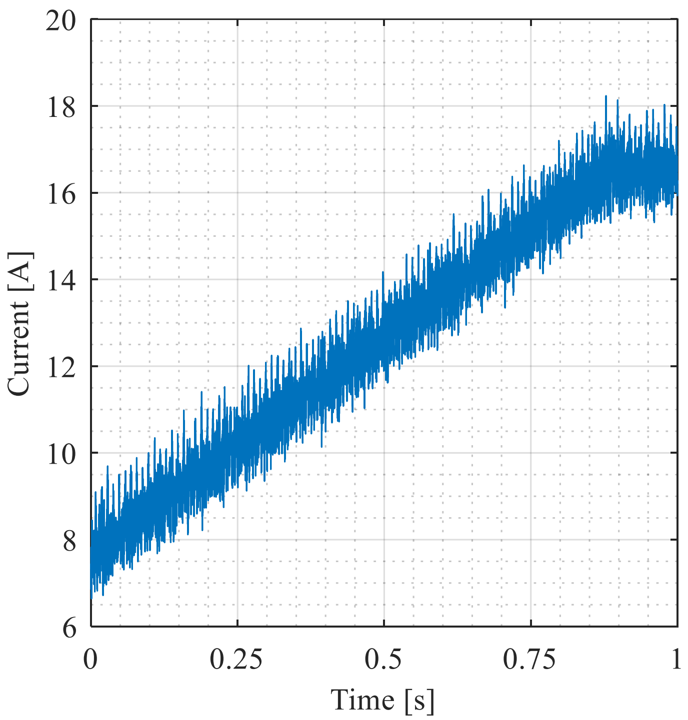

Figure 71 - Current ramp with a 10 A/s slope.

Figure 73 and Figure 74 show the oscilloscope and a still image of it. In particular, the oscilloscope was connected to the analog output channels that report measurements from the FPGA of the control board. Specifically, Figure 73 shows the voltage and current measurements on the dq axes while a ramp waveform has been injected to induce the harmonics generation. Indeed, the load variation has been modelled by adding a ramp signal in the d-current reference of the control loop. Since, the inverter as feedback for control uses the voltage on the filter capacitor and the current on the converter-side inductor, the measurements used for estimation and shown on the oscilloscope in Figure 73 are the result of the Clark and Park transforms, calculated directly from the FPGA, of the three-phase currents and voltages, which are visible instead in Figure 74.

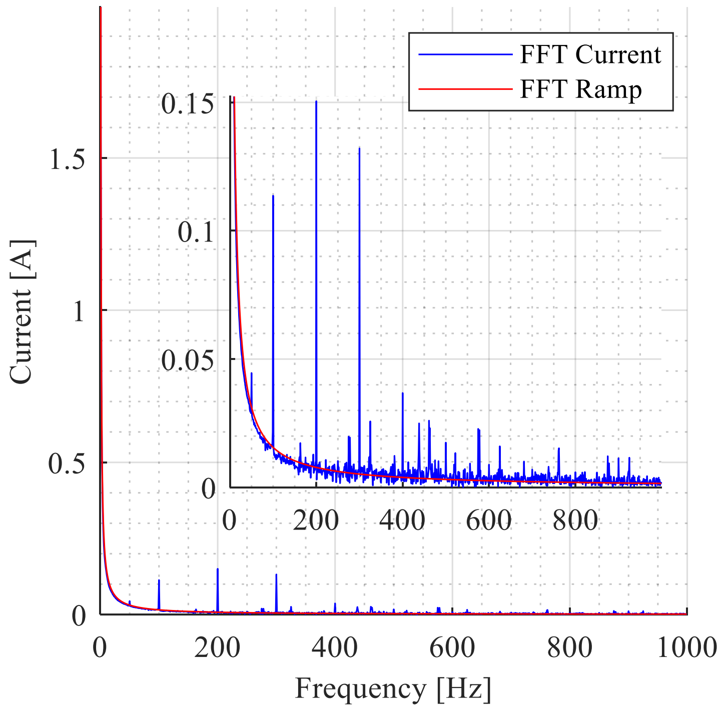

Figure 72 - FFT comparison of the current ramp generated by a load variation (blue waveform) to an ideal ramp (red line).

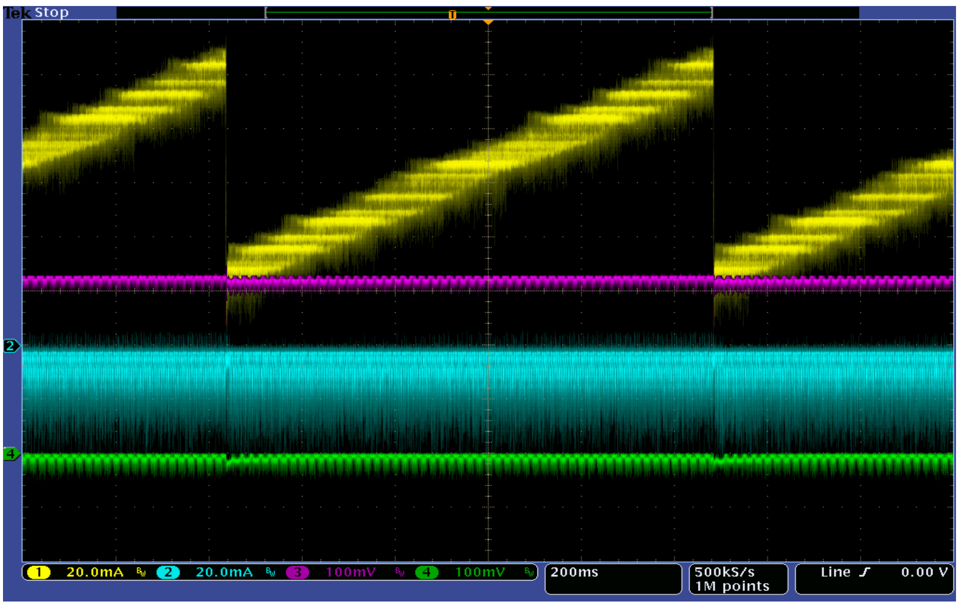

Figure 73 - analysed current and voltage waveform in the dq frame for the impedance estimation.

Figure 74 - Test setup for measuring the three-phase currents and voltages directly calculated by the FPGA.

Figure 75 shows the estimation result obtained as the point ratio of voltage and current in the frequency range. In particular, one can see in orange the actual impedance of the system and blue the result of impedance estimation. Interestingly, the initial accuracy at low frequencies, which is the most important for the grid impedance estimation, is quite good, as a result of the stimulus at low frequencies. In contrast, the deviation of the estimate from the true value as the frequency increases is related to the attenuative effect of the LCL filter at the inverter output on harmonics.

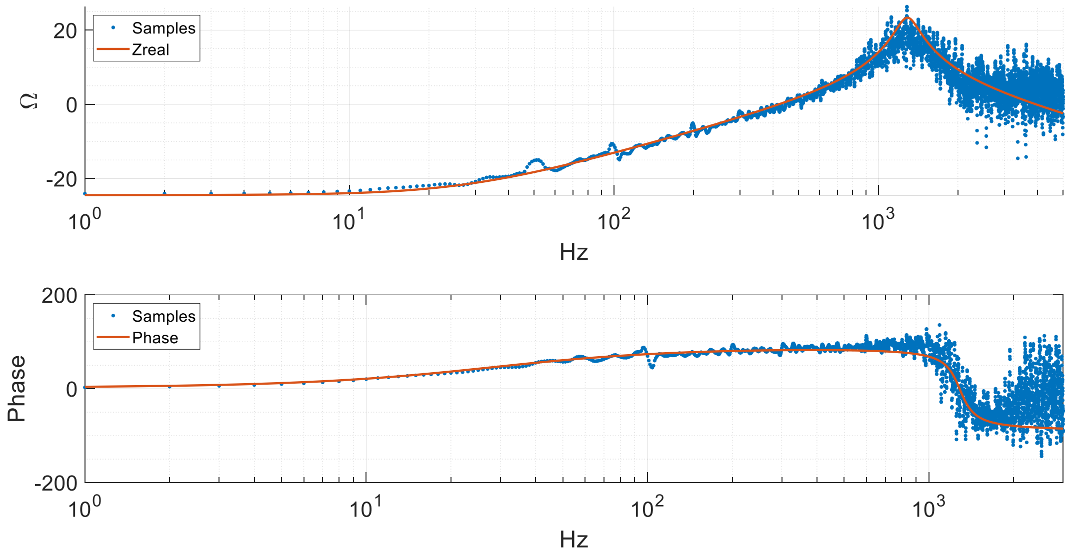

Figure 75 - Impedance estimation using the passive method proposed (blue) compared to the experimental impedance (orange) in modulus and phase.

For further validation, the method has been tested and validated with an additional impedance value, thus obtaining a larger sample set. For this reason, an inductance has been added in series to the EGSTON-side transformer. Figure 76 shows the added inductance with a theoretical value of 1.7 mH. Finally, in Figure 77, the results obtained, as presented above, with the additional inductance in series are shown. Interestingly, the overall accuracy is higher; this could be explained because a network with a higher overall impedance has a higher information content.

Figure 76: Additional inductance in series to the EGSTON-side transformer.

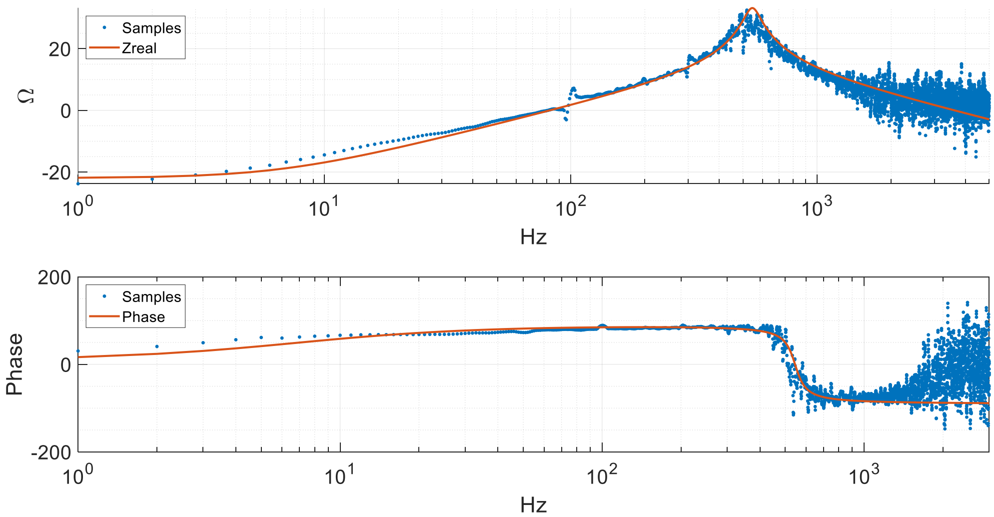

Figure 77: Impedance estimation using the passive method proposed (blue) compared to the experimental impedance (orange) in modulus and phase considering the additional inductance in series.

5 Railway applications

5.1 Introduction

This chapter translates the impedance-aware framework developed in the previous chapters to a real-world railway electrification scenario. The focus is on urban DC railway systems equipped with regenerative braking, where a bidirectional Energy Recovery System (ERS) injects braking energy from the catenary back into the AC grid. Under these conditions, the ERS behaves as a constant power load, exhibiting negative incremental impedance and potentially exciting low-frequency resonances of the supply line and catenary. If these oscillations overlap with the frequency range of signalling circuits, both system stability and safe operation can be severely affected.

Within this context, the chapter presents a complete workflow for real-time resonance estimation and active damping in a 2.5 MW railway ERS. After introducing the operating principles of regenerative braking and the bidirectional substation topology, the railway infrastructure is modelled, including catenary, track and converter interfaces. A disturbance-based method is then used to estimate the DC-side resonance frequency from synchronously sampled voltage and current measurements, and an active damping controller is configured to act selectively around the estimated resonance. The proposed strategy is implemented on an industrial control platform and validated through Hardware-in-the-Loop and system-level simulations, demonstrating that resonance can be mitigated without compromising energy recovery capability or power quality.

5.2 Real-Time Resonance Estimation and Damping Control [51]

With the increase in urbanization of cities, the cost of energy, and current European policies to stop the production of vehicles with engines powered by fossil fuels, it is easy to imagine that the demand for public transport will increase. Therefore, it makes sense to implement policies related to optimizing urban railway systems, not only for the forecast of demand growth but also for environmental reasons. In general, the running of an electric train can be divided into four phases: acceleration, cruising, coasting, and braking. During the acceleration phase a train increases its speed and draws energy from a catenary or a third track [52]. During the cruising phase, the power required by the electric machine operating as a motor is approximately constant. During coasting, in which the train moves by inertia, the speed of the vehicle is almost constant, and the amount of power absorbed is negligible. During the braking phase the train decelerates until it stops. In urban areas, since the distances between stations are short, the cruising phase is generally not reached. During the deceleration phase, the use of electric braking is widespread in rail transport as, unlike friction braking, it does not generate wear, dust, odour, heat, or noise. Electric braking can be divided into two categories: rheostatic and regenerative braking. During rheostatic braking the kinetic energy is converted into electrical energy and subsequently dissipated in the form of heat on rheostats, generally placed on the roof of the vehicle. On the other hand, regenerative braking is the one that allows this energy to be reused in some way, by injecting it directly into the supply catenary. Normally, in urban areas the power supply of the overhead contact lines is in DC using non-reversible conversion systems, such as diode rectifiers. Therefore, if the catenary is unable to accept the braking power, dissipative braking is activated, losing the possibility of any recovery. An advanced bidirectional railway power substation is shown in Figure 78, where during the train acceleration the power flow is directed from the grid to the catenary (condition 1). In a common substation, during the train braking the power flow is directed from the traction system operating as a generator to the braking rheostats (condition 2), dissipating the energy as heat. In the case of new, modern, substations, during the regenerative braking the power flow is directed from the traction system operating as a generator to the Energy Recovery System (ERS) (condition 3), which injects the power into the AC grid.

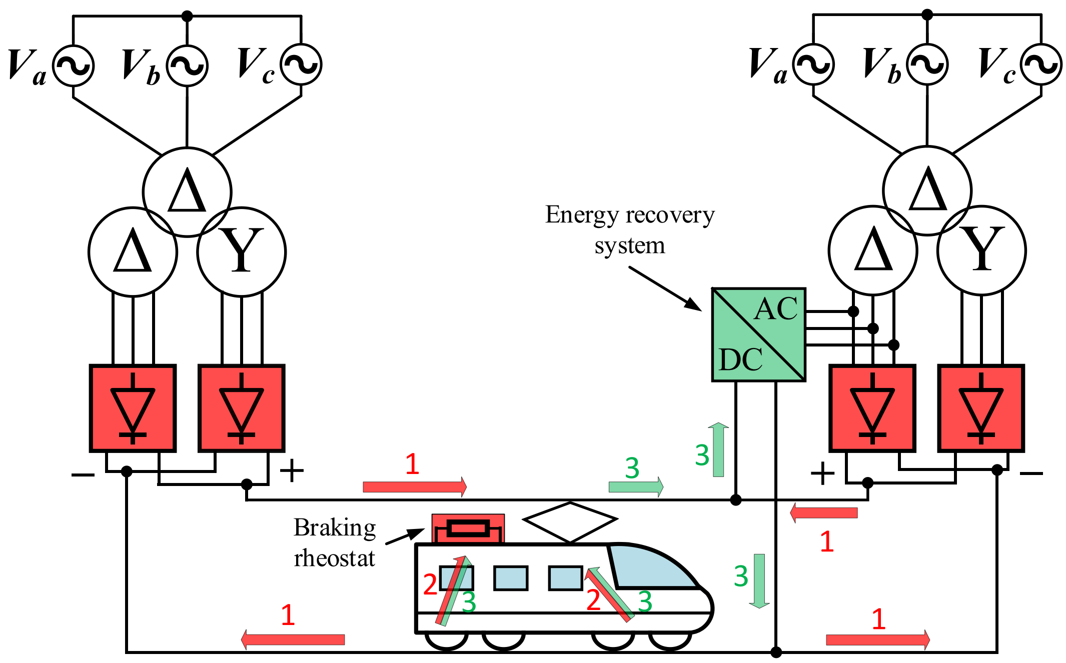

Figure 78. Bidirectional railway power system.

The AC voltage on the grid side is almost constant during the energy recovery phase, hence, being the recovery inverter AC current controlled [7], the system operation is in the situation called Constant Power Load (CPL); when the catenary voltage decreases, the catenary current must increase to keep the power constant. This effect can introduce low-frequency oscillations so that if they fall within the resonant frequency of the power supply line, the current oscillations would be amplified compromising the stability of the catenary system with the risk that passing trains will stop [53]. Such effect is related to the intrinsic characteristic of constant power loads which, showing a negative incremental impedance, generates, consequently, the reduction of the stability margin [67]. Figure 79 shows experimental data obtained by analysing 1000 cases reported on the x-axis (#), about catenary low-frequency harmonics during the energy recovery phase. Z-axis shows the current harmonics in [A] as a function of frequency in [Hz] reported on the y-axis. This work deals with the issues related to energy recovery in the braking phase of railway vehicles with the aim of reducing overall energy consumption and increasing the total efficiency of the system, bringing benefits from both the economic and environmental point of view. Recovery of the train energy injecting a certain amount of power directly into the AC grid must be accomplished considering specific effects that arise when a constant power load is connected to the catenary, which is, due to its nature, unregulated.

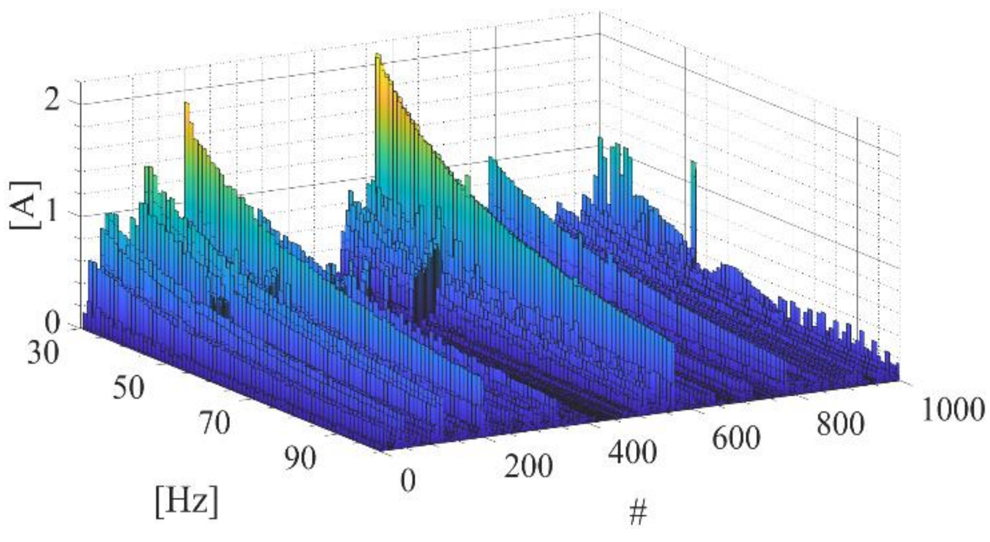

Figure 79. Experimental data from real catenary current.

Theoretically, a DC line fed by a 12-pulse diode bridge rectifier should contain, in addition to the continuous signal, only multiple harmonics of *600 Hz*. However, more harmonics appear in the catenary due to several reasons. Among these reasons are the voltage unbalances in the transformer windings, the not negligible inductances of cables and catenary, the voltage inductances due to proximity (parallel circuits), the traction returns, and so on. The interaction between the braking energy recovery system and the train's regenerative brake produces interactions that tend to amplify existing signals in the catenary. Several approaches are proposed in literature to solve the problems related to the constant power load, as linearization, passive damping control and active damping control that includes virtual resistor and virtual capacitor. In [65] the authors propose a method of input-output linearization of a boost converter for constant voltage load and constant power load by injecting a small inductor current signal into the output node. In [63] it is proposed the active damping control based on Multiagent Stabilization System (MASS) for DC power systems with CPL, where each load contributes to microgrid stabilization. In [66] the active damping control system is used to reduce the oscillations and increase the electrical inertia of a microgrid using a virtual capacitor. In [75] the passive approach for CPL stabilization is proposed by using three different circuits, RC parallel, RL parallel, RL series. Normally, the passive damping control system is not very common since it consists of introducing a passive component, usually a resistor, in series with the capacitor branch of the filter, thus reducing the efficiency of the system. In contrast, the active damping control system generally acts on the converter control loop using either current or voltage measurement as feedback [108].

More information about the topic of active damping control can be found in [72] where, however, a time-invariant system and steady state conditions were considered. In [69] active damping is proposed to artificially reduce the output impedance in DC-DC power converter. The method of virtual resistor has been deeply investigated in applications such as DC-Microgrid [109], STATCOM [110], and bidirectional DC-DC [71]. Moreover, the virtual capacitor approach has been proved in [111]- [112] introducing the ultracapacitors technology. In [113] a combined resistive-capacitive damper is proposed for weak grids. A similar methodology is illustrated in [70] for DC microgrids operating in the low-voltage standard. The sensitivity analysis for High-Voltage DC grid is presented in [58].

The problem experimentally encountered in the field is the occurrence of resonances during the braking energy recovery phases, which, if they fall into the same spectrum of the frequencies used for railway signalling, do not allow the full recovery of available energy by limiting it to modest values. There are two approaches hypothesized as viable solutions [114]:

1. using the active damping control system with the purpose of reducing the harmonics around the resonance frequency;
2. estimate the impedance online and simultaneously adjust the control parameters of the energy recovery system.

Obviously the two approaches are not mutually exclusive; rather we would like to try to act on several aspects to increase the energy recovery potential as much as possible without at the same time affecting the robustness of the safety systems.

In this work, the first mentioned solution is analysed. The proposed method basically consists of developing an active damping control system using the voltage on the catenary as feedback and acting directly on the current control of the energy recovery system. The innovative aspect is the possibility of being able to derive the resonance frequency in real-time and thus set the cut-off frequency of the low-pass filter used in the damping control algorithm.

The introduction of the disturbance is done through the ERS; in fact, the disturbance is injected as a current into the grid and affects the catenary. Then the voltage and current values on the catenary are synchronously sampled and the response of the catenary to the disturbance is evaluated and the current resonance point can be derived. The work initially deals with the modelling of the system and the configuration of the railway infrastructure. The equivalent circuits and operating modes in the presence of the braking ERS are defined and illustrated. Subsequently, the method associated with the estimation of the DC side resonance is shown, with reference to the introduced stimulus. The complete procedure is shown in detail and divided into functional blocks. Finally, the results obtained by implementing the proposed method on an industrial control board are shown. The innovative contribution of the proposed work lies in the real-time estimation of resonance and the ability to confine the damping control action to only the frequencies affected by resonance. Furthermore, the action is performed on the AC side as it is not allowed to introduce any signal directly on the catenary.

5.2.1 System Description and Configuration

The scheme of the investigated railway system is summarized in Figure 80a, the system parameters are summarized in Table XXII. The catenary is supplied by the specific double-side feeding topology and the energy recovery inverter is placed close to one of the two substations.

Table XXII - System parameters

Parameters	Symbol	Value
Transformer grid-side impedance	$Z_{g\Delta}$ $(R_{g\Delta}+L_{g\Delta})$	$0.001\ \Omega + 100\ \mu H$
Transformer catenary-Δ-side impedance	$Z_{t\Delta}$ $(R_{t\Delta}+L_{t\Delta})$	$0.006\ \Omega + 0.38\ \mu H$
Transformer catenary-Y-side impedance	Z_{tY} $(R_{tY}+L_{tY})$	$0.002\ \Omega + 0.274\ \mu H$
ERS AC-side impedance	$Z_{ers\text{-}AC}$ $(R_{ers\text{-}AC}+L_{ers\text{-}AC})$	$0.03\ \Omega + 160\ \mu H$
ERS DC-side impedance	$Z_{ers\text{-}DC}$ $(R_{ers\text{-}DC}+L_{ers\text{-}DC})$	$0.01\ \Omega + 1\ \mu H$
Catenary impedance (200 m)	$Z_{c\text{-}200m}$ $(R_{c\text{-}200m}+L_{c\text{-}200m})$	$0.0021\ \Omega + 351\ \mu H$
Railway track impedance (200 m)	$Z_{rt\text{-}200m}$ $(R_{rt\text{-}200m}+L_{rt\text{-}200m})$	$0.0028\ \Omega + 343\ \mu H$
Catenary impedance (1800 m)	$Z_{c\text{-}1800m}$ $(R_{c\text{-}1800m}+L_{c\text{-}1800m})$	$0.0185\ \Omega + 3950\ \mu H$
Railway track impedance (1800 m)	$Z_{rt\text{-}1800m}$ $(R_{rt\text{-}1800m}+L_{rt\text{-}1800m})$	$0.0254\ \Omega + 3880\ \mu H$
ERS DC-bus equivalent impedance	Z_{ers} $(R_{ers}+C_{ers})$	$0.005\ \Omega + 6\ mF$
Transformer ERS and filter impedance	Z_{tYn} $(R_{tYn}+L_{tYn})$	$0.03\ \Omega + 160\ \mu H$
Load resistance	R_l	$4.7\ \Omega$
Train equivalent impedance	Z_t (R_t+C_t)	$0.005\ \Omega + 5\ mF$
DC-link rate voltage	V_{DC}	$1750\ V$
Sampling frequency (control)	F_{spl}	$6.6\ kHz$
Switching frequency (inverter)	F_{sw}	$3.3\ kHz$
Dead-Time (inverter)	DT	$3.3\ \mu s$
Q-axis reference current	I_q^*	$0 \div 800\ A$
D-axis reference current	I_d^*	$0\ A$
Current controllers' gains	$K_{p\text{-}i}$	0.001
	$K_{i\text{-}i}$	0.17
PLL bandwidth (Kalman based)	$\square_0$	$38\ rad/s$

The current-controlled three-phase NPC inverter is used to accomplish the Energy Recovery System, which is connected to the grid by an L-type low-pass filter, as shown in Figure 80b.

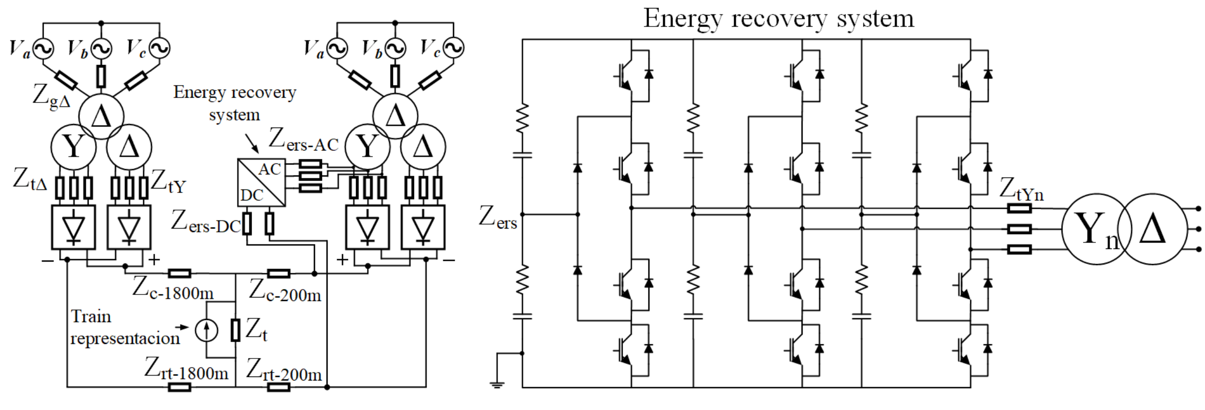

Figure 80. a) Scheme of the catenary system with substations. b) 2.5 MW Energy Recovery Inverter (ERS).

In the present scenario, the DC-side filters at the output of the traction substations are not being considered due to their inconsistent presence. First, during the braking phase, the current supplied by the substations is deemed practically insignificant compared to that supplied by the train itself. Furthermore, the capacitors installed onboard the train, specifically on the DC side of the traction inverter, are at least two orders of magnitude larger than the capacitors on the DC-side filters of the substation, which typically fall within the range of microfarads (μF). The control of the inverter is implemented in synchronous reference on the dq-axes. Disturbances and variations used to estimate the resonance frequency are introduced by the control algorithm. The DC-side is represented by the catenary and the train. The overhead contact line is modelled assuming a rigid aluminium profile supporting a copper contact line, as shown in Figure 81a. The aluminium bearing support height is *110 mm* and its equivalent section is *2423 mm*^{2}. While the equivalent section of the copper contact line is *150 mm*^{2}. Concerning the track, the standard UIC50 profile used in metropolitan urban areas is taken into consideration, made of steel with equivalent section equals to *6400 mm*^{2}, Figure 81b. Based on these hypotheses, the impedance values expressed in resistance and inductance of the catenary and of the track are calculated. The parameters used for the calculation of the impedance of the catenary are listed in Table XXIII.

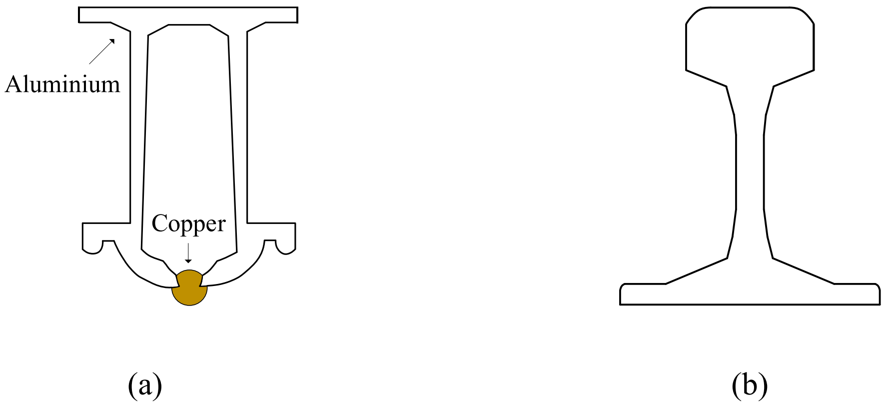

Figure 81. Cross section: a) overhead catenary, b) track.

Table XXIII - Catenary contact line parameters [115]

Parameters	**Symbol**	**Value**
Copper resistivity	ρ_{co}	$1{,}68 \cdot 10^{-8}\ \Omega \cdot m$
Aluminum resistivity	ρ_{al}	$2.75 \cdot 10^{-8}\ \Omega \cdot m$
Messenger cable equivalent section	S_{mc}	$2423\ mm^2$
Contact wire equivalent section	S_{cw}	$150\ mm^2$
Steel resistivity	ρ_{steel}	$18 \cdot 10^{-8}\ \Omega \cdot m$
Steel mass per unit length	$m_{l\text{-}steel}$	$50\ kg/m$
Steel density	d_{steel}	$7850\ kg/m$

The equivalent section of the messenger wire in copper was first obtained and then the total area was considered also including the contact wire:

$$S_{eq} = \frac{\rho_{co}}{\rho_{al}} \cdot S_{mc} + S_{cw} = 1630 mm^2 \Rightarrow r_c = 0.0228m \tag{81}$$

Hence, the catenary total resistive component can be evaluated as:

$$R_c = \frac{\rho_{co}}{S_{eq}} = 10.3 \frac{\mu\Omega}{m} \tag{82}$$

Whereas, according to [116] it is possible to calculate the inductance as follows:

$$L_c = \frac{\mu_0 s}{2\pi}\left[\ln\left(\frac{2s}{r_c}\right) - 1\right] \tag{83}$$

Where s is the length of the wire.

For the track, the equivalent section in copper is obtained starting from the equivalent section and the density of the steel:

$$S_{eq} = \frac{\rho_{co}}{\rho_{steel}} \cdot \frac{m_{l-steel}}{d_{steel}} = 595mm^2 \Rightarrow r_{rt} = 0.0138m \tag{84}$$

Therefore, the railway tracks resistive component considering the two paths connected in parallel can be obtained as:

$$R_{rt} = \frac{\rho_{co}}{2 \cdot S_{eq}} = 14.1\frac{\mu\Omega}{m} \tag{85}$$

With the same procedure used to calculate the contact wire inductance, the track inductance is evaluated as:

$$L_{rt} = \frac{\mu_0 s}{2\pi}\left[\ln\left(\frac{2s}{2 \cdot r_{rt}}\right) - 1\right] \tag{86}$$

Energy recovery occurs for the entire duration of braking, where the recoverable kinetic energy decreases with the square of the speed. During the phase of electric braking and referring to Figure 78, the train can have its direction of movement from right to left, where the train moves away from the ERS and therefore the impedance increases, or from left to right, where the impedance decreases.

The most challenging condition occurs when the train is in regenerative braking, i.e., it injects active power into the catenary, and the ERS is active, draining power from the catenary and feeding it into the grid. The equivalent circuit representing this condition is not univocally defined, as it changes with both train position and braking conditions.

The proposed study aims to validate a methodology to estimate the catenary resonance frequency at the braking starting point and set the damping control system close to the estimated resonance frequency. Without loss of validity, it is decided to choose as the braking start point where the train is *200 m* from the right substation and *1800 m* from the left substation assuming a total line length of *2 km*, referring to Figure 80a. Therefore, two limiting cases have been considered.

1. The ERS drains power from the overhead contact line with the train braking by activating the braking rheostats (see Figure 78), thus effectively without power input from the train. In this condition the power is recirculating between the ERS and the power substation. The equivalent circuit is depicted in Figure 82.

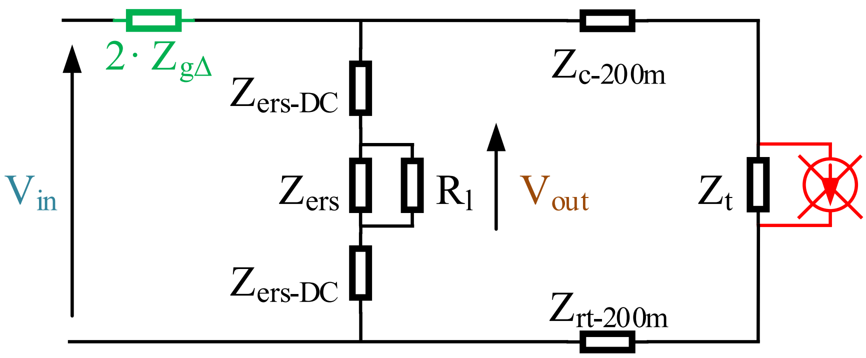

Figure 82. Case 1 energy recovering – Equivalent circuit.

From (87), the related transfer function can be evaluated as (88)

$$\begin{cases} Z_{ctrt} = \left(Z_{c-200m} + Z_t + Z_{rt-200m}\right) \\ Z_{ers-l} = Z_{ers} // R_l = \left(\dfrac{Z_{ers} \cdot R_l}{Z_{ers} + R_l}\right) \end{cases} \tag{87}$$

$$G_1 = \frac{V_{out}}{V_{in}} = \frac{1}{\left(\dfrac{Z_{ctrt} + Z_{ers-l} + 2Z_{ers-DC}}{Z_{ers-l} \cdot Z_{ctrt}}\right) 2Z_{g\Delta} + \dfrac{2Z_{ers-DC}}{Z_{ers-l}} + 1} \tag{88}$$

2. The ERS draws power from the overhead contact line with the train that does not activate the braking rheostat during the deceleration phase (Figure 78). The kinetic energy of the train, converted into electricity, is fed into the catenary, and completely recovered by the ERS: the current from the substation is zero. The equivalent circuit is shown in Figure 83.

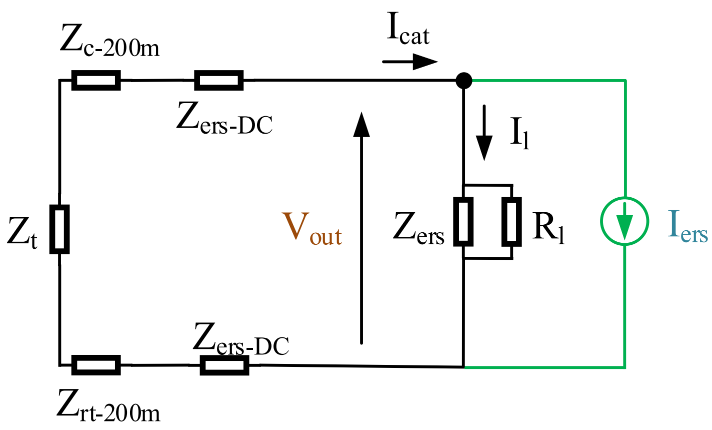

Figure 83. Case 2 energy recovering – Equivalent circuit.

The transfer function for this second case can be expressed as (89)

$$G_2 = \frac{V_{out}}{I_{ers}} = \frac{\left(Z_{ctrt} + 2Z_{ers-DC}\right) Z_{ers-l}}{\left(Z_{ctrt} + 2Z_{ers-DC}\right) + Z_{ers-l}} \tag{89}$$

Finally, the Bode plots and the frequency responses obtained by the two systems reported in case 1 and case 2 are shown respectively in Figure 84 and Figure 85.

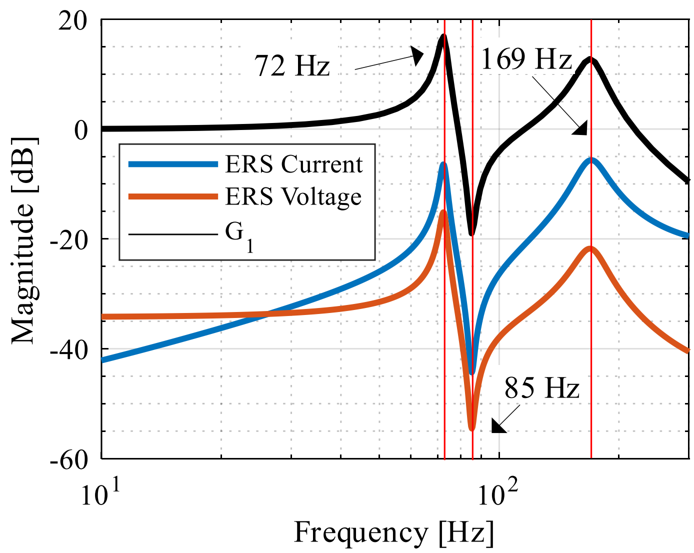

Figure 84. Case 1 energy recovering – Transfer function.

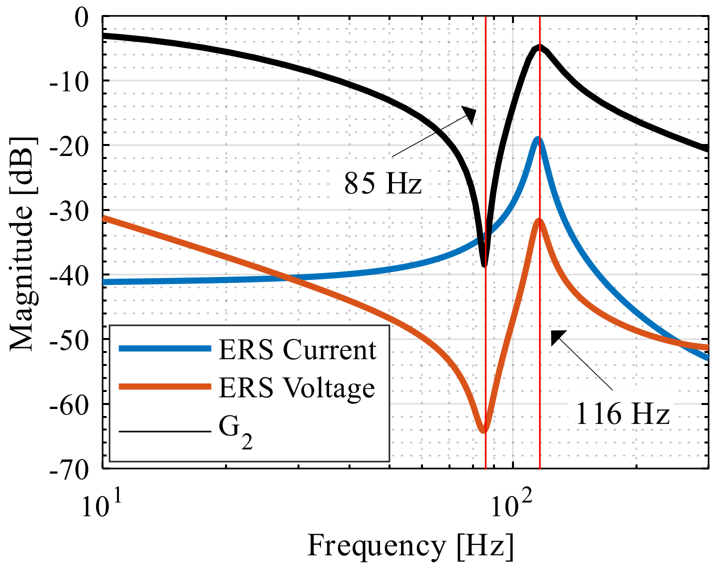

Figure 85. Case 2 energy recovering – Transfer function.

The frequency responses are obtained through a Matlab/Simulink evaluation by introducing a White Noise signal and evaluating the frequency response obtained through the voltage and current measurements on the DC bus of the Energy Recovery System. Finally, according to the operating mode of the ERS, by recovering the largest possible amount of braking energy, the system will be closer to operating condition 2 than condition 1.

5.2.2 Resonance Estimation and Damping Control

In this section, the operational procedure and implementation of resonance estimation and damping control are presented. In Figure 86, the complete algorithm flowchart is provided, which summarizes the concepts addressed in the work.

A simplified system block scheme is shown in Figure 87. The dependencies between the blocks for the resonance estimation and damping control can be clearly recognized. The catenary resonance estimation requires the measurement of the DC-side current I_{dc}, which is acquired from a current sensor installed on the inverter DC bus. The methodology for the resonance frequency estimation, the selection of the band-pass and band-

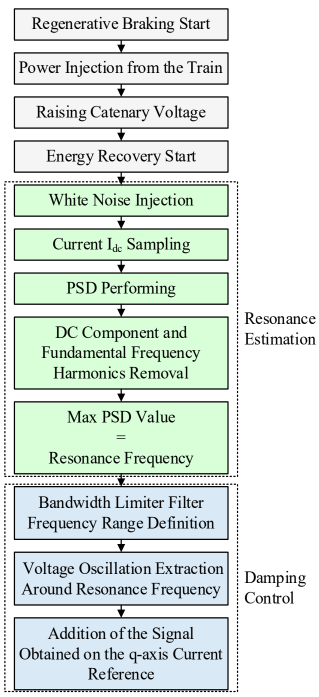

Figure 86. Flowchart of the proposed algorithm.

stop frequencies of the bandwidth limiter, and finally the configuration of the damping control is described in this section.

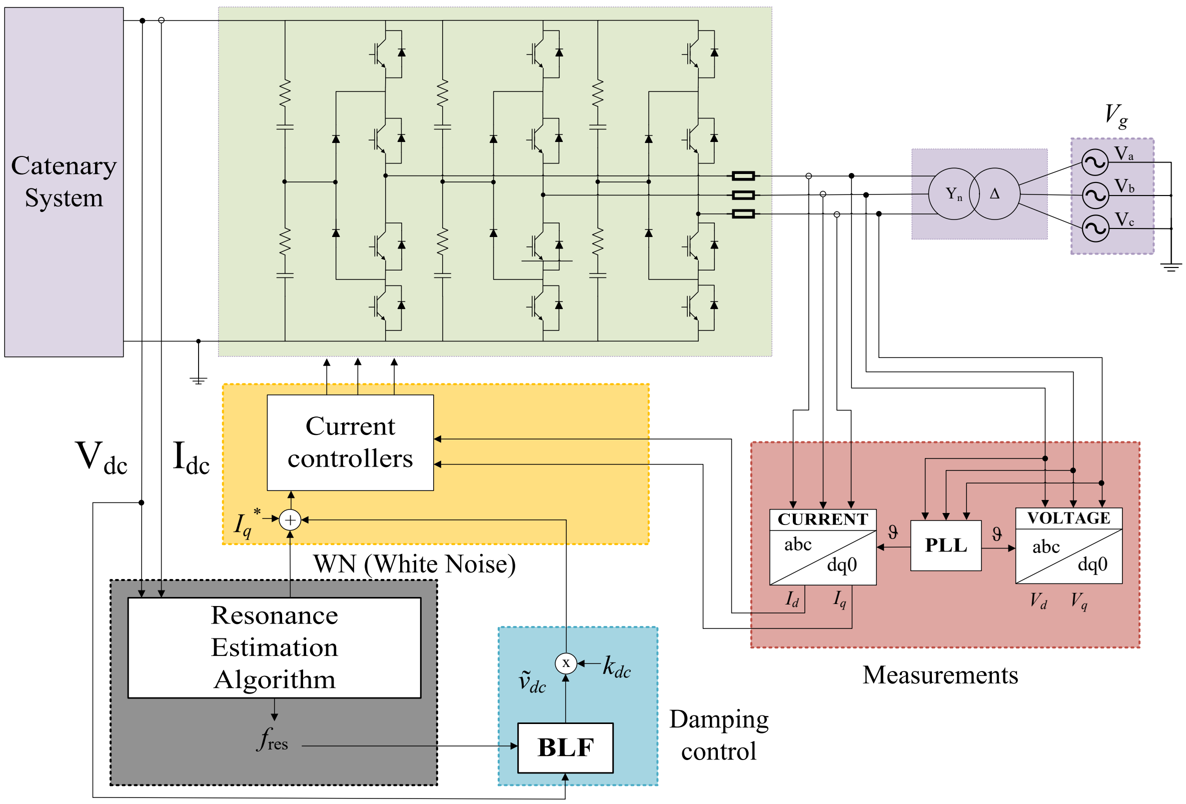

Figure 87. System block diagram including the Bandwidth Limiter Filter (BLF).

A. Generation of disturbance

For the estimation of the resonance frequency of the catenary, an appropriate disturbance is injected into the AC network by modifying the I_q current reference of the ERS for the duration of one second. The concept is to inject a disturbance, which is White Noise based, having constant magnitude and spread frequency spectrum. Then, by evaluating the frequency response of the system to the stimulus, the real-time analysis assesses where the signal is attenuated and where it is amplified. Concerning the amplitude of the disturbance, it is generated with amplitude $u\pm 1$ (i.e., normalized output) and then multiplied by a scale factor A_{wn}, Figure 88. The selection of the multiplication factor is related to the full scale of the current sensors (i.e. the rated power of the converter). The greater the converter current rating, the higher the magnitude of injected disturbance must be in order to discriminate the grid response within acquired data.

B. Disturbance injection, sampling and frequency estimation

There are different methods for resonance estimation. Most of them rely on prior knowledge of the circuit. Others estimate the resonance by stimulating the system, as in the proposed method. The substantial difference lies in the application and in the lack of knowledge of the circuit whose resonance must be estimated since it varies over time. Figure 88 shows the block diagram that summarizes the proposed methodology used to estimate the resonance frequency in real-time.

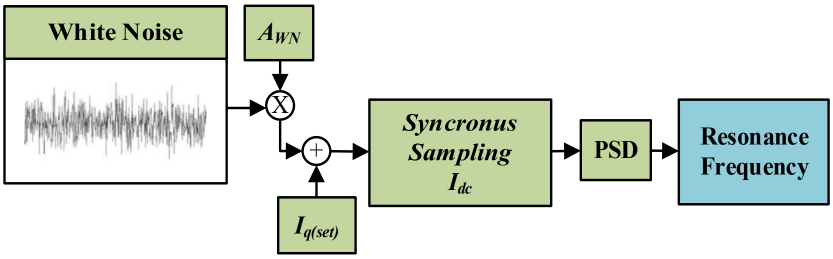

Figure 88. Block diagram of the signal injection and resonance estimation.

Figure 89 shows the White Noise Power Spectrum Density (PSD) that is injected into the network.

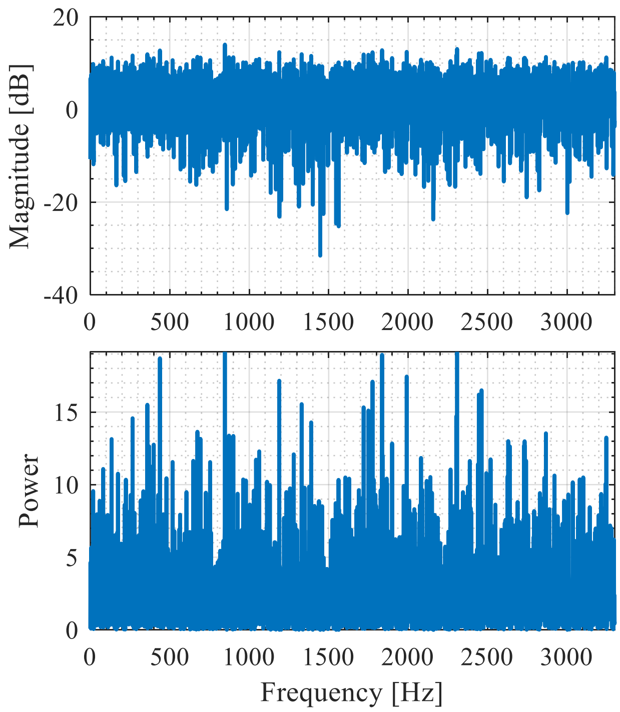

Figure 89. White Noise Power Spectrum Density.

Later it will be compared with the PSD of the acquired overhead contact line current. Once the disturbance is introduced and the current values are synchronously sampled, it is possible to proceed with the estimation of the resonance frequency by searching for the maximum value which can be found by evaluating the Power Spectrum Density of the catenary current. It must be noticed that specific attention must be given to the harmonics which are related to the AC fundament frequency, i.e., *50 Hz*, *300 Hz*, etc.

C. Bandwidth limiter filter and active damping

The bandwidth limiter filter consists of a pair of high-pass and low-pass filters which subtract their outputs from the input signal, to remove the DC component. Therefore, a signal composed by the harmonics higher than one tenth of the resonant frequency and lower than ten times the resonant frequency itself is obtained (i.e. useless harmonic content is not forwarded to the processing algorithm). The block diagram of the bandwidth limiter filter structure and frequency selection is shown in the Figure 90, whereas Figure 91 summarizes the operation to remove the DC component, highlighting the signal information close to the resonance frequency. In the investigated applications the used sampling frequency is *6600 Hz*, which is twice the switching frequency of the ERS converter, regardless of the resonance value the imposed range for acceptable cut-off frequencies could be between *5* and *3300 Hz*. This is due to the range of specific power of the converter, which reduces the range of observation frequencies. Once the catenary voltage is filtered, the signal corresponding to the voltage fluctuations around the estimated resonance frequency is obtained, $\tilde{v}_{dc}$. This signal is then multiplied by the K_{dc} factor becoming the input signal for the damping control, which acts directly on the AC current regulation, Figure 92. The concept and the operation of the bandwidth limiter filter is graphically depicted in Figure 93, where the zone highlighted in yellow is referred as the area of interest for the feedback signal.

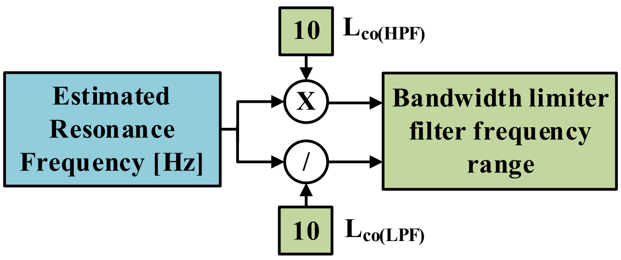

Figure 90. Block diagram of the analysis and cut-off frequency filter.

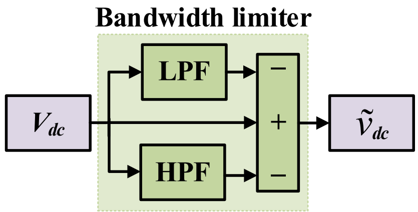

Figure 91. Block diagram Bandwidth Limiter Filter (BLF).

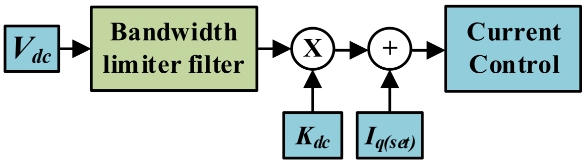

Figure 92. Block diagram of damping control.

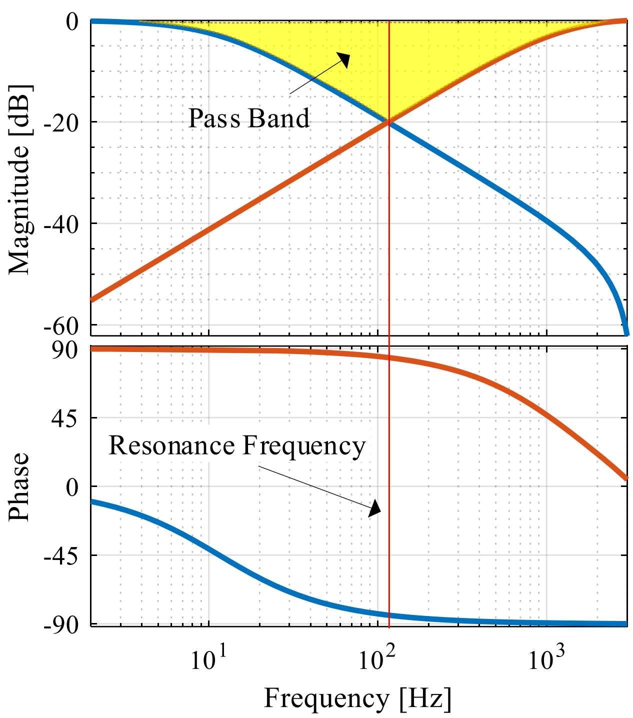

Figure 93. Low-pass and high-pass filters Bode plots

Figure 94 shows the bode plots of the open loop current loop and the damping control. The area where the damping control is able to operate is marked green. Figure 95 shows the block diagram of the basic operation of the control. The system consists of two nested control loops. The outermost loop is necessary to stabilize the catenary voltage V_{dc}, while the inner loop controls the grid current. The damping control, as visible in Figure 95, is integrated into the outer loop, resulting in a component of the total current reference I_q. Conceptually, the damping control acts on the whole system, providing a suitable harmonic compensation around the resonant frequency..

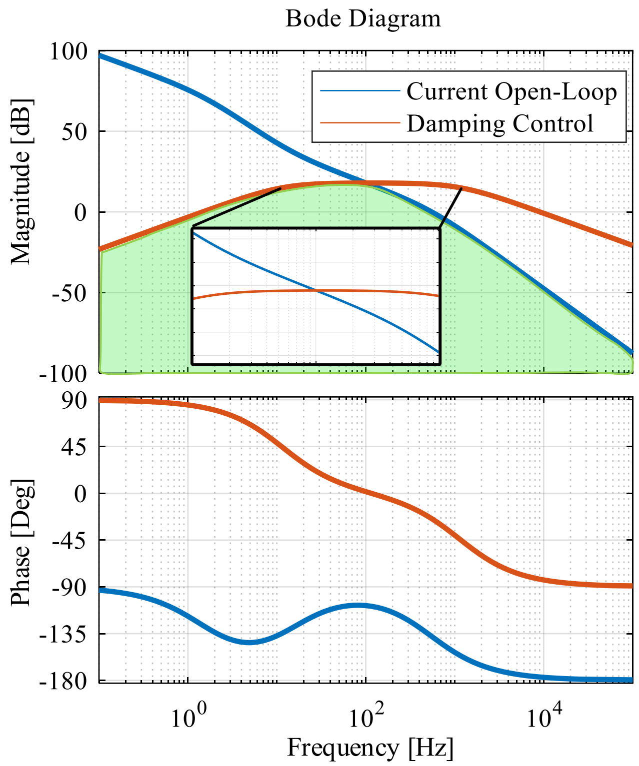

Figure 94. Bode Diagrams for the damping control and current loop.

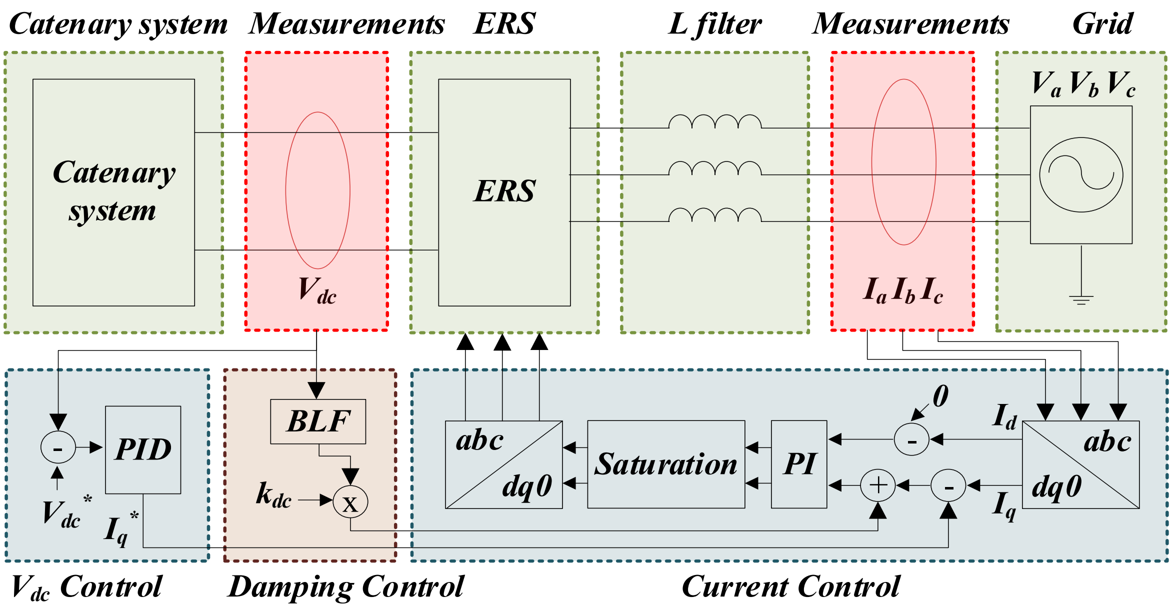

Figure 95. Control block diagram of the energy recovery system.

5.1 Experimental Results

The validation of the proposed damping control methodology has been carried out using a Hardware-In-The-Loop (HIL) real-time emulator, shown in Figure 96, which allows to obtain the proof of work of the proposed algorithm: the environment is under a controlled impedance state (i.e., the catenary resonance is unknown), in addition to the obvious beneficial in terms of safety. The power inverter and the catenary have been real-time emulated by the eHS64 Gen4 FPGA solver from OPAL-RT.

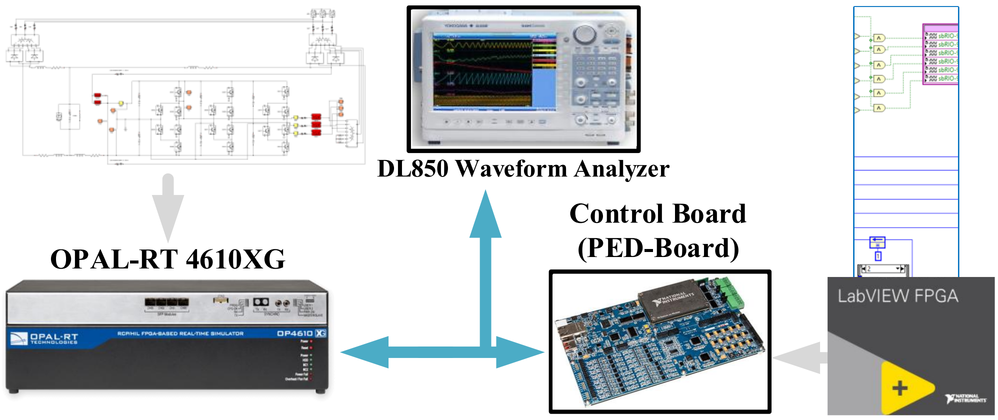

Figure 96. HIL arrangement.

Figure 97 shows the 2.5 MW energy recovery system based on a twin-NPC inverter installed in the substation.

Figure 97. Energy Recovery System.

The high-fidelity OP4610XG Hardware-In-the-Loop platform allows to correctly represent the power converter behaviour when connected to the grid and to the railway catenary. The control structure, the data acquisition and buffering scheme are implemented on the PED-Board® controller directly on the FPGA, taking advantage of the LabVIEW graphical environment. The PED-Board is based on the System-on-Module sbRIO-9651 from National Instruments incorporating a Xilinx Zynq7020.

A. Catenary response to the White Noise injection

First, it is remarked that the catenary current is not directly regulated, as it depends on the Energy Recovery System operating point set by controlling the AC side current. Figure 98 shows the catenary response (inverter DC side) when the stimulus is injected on the AC grid side. It is possible to see how the injection of noise into the AC-side of the inverter results in a disturbance also into the DC-side. The analysis of the DC side current using the PSD will allow to understand how these oscillations mainly depend on the circuit resonant frequency falling within the frequency bandwidth of the injected disturbance.

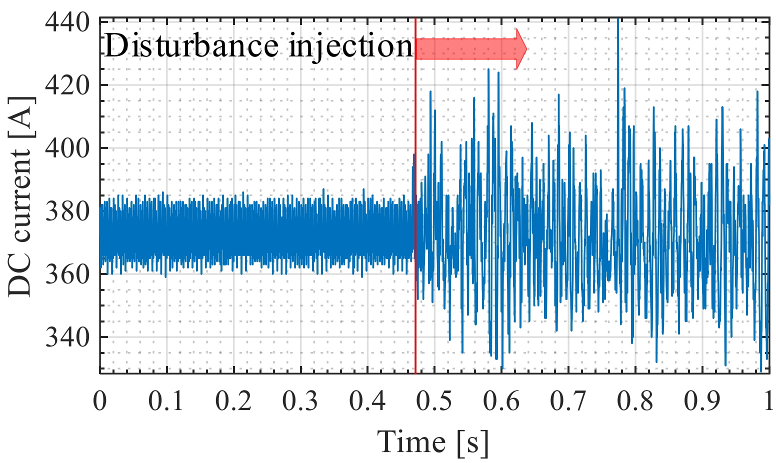

Figure 98. Effects of White Noise injection from the catenary side.

B. Power Spectrum Density (PSD)

Figure 99 shows the PSD obtained by sampling the voltage and current on the catenary at the connection to the ERS when the train injects power into the catenary and the inverter transfers it to the grid.

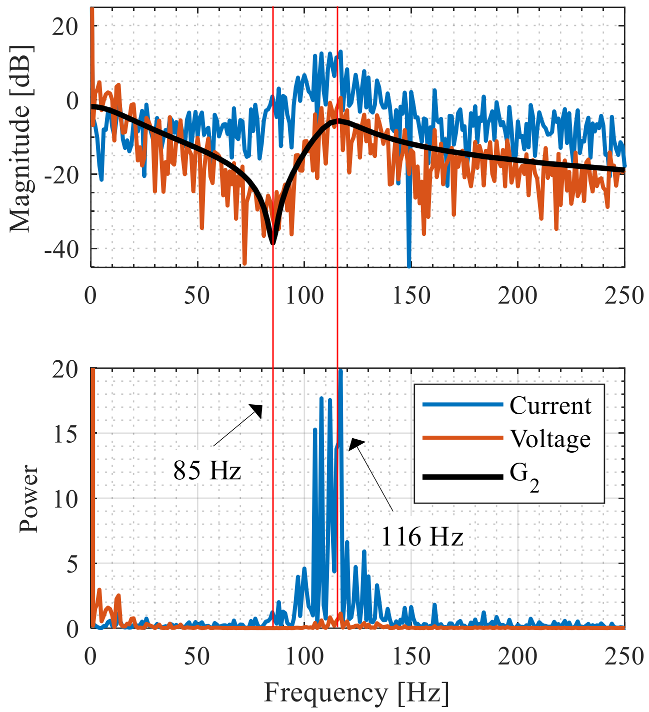

Figure 99. Catenary side PSD.

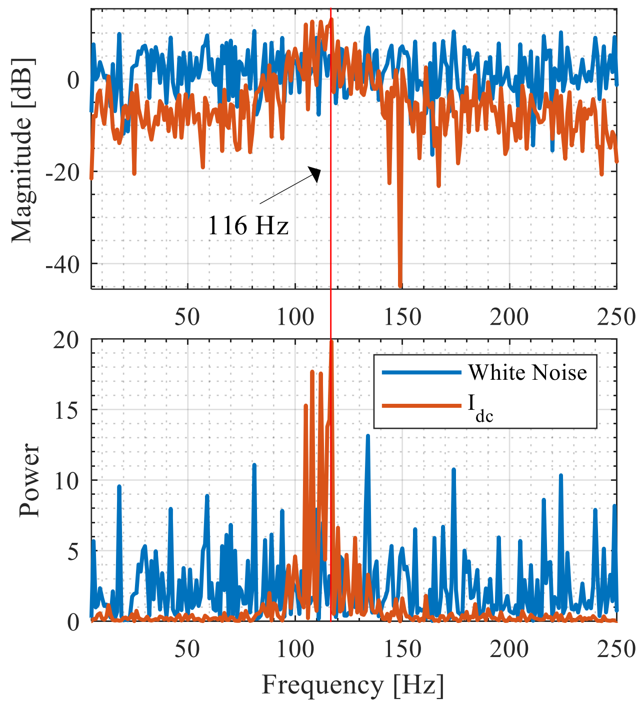

Figure 100. Comparison of White Noise and catenary current PSD.

From the analysis of the PSD, it can be deduced that there are two changes of slope in the voltage curve, respectively at about *85 Hz* and *116 Hz*, with a resonance on the current at about

116 Hz. Comparing these values which are obtained experimentally with those obtained analytically in the previous analysis and shown in Figure 85, a very strong agreement can be found between the two results, which allows to validate the proposed approach for the real-time resonance estimation. Figure 100 shows the response of the catenary current to the introduction of White Noise. The blue trace represents the PSD of the White Noise disturbance introduced into the AC grid by ERS. In orange, it is reported the PSD obtained from the measured DC current circulating in the catenary. It can be easily recognized how the catenary exhibits attenuative behaviour outside the resonant frequency. Hence, it would be effective to recognize where the resonant frequency is located and then take the proper action.

C. Damping control

In the introduction, it was explained how one of the negative effects of the Constant Power Load (CPL) is when the frequencies of the oscillations introduced by the ERS fall within the resonance frequencies of the catenary. Therefore, the situation in which the resonance of the catenary is stimulated by a disturbance deriving from the Energy Recovery System has been recreated. Then the results were obtained in the condition where the train is in the recovery phase by introducing the same stimulus used for the resonance estimation. This last choice is motivated by having a comparison on the attenuation of the disturbance exactly under the same operating conditions. To fully understand the motivation, it can be imagined that while the train is in the recovery braking, it approaches or move away from the ERS. Hence, it causes the impedance to vary over the time, affecting also the resulting resonant frequency. At the same time, the ERS introduces oscillations at low frequencies, which are attenuated if they do not coincide with the resonant frequency. On the other case, if some of these frequencies fall within the resonant frequency, the oscillations are amplified causing a possible stop of the trains. Figure 101 shows the catenary current PSD results when the proposed active damping control is disabled and enabled, considering a K_{dc} factor equal to *8*. It can be noticed that when the damping control is activated the power spectrum around the resonance frequency is perfectly attenuated, making the proposed solution effective. The goal would be to have a damping algorithm that can remain silent until a resonance condition is detected, i.e., when the frequencies generated by the inverter fall in the range of the resonant frequency of the catenary. From a mathematical standpoint, the effect of the proportional component (K_{dc}) on the transfer function is to artificially increase the DC-side equivalent resistance of the energy recovery system and effectively introduce active damping of resonance.

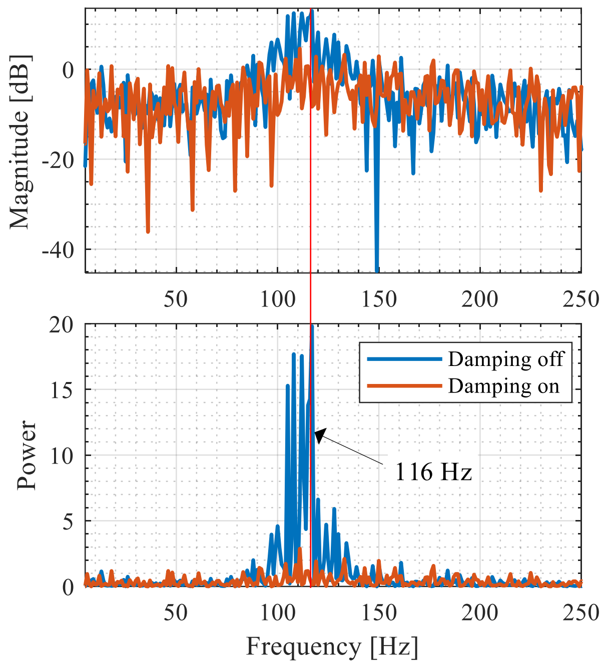

Figure 101. Resonance response with and without the proposed damping control.

Figure 102 illustrates the transfer functions with and without damping control, along with the experimental results obtained through Hardware-in-the-Loop (HIL).

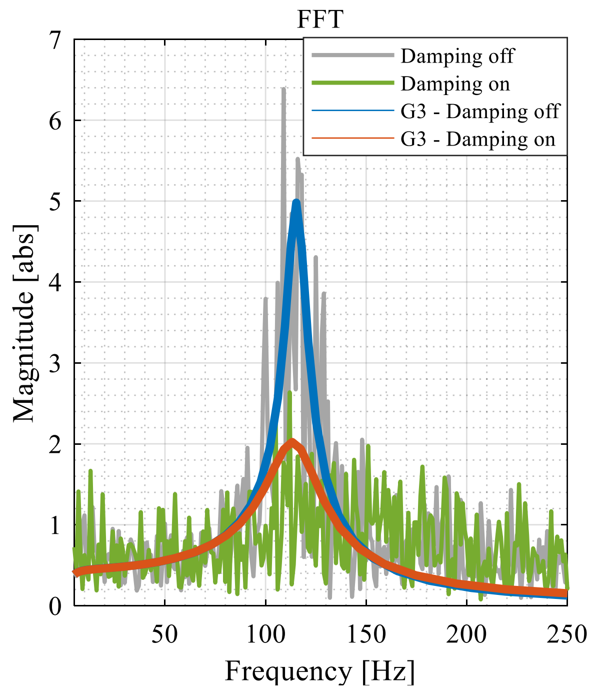

Figure 102. FFT with and without the Damping Control.

The transfer function with damping control (G3) is expressed as in (90).

$$G_3 = \frac{I_{cat}}{I_{ers}} = 1 - \frac{\left(Z_{ctrt} + 2Z_{ers-DC}\right)}{\left(Z_{ctrt} + 2Z_{ers-DC}\right) + \left(\frac{\left(R_{ers} \cdot K_{dc} + \frac{1}{C_{ers}}\right) \cdot R_l}{\left(R_{ers} \cdot K_{dc} + \frac{1}{C_{ers}}\right) + R_l}\right)} \tag{90}$$

From Figure 103 it can be noticed that the value of K_{dc} directly affects the quality and the damping, when the attenuation factor increases the resonance damping is stronger.

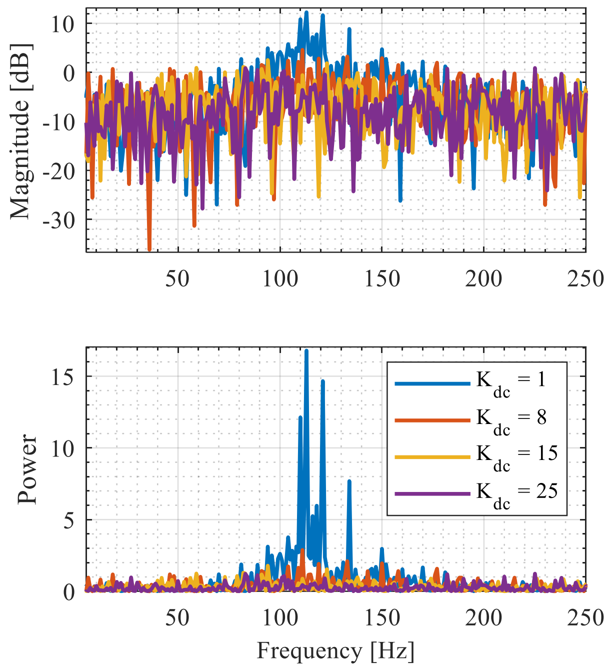

Figure 103. Effects of different K_{dc} values on the DC side current.

However, increasing the attenuation coefficient has a drawback on the quality of the AC side current. Accordingly, the selection of the K_{dc} factor must be a trade-off between the response of the damping control acting on the catenary and the disturbance injected into the grid. Figure 104 shows the PSD of the AC current, and it is evident that as K_{dc} increases, the current fluctuations increase too. Therefore, based on this analysis it was decided to choose K_{dc} equal to *8* as a compromise between damping and quality of the current waveform.

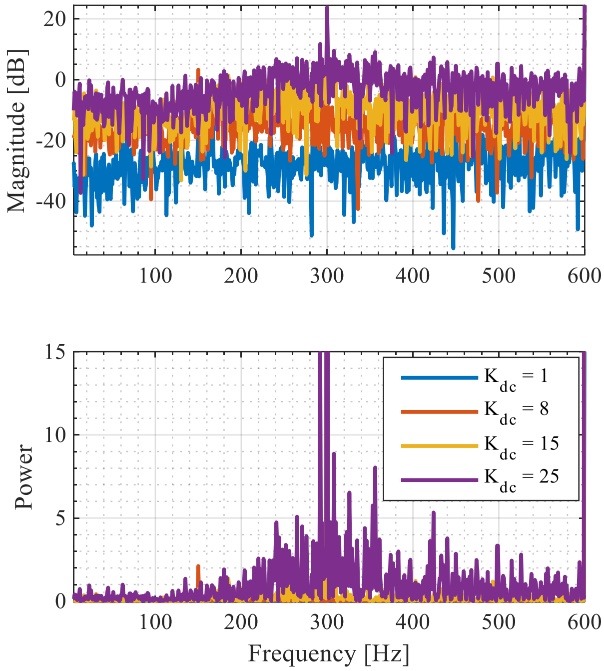

Figure 104. Effects of different K_{dc} values on the AC side current.

6 Conclusions

This dissertation confirms, through a consistent set of experimental campaigns, that impedance awareness can be embedded in the control layer of grid connected converters and used immediately for stability-oriented actions, without relying on prior knowledge of the network and without introducing disruptive operating conditions. The experimental results demonstrate that active impedance estimation can be executed online by injecting a bounded disturbance on the current reference and by processing synchronously sampled voltage and current measurements, and that the same measurement pipeline supports both AC side and DC side characterization when the excitation is applied on the AC side.

The work presents two complementary active strategies. The white Noise based approach is validated as a practical baseline due to its simplicity, broad spectral coverage, and compatibility with real time implementation, and the experiments highlight that the estimation bandwidth and reliability are naturally shaped by the converter control and filter dynamics, making resonance awareness an integral part of the estimation process rather than a separate offline analysis. The Multi-Sine strategy is then experimentally shown to provide a more controllable excitation profile, where energy can be concentrated only at the frequencies that are actually used for estimation, and the comparative tests against other common stimuli demonstrate that the main benefit is the ability to extract the needed information with the minimum necessary stimulation, improving repeatability and reducing invasiveness under equivalent disturbance effort.

Building on these identification results, the experimental sections dedicated to self commissioning and active damping show that estimated impedance is not only measurable but actionable, because it can be translated into automatic controller updates that recover the intended closed loop dynamics when grid strength changes, and it can be used to configure damping terms that suppress oscillatory behaviour near the stability boundary. The validation is carried out across a broad set of impedance conditions, confirming that the workflow remains robust from strong to weak grids, and that the combination of estimation, gain adaptation, and damping yields a stable and predictable response even when nominal tuning becomes inadequate.

In addition, the experimental evidence supports a hybrid operational philosophy where active identification is performed only when needed: the Quasi-Passive scheme is presented as an event driven layer that monitors the adequacy of the current estimate and triggers a short identification routine only when the measurements indicate that the grid has changed enough to compromise model fidelity, thereby limiting disturbance injection while maintaining control performance.

The passive method based on natural operating point variation further complements the toolbox by showing that, when sufficient spectral richness is already present in the measured signals, useful impedance information can be obtained without deliberate excitation, with experiments confirming that this approach is particularly meaningful in the low frequency region that most directly affects grid impedance modelling and control interaction in LCL filtered converters.

In parallel, the experimental results in the railway chapter demonstrate that the same impedance aware logic can be translated from grid impedance estimation to real time resonance tracking in DC traction systems, where the objective is to identify the dominant resonance from catenary measurements and to apply damping selectively around that resonance through the converter control, without injecting any signal directly on the catenary. The measurements confirm that a resonance signature can be extracted from the power spectrum density of synchronously sampled voltage and current and that the identified resonance aligns with the expected system behaviour, validating the estimation method under controlled yet realistic conditions. Finally, the damping control results indicate that attenuation is achieved where it is needed, around the resonance region, and that the control action can be confined in frequency by appropriate filtering, thereby mitigating low frequency oscillations while preserving the remainder of the operating spectrum, which is essential in railway environments where stability and signalling compatibility must be maintained simultaneously.

7 References

[1] T. Strasser, F. Andren, J. Kathan, C. Cecati, C. Buccella, P. Siano, P. Leitao, G. Zhabelova, V. Vyatkin, P. Vrba and V. Marik, “A Review of Architectures and Concepts for Intelligence in Future Electric Energy Systems,” *IEEE Transactions on Industrial Electronics,* vol. 62, p. 2424–2438, April 2015.

[2] S. Potrč, L. Čuček, M. Martin and Z. Kravanja, “Sustainable renewable energy supply networks optimization – The gradual transition to a renewable energy system within the European Union by 2050,” *Renewable and Sustainable Energy Reviews,* vol. 146, p. 111186, August 2021.

[3] P. S. Georgilakis and N. D. Hatziargyriou, “A review of power distribution planning in the modern power systems era: Models, methods and future research,” *Electric Power Systems Research,* vol. 121, p. 89–100, April 2015.

[4] F. Blaabjerg, R. Teodorescu, M. Liserre and A. V. Timbus, “Overview of Control and Grid Synchronization for Distributed Power Generation Systems,” *IEEE Transactions on Industrial Electronics,* vol. 53, p. 1398–1409, October 2006.

[5] X. Wang, M. G. Taul, H. Wu, Y. Liao, F. Blaabjerg and L. Harnefors, “Grid-Synchronization Stability of Converter-Based Resources—An Overview,” *IEEE Open Journal of Industry Applications,* vol. 1, p. 115–134, 2020.

[6] M. A. K. Magableh, A. A. A. Radwan and Y. Abdel-Rady I. Mohamed, “Dynamic Analysis and Stability Enhancement of a Weak Grid-Tied Hybrid System Integrating PV, Full-Scale Wind Turbine, and Battery Storage,” *IEEE Open Journal of Industry Applications,* vol. 6, p. 325–349, 2025.

[7] L. Kong, Y. Xue, L. Qiao and F. G. Wang, "Online-Harmonic-Detection-Based System Stabilization Function for Grid-Forming Inverters Under Various Grid Conditions," *in IEEE Open Journal of Power Electronics, vol. 4, pp. 2-13, 2023.*

[8] Y. Chen, W. Han, Y. Hu and Y. Zhang, “Adaptive Control for Improved Virtual Synchronous Generator Under Imbalanced Grid Voltage,” *IEEE Open Journal of the Industrial Electronics Society,* vol. 5, p. 722–736, 2024.

[9] Y. Han, M. Yang, H. Li, P. Yang, L. Xu, E. A. A. Coelho and J. M. Guerrero, “Modeling and Stability Analysis of LCL -Type Grid-Connected Inverters: A Comprehensive Overview,” *IEEE Access,* vol. 7, p. 114975–115001, 2019.

[10] F. Carnielutti, T. D. C. Busarello, Ê. C. Resende, Q. Ullah and M. G. Simões, “Fixed Switching Frequency Model Predictive Control for Grid-Forming Inverters,” *IEEE Transactions on Power Electronics,* vol. 40, p. 9080–9089, July 2025.

[11] O. Dankar, M. Tarnini, A. El Ghaly, N. Moubayed and K. Chahine, “A Neural Network-Based Model Predictive Control for a Grid-Connected Photovoltaic–Battery System with Vehicle-to-Grid and Grid-to-Vehicle Operations,” *Electricity,* vol. 6, p. 32, June 2025.

[12] M. Liserre, F. Blaabjerg and S. Hansen, “Design and Control of an LCL-Filter-Based Three-Phase Active Rectifier,” *IEEE Transactions on Industry Applications,* vol. 41, p. 1281–1291, September 2005.

[13] E. Twining and D. G. Holmes, “Grid current regulation of a three-phase voltage source inverter with an LCL input filter,” *IEEE Transactions on Power Electronics,* vol. 18, p. 888–895, May 2003.

[14] J. F. Guerreiro, T. D. C. Busarello, H. Guillardi, I. A. Maronni, J. D. A. O. Filho, H. K. M. Paredes and J. A. Pomilio, “Self-Stabilization of Grid-Connected Inverters by Means of an Impedance-Based Adaptive Controller,” *IEEE Open Journal of Industry Applications,* vol. 6, p. 366–381, 2025.

[15] R. Peña-Alzola, M. Liserre, F. Blaabjerg, R. Sebastián, J. Dannehl and F. W. Fuchs, “Analysis of the Passive Damping Losses in LCL-Filter-Based Grid Converters,” *IEEE Transactions on Power Electronics,* vol. 28, p. 2642–2646, June 2013.

[16] R. Peña-Alzola, M. Liserre, F. Blaabjerg, M. Ordonez and T. Kerekes, “A Self-commissioning Notch Filter for Active Damping in a Three-Phase LCL -Filter-Based Grid-Tie Converter,” *IEEE Transactions on Power Electronics,* vol. 29, p. 6754–6761, December 2014.

[17] R. Peña-Alzola, J. Roldán-Pérez, E. Bueno, F. Huerta, D. Campos-Gaona, M. Liserre and G. Burt, “Robust Active Damping in LCL-Filter-Based Medium-Voltage Parallel Grid Inverters for Wind Turbines,” *IEEE Transactions on Power Electronics,* vol. 33, p. 10846–10857, December 2018.

[18] D. Pan, X. Ruan, C. Bao, W. Li and X. Wang, "Capacitor-Current-Feedback Active Damping With Reduced Computation Delay for Improving Robustness of LCL-Type Grid-Connected Inverter," *IEEE Transactions on Power Electronics,* vol. 29, p. 3414–3427, July 2014.

[19] V. Blasko and V. Kaura, "A novel control to actively damp resonance in input LC filter of a three-phase voltage source converter," *IEEE Transactions on Industry Applications,* vol. 33, p. 542–550, 1997.

[20] L. Zhou, J. M. Guerrero, X. Zhou, Y. Chen, Z. Lv, Z. He, W. Wu, L. Yang, K. Yan and A. Luo, "Inverter-Current-Feedback Resonance-Suppression Method for LCL-Type DG System to Reduce Resonance-Frequency Offset and Grid-Inductance Effect," *IEEE Transactions on Industrial Electronics,* vol. 65, p. 7036–7048, September 2018.

[21] W. Yao, Y. Yang, X. Zhang and F. Blaabjerg, "Digital notch filter based active damping for LCL filters," in *2015 IEEE Applied Power Electronics Conference and Exposition (APEC)*, 2015.

[22] X. Wang, Y. He, D. Pan, H. Zhang, Y. Ma and X. Ruan, "Passivity Enhancement for \less{}{i}{}\greater{}{LCL}{}\less{}{/}{i}\greater{}{-}{F}iltered Inverter With Grid Current Control and Capacitor Current Active Damping," *IEEE Transactions on Power Electronics,* vol. 37, p. 3801–3812, April 2022.

[23] J. Sun, "Impedance-Based Stability Criterion for Grid-Connected Inverters," *IEEE Transactions on Power Electronics,* vol. 26, p. 3075–3078, November 2011.

[24] A. Suárez, C. Blanco, P. García, Á. Navarro-Rodríguez and J. M. C. Rodríguez, "Grid Impedance Estimator for Active Multisource AC Grids," *IEEE Transactions on Smart Grid,* vol. 14, p. 2023–2033, May 2023.

[25] M. Liserre, R. Teodorescu and F. Blaabjerg, "Stability of photovoltaic and wind turbine grid-connected inverters for a large set of grid impedance values," *IEEE Transactions on Power Electronics,* vol. 21, p. 263–272, January 2006.

[26] R. Khatua, A. Haldar, A. Malkhandi, N. Senroy and S. Mishra, "A Noninvasive Measurement Technique of Grid and Converter Wideband Impedance," *IEEE Transactions on Industrial Informatics,* vol. 20, pp. 886-898, 2024.

[27] N. Mohammed and M. Ciobotaru, "Fast and accurate grid impedance estimation approach for stability analysis of grid-connected inverters," *Electric Power Systems Research,* vol. 207, p. 107831, June 2022.

[28] C. Burgos-Mellado, A. Costabeber, M. Sumner, R. Cárdenas-Dobson and D. Sáez, "Small-Signal Modelling and Stability Assessment of Phase-Locked Loops in Weak Grids," *Energies,* vol. 12, p. 1227, March 2019.

[29] D. D. Reigosa, F. Briz, C. B. Charro and J. M. Guerrero, "Islanding Detection in Three-Phase and Single-Phase Systems Using Pulsating High-Frequency Signal Injection," *IEEE Transactions on Power Electronics,* vol. 30, p. 6672–6683, December 2015.

[30] D. Reigosa, F. Briz, C. B. Charro, P. Garcia and J. M. Guerrero, "Active Islanding Detection Using High-Frequency Signal Injection," *IEEE Transactions on Industry Applications,* vol. 48, p. 1588–1597, September 2012.

[31] M. M. Mardani, N. Mijatovic and T. Dragičević, "Real-Time Grid Impedance Identification for Online Parameter Tuning of Predictive Control in Grid-Tied Converters Using Artificial Neural Networks," in *IECON 2023- 49th Annual Conference of the IEEE Industrial Electronics Society*, 2023.

[32] M. K. De Meerendre, E. Prieto-Araujo, K. H. Ahmed, O. Gomis-Bellmunt, L. Xu and A. Egea-Alvarez, "Review of Local Network Impedance Estimation Techniques," *IEEE Access,* vol. 8, p. 213647–213661, 2020.

[33] G. Di Nezio, G. Marini, S. D'Arco, E. Tedeschi and A. Lidozzi, "A Passive Grid Impedance Estimation Method in Exploiting Variable Operating Conditions," in *2024 IEEE Energy Conversion Congress and Exposition (ECCE)*, 2024.

[34] D. Babazadeh, A. Muthukrishnan, P. Mitra, T. Larsson and L. Nordström, "Real-time estimation of AC-grid short circuit capacity for HVDC control application," *{IET} Generation, Transmission {\&}amp$\mathsemicolon$ Distribution,* vol. 11, p. 838–846, March 2017.

[35] A. Das and C. C. Reddy, "An Analytical Approach to Locate Short Circuit Fault in a Cable Using Sweep Frequency Response Analysis," *IEEE Transactions on Industrial Electronics,* vol. 70, p. 5235–5244, May 2023.

[36] H. Temiz, O. Keysan and E. Demirok, "Adaptive controller based on grid impedance estimation for stable operation of grid-connected inverters under weak grid conditions," *IET Power Electronics,* vol. 13, p. 2692–2705, September 2020.

[37] Y. Liao and X. Wang, “Impedance-Based Stability Analysis for Interconnected Converter Systems With Open-Loop RHP Poles,” *IEEE Transactions on Power Electronics,* vol. 35, p. 4388–4397, April 2020.

[38] J. Fang, H. Deng and S. M. Goetz, “Grid Impedance Estimation Through Grid-Forming Power Converters,” *IEEE Transactions on Power Electronics,* vol. 36, p. 2094–2104, February 2021.

[39] M. Liserre, R. Teodorescu and F. Blaabjerg, “Multiple harmonics control for three-phase grid converter systems with the use of PI-RES current controller in a rotating frame,” *IEEE Transactions on Power Electronics,* vol. 21, p. 836–841, May 2006.

[40] R. Teodorescu, F. Blaabjerg, M. Liserre and P. C. Loh, “Proportional-resonant controllers and filters for grid-connected voltage-source converters,” *IEE Proceedings - Electric Power Applications,* vol. 153, p. 750, 2006.

[41] A. V. Timbus, P. Rodriguez, R. Teodorescu and M. Ciobotaru, “Line Impedance Estimation Using Active and Reactive Power Variations,” in *2007 IEEE Power Electronics Specialists Conference*, 2007.

[42] M. Cespedes and J. Sun, “Online grid impedance identification for adaptive control of grid-connected inverters,” in *2012 IEEE Energy Conversion Congress and Exposition (ECCE)*, 2012.

[43] W. Cai, B. Liu, S. Duan and C. Zou, “An Islanding Detection Method Based on Dual-Frequency Harmonic Current Injection Under Grid Impedance Unbalanced Condition,” *IEEE Transactions on Industrial Informatics,* vol. 9, p. 1178–1187, May 2013.

[44] M. Nahalparvari, M. Asoodar, I. Jahn, L. Bessegato, O. Despouys, S. Norrga and H.-P. Nee, “DC-Side Impedance Estimation of a Modular Multilevel Converter Through System Identification of a Partially Black-Boxed Control System,” *IEEE Transactions on Energy Conversion,* vol. 37, p. 2708–2721, December 2022.

[45] C. Yuan, P. Wang and H. Zhao, “Review of Impedance Measurement Methods in New Energy Scenarios,” in *2024 7th International Conference on Energy, Electrical and Power Engineering (CEEPE)*, 2024.

[46] N. Mohammed, M. H. Ravanji, W. Zhou and B. Bahrani, “Online Grid Impedance Estimation-Based Adaptive Control of Virtual Synchronous Generators Considering Strong and Weak Grid Conditions,” *IEEE Transactions on Sustainable Energy,* vol. 14, p. 673–687, January 2023.

[47] T. T. Tran, S. K. Gurumurthy, M.-Q. Tran, T.-A. Nguyen-Huu, T. Heins, F. Ponci, A. Monti and P. H. Nguyen, “Enhancing Performance of Andronov-Hopf Oscillator-Based Grid-Forming Converters in Microgrids With Non-Invasive Online Impedance Estimation,” *IEEE Transactions on Smart Grid,* vol. 14, p. 4479–4493, November 2023.

[48] M. Li, Y. Yuan, L. Li, L. Chen and H. Nian, “Online Multi-cascade DC Converter Impedance Measurement Method Based on Multi-sine Signal Injection,” in *2020 IEEE 1st China International Youth Conference on Electrical Engineering (CIYCEE)*, 2020.

[49] A. González-Gil, R. Palacin and P. Batty, “Sustainable urban rail systems: Strategies and technologies for optimal management of regenerative braking energy,” *Energy Conversion and Management,* vol. 75, p. 374–388, November 2013.

[50] Y. Hong, Z. Shuai, H. Cheng, C. Tu, Y. Li and Z. J. Shen, “Stability Analysis of Low-Frequency Oscillation in Train-Network System Using RLC Circuit Model,” *IEEE Transactions on Transportation Electrification,* vol. 5, p. 502–514, June 2019.

[51] G. Marini, A. Lidozzi, M. di Benedetto, M. Moranchel Pérez and L. Solero, “Real-Time Resonance Detection and Active Damping in Energy Recovery Railways Applications,” *IEEE Open Journal of the Industrial Electronics Society,* vol. 5, p. 916–927, 2024.

[52] I. A. Tasiu, Z. Liu, S. Wu, W. Yu, M. Al-Barashi and J. O. Ojo, “Review of Recent Control Strategies for the Traction Converters in High-Speed Train,” *IEEE Transactions on Transportation Electrification,* vol. 8, p. 2311–2333, June 2022.

[53] I. A. Tasiu, H. Wang, Z. Liu, Y. Zhang, Q. Zhang, X. Meng and W. Zhao, “Robust fuzzy stabilization control for the traction converters in high-speed train,” *Control Engineering Practice,* vol. 132, p. 105423, March 2023.

[54] H. Alenius, R. Luhtala, T. Messo and T. Roinila, “Autonomous reactive power support for smart photovoltaic inverter based on real-time grid-impedance measurements of a weak grid,” *Electric Power Systems Research,* vol. 182, p. 106207, May 2020.

[55] M. Sumner, A. Abusorrah, D. Thomas and P. Zanchetta, “Real Time Parameter Estimation for Power Quality Control and Intelligent Protection of Grid-Connected Power Electronic Converters,” *IEEE Transactions on Smart Grid,* vol. 5, p. 1602–1607, July 2014.

[56] R. Pena-Alzola, M. Liserre, F. Blaabjerg, R. Sebastian, J. Dannehl and F. W. Fuchs, “Systematic Design of the Lead-Lag Network Method for Active Damping in LCL-Filter Based Three Phase Converters,” *IEEE Transactions on Industrial Informatics,* vol. 10, p. 43–52, February 2014.

[57] G. Zhang, Z. Liu, S. Yao, Y. Liao and C. Xiang, “Suppression of Low-Frequency Oscillation in Traction Network of High-Speed Railway Based on Auto-Disturbance Rejection Control,” *IEEE Transactions on Transportation Electrification,* vol. 2, p. 244–255, June 2016.

[58] Y. Liao, H. Wu, X. Wang, M. Ndreko, R. Dimitrovski and W. Winter, "Stability and Sensitivity Analysis of Multi-Vendor, Multi-Terminal HVDC Systems," *in IEEE Open Journal of Power Electronics, vol. 4, pp. 52-66, 2023.*

[59] M. Cespedes and J. Sun, “Adaptive Control of Grid-Connected Inverters Based on Online Grid Impedance Measurements,” *IEEE Transactions on Sustainable Energy,* vol. 5, p. 516–523, April 2014.

[60] J. Koppinen, J. Kukkola and M. Hinkkanen, “Plug-In Identification Method for an LCL Filter of a Grid Converter,” *IEEE Transactions on Industrial Electronics,* vol. 65, p. 6270–6280, August 2018.

[61] M. Li, H. Nian, B. Hu, Y. Xu, Y. Liao and J. Yang, “Design Method of Multi-Sine Signal for Broadband Impedance Measurement Considering Frequency Coupling Characteristic,” *IEEE Journal of Emerging and Selected Topics in Power Electronics,* vol. 10, p. 532–543, February 2022.

[62] G. Marini, A. Lidozzi, M. di Benedetto and L. Solero, “Multi-SIN Based Real-Time Impedance Estimation for Grid-Tied VSI,” in *2024 Energy Conversion Congress & Expo Europe (ECCE Europe)*, 2024.

[63] P. Magne, B. Nahid-Mobarakeh and S. Pierfederici, “Dynamic Consideration of DC Microgrids With Constant Power Loads and Active Damping System—A Design Method for Fault-Tolerant Stabilizing System,” *IEEE Journal of Emerging and Selected Topics in Power Electronics,* vol. 2, p. 562–570, September 2014.

[64] J. Mace, “Enhancing the Perturbation Injection Capabilities of Grid-Connected Converters With Asymmetric Signals,” *CPSS Transactions on Power Electronics and Applications,* vol. 9, September 2024.

[65] S. Arora, P. Balsara and D. Bhatia, “Input–Output Linearization of a Boost Converter With Mixed Load (Constant Voltage Load and Constant Power Load),” *IEEE Transactions on Power Electronics,* vol. 34, p. 815–825, January 2019.

[66] X. Zhu, F. Meng, Z. Xie and Y. Yue, “An Inertia and Damping Control Method of DC–DC Converter in DC Microgrids,” *IEEE Transactions on Energy Conversion,* vol. 35, p. 799–807, June 2020.

[67] S. Sanchez and M. Molinas, “Large Signal Stability Analysis at the Common Coupling Point of a DC Microgrid: A Grid Impedance Estimation Approach Based on a Recursive Method,” *IEEE Transactions on Energy Conversion,* vol. 30, p. 122–131, March 2015.

[68] Z. Liu, Y. Wang, S. Liu, Z. Li, H. Zhang and Z. Zhang, “An Approach to Suppress Low-Frequency Oscillation by Combining Extended State Observer With Model Predictive Control of EMUs Rectifier,” *IEEE Transactions on Power Electronics,* vol. 34, p. 10282–10297, October 2019.

[69] Y. Li, P. Jia and T. Q. Zheng, “Active damping method to reduce the output impedance of the DC–DC converters,” *IET Power Electronics,* vol. 8, p. 88–95, January 2015.

[70] O. Lorzadeh, I. Lorzadeh, M. N. Soltani and A. Hajizadeh, “Source-Side Virtual $\less$i$\greater${RC}$\less$/i$\greater$ Damper-Based Stabilization Technique for Cascaded Systems in {DC} Microgrids,” *IEEE Transactions on Energy Conversion,* vol. 36, p. 1883–1895, September 2021.

[71] H. Tian and Y. Li, “Virtual Resistor Based Second-Order Ripple Sharing Control for Distributed Bidirectional DC–DC Converters in Hybrid AC–DC Microgrid,” *IEEE Transactions on Power Electronics,* vol. 36, p. 2258–2269, February 2021.

[72] J. Xu and Y. Sato, “A DC-side damping control method for power converters to suppress resonance in DC power network,” *IEEJ Transactions on Electrical and Electronic Engineering,* vol. 7, p. 641–648, September 2012.

[73] H. Li, X. Ding, R. Xue, G. Li and Y. Chen, “Active Damping Adaptive Controller for Grid-Connected Inverter Under Weak Grid,” *IEEE Access,* vol. 9, p. 132442–132454, 2021.

[74] J. R. Massing, M. Stefanello, H. A. Grundling and H. Pinheiro, “Adaptive Current Control for Grid-Connected Converters With LCL Filter,” *IEEE Transactions on Industrial Electronics,* vol. 59, p. 4681–4693, December 2012.

[75] M. Cespedes, L. Xing and J. Sun, “Constant-Power Load System Stabilization by Passive Damping,” *IEEE Transactions on Power Electronics,* vol. 26, p. 1832–1836, July 2011.

[76] S. Shah and L. Parsa, "Impedance Modeling of Three-Phase Voltage Source Converters in DQ, Sequence, and Phasor Domains," *IEEE Transactions on Energy Conversion,* vol. 32, p. 1139–1150, September 2017.

[77] N. Hoffmann and F. W. Fuchs, "Minimal Invasive Equivalent Grid Impedance Estimation in Inductive–Resistive Power Networks Using Extended Kalman Filter," *IEEE Transactions on Power Electronics,* vol. 29, p. 631–641, February 2014.

[78] A. Vijayakumari, A. T. Devarajan and N. Devarajan, "Decoupled control of grid connected inverter with dynamic online grid impedance measurements for micro grid applications," *International Journal of Electrical Power {\&}amp$\mathsemicolon$ Energy Systems,* vol. 68, p. 1–14, June 2015.

[79] Q. Shu, Y. Fan, F. Xu, C. Wang and J. He, "A harmonic impedance estimation method based on AR model and Burg algorithm," *Electric Power Systems Research,* vol. 202, p. 107568, 2022.

[80] D. K. Alves, R. L. de Araujo Ribeiro, F. B. Costa, T. de Oliveira Alves Rocha and J. M. Guerrero, "Wavelet-Based Monitor for Grid Impedance Estimation of Three-Phase Networks," *IEEE Transactions on Industrial Electronics,* vol. 68, p. 2564–2574, March 2021.

[81] P. Zanchetta, A. Abusorrah, D. W. P. Thomas and M. Sumner, "Power System Impedance Estimation for Improved Active Filter Control, using Continuous Wavelet Transforms.," in *2005/2006 IEEE/PES Transmission and Distribution Conference and Exhibition*, 2006.

[82] T. Roinila, M. Vilkko and J. Sun, "Broadband methods for online grid impedance measurement," in *2013 IEEE Energy Conversion Congress and Exposition*, 2013.

[83] C. Vickery, R. Ali, H. Heydari-doostabad and T. O'Donnell, "Wideband Measurement of Grid Impedance Using Chirp Signals in Grid-Connected Inverters," in *2023 58th International Universities Power Engineering Conference (UPEC)*, 2023.

[84] J. Sihvo, T. Messo, T. Roinila and R. Luhtala, "Online Internal Impedance Measurements of Li-ion Battery Using PRBS Broadband Excitation and Fourier Techniques: Methods and Injection Design," in *2018 International Power Electronics Conference (IPEC-Niigata 2018 -ECCE Asia)*, 2018.

[85] N. Mohammed, M. Ciobotaru and G. Town, "Fundamental grid impedance estimation using grid-connected inverters: a comparison of two frequency-based estimation techniques," *IET Power Electronics,* vol. 13, p. 2730–2741, September 2020.

[86] N. Mohammed, M. Ciobotaru and G. Town, "Performance Evaluation of Wideband Binary Identification of Grid Impedance Using Grid-connected Inverters," in *2019 21st European Conference on Power Electronics and Applications (EPE19), ECCE Europe*, 2019.

[87] G. Marini, A. Lidozzi, M. d. Benedetto and L. Solero, "White Noise Based Synchronous Active DC and AC Impedance Estimation from Front-End Inverters," *IEEE Transactions on Energy Conversion,* vol. 39, p. 1–11, June 2023.

[88] X. Weng, Z. Zhao, K. Chen and L. Yuan, "Chirp Signal Injection Method and Real-Time Impedance Characteristic Measurement of Electric Energy Router," *IEEE Journal of Emerging and Selected Topics in Power Electronics,* vol. 10, p. 5564–5577, October 2022.

[89] Y. Wang, D. Tu, Q. Wang, H. Zhang and Y. Chen, "Multistage Design Method of Broadband Perturbation Signal for Impedance Measurement," *IEEE Transactions on Instrumentation and Measurement,* vol. 73, p. 1–13, 2024.

[90] F. A. Aroge and P. S. Barendse, "Time-Frequency Analysis of the Chirp Response for Rapid Electrochemical Impedance Estimation," in *2018 IEEE Energy Conversion Congress and Exposition (ECCE)*, 2018.

[91] M. Ciobotaru, R. Teodorescu, P. Rodriguez, A. Timbus and F. Blaabjerg, "Online grid impedance estimation for single-phase grid-connected systems using PQ variations," in *2007 IEEE Power Electronics Specialists Conference*, 2007.

[92] J.-H. Cho, K.-Y. Choi, Y.-W. Kim and R.-Y. Kim, "A novel P-Q variations method using a decoupled injection of reference currents for a precise estimation of grid impedance," in *2014 IEEE Energy Conversion Congress and Exposition (ECCE)*, 2014.

[93] Y. Cheng, W. Wu, M. Orabi, K. Eftychios, H. Chung and F. Blaabjerg, "A Novel Online Grid Impedance Measurement Method Based on Injecting Third Harmonic Voltage," in *2023 IEEE Energy Conversion Congress and Exposition (ECCE)*, 2023.

[94] N. Mohammed, T. Kerekes and M. Ciobotaru, "An Online Event-Based Grid Impedance Estimation Technique Using Grid-Connected Inverters," *IEEE Transactions on Power Electronics,* vol. 36, p. 6106–6117, May 2021.

[95] A. Charalambous, L. Hadjidemetriou and M. Polycarpou, “A Sensorless Asymmetric and Harmonic Load Compensation Method by Photovoltaic Inverters Based on Event-Triggered Impedance Estimation,” *IEEE Transactions on Industrial Electronics,* vol. 70, p. 10089–10100, October 2023.

[96] B. Palethorpe, M. Sumner and D. W. P. Thomas, “Power system impedance measurement using a power electronic converter,” in *Ninth International Conference on Harmonics and Quality of Power. Proceedings (Cat. No.00EX441)*.

[97] R. A. Fantino, C. A. Busada and J. A. Solsona, “Grid Impedance Estimation by Measuring Only the Current Injected to the Grid by a VSI With \textdollarLCL\textdollar Filter,” *IEEE Transactions on Industrial Electronics,* vol. 68, p. 1841–1850, March 2021.

[98] J. De Kooning, J. Van de Vyver, J. D. M. De Kooning, T. L. Vandoorn and L. Vandevelde, “Grid voltage control with distributed generation using online grid impedance estimation,” *Sustainable Energy, Grids and Networks,* vol. 5, p. 70–77, March 2016.

[99] K. Jia, T. Bi, B. Liu, E. Christopher, D. W. P. Thomas and M. Sumner, “Marine Power Distribution System Fault Location Using a Portable Injection Unit,” *IEEE Transactions on Power Delivery,* vol. 30, p. 818–826, April 2015.

[100] P. Garcia, M. Sumner, A. Navarro-Rodriguez, J. M. Guerrero and J. Garcia, “Observer-Based Pulsed Signal Injection for Grid Impedance Estimation in Three-Phase Systems,” *IEEE Transactions on Industrial Electronics,* vol. 65, p. 7888–7899, October 2018.

[101] M. M. Alyan Nezhadi, F. Zare and H. Hassanpour, “Passive grid impedance estimation using several short-term low power signal injections,” in *2016 2nd International Conference of Signal Processing and Intelligent Systems (ICSPIS)*, 2016.

[102] M. A. Khan, F. Taghizadeh, J. Lu and F. Bai, “Enhanced Online Impedance Estimation of Grid-Connected Inverter Using Hybrid Pseudorandom Binary Sequence,” in *2024 International Conference on Green Energy, Computing and Sustainable Technology (GECOST)*, 2024.

[103] G. Marini, N. Baschera, A. Lidozzi, M. d. Benedetto and L. Solero, “Multi-SIN Based Real-Time Impedance Estimation for Self-Commissioning Controller and Active Damping in an LCL-Grid-Tied VSI,” *IEEE Open Journal of Industry Applications,* p. 1–15, 2025.

[104] M. Liserre, A. Dell’Aquila and F. Blaabjerg, “Genetic Algorithm-Based Design of the Active Damping for an LCL-Filter Three-Phase Active Rectifier,” *IEEE Transactions on Power Electronics,* vol. 19, p. 76–86, January 2004.

[105] A. Lidozzi, L. Solero, F. Crescimbini and A. Di Napoli, “Direct tuning strategy for speed controlled PMSM drives,” in *2010 IEEE International Symposium on Industrial Electronics*, 2010.

[106] J. Xu, S. Xie and T. Tang, “Active Damping-Based Control for Grid-Connected LCL -Filtered Inverter With Injected Grid Current Feedback Only,” *IEEE Transactions on Industrial Electronics,* vol. 61, p. 4746–4758, September 2014.

[107] X. Wang, F. Blaabjerg and P. C. Loh, “Grid-Current-Feedback Active Damping for <italic>LCL</italic> Resonance in Grid-Connected Voltage-Source Converters,” *IEEE Transactions on Power Electronics,* vol. 31, p. 213–223, January 2016.

[108] J. L. Xie, D. C. Liao, T. T. Chen and J. Chen, “Active Damping and Passive Control Strategy for Three-Phase LCL Grid-Connected Inverter,” *IOP Conference Series: Earth and Environmental Science,* vol. 701, p. 012065, March 2021.

[109] X. Wan, Y. Li and M. Peng, “Modelling, analysis and virtual parallel resistor damping control of VSC-based DC grid using master–slave control mode,” *{IET} Generation, Transmission {\&}amp$\mathsemicolon$ Distribution,* vol. 12, p. 2046–2054, February 2018.

[110] Q. Zhu, Q. Li, J. Zhang and P. Cheng, “Virtual resistor circuit-based control strategy of STATCOM during network unbalance,” *The Journal of Engineering,* vol. 2017, p. 1804–1808, January 2017.

[111] J. You, Z. P. Fan, Y. Hu and H. J. Jia, “Virtual capacitor based DBVC and active damping method for cascaded power converters stabilization control,” in *2017 IEEE Transportation Electrification Conference and Expo, Asia-Pacific (ITEC Asia-Pacific)*, 2017.

[112] X. Chang, Y. Li, X. Li and X. Chen, An Active Damping Method Based on a Supercapacitor Energy Storage System to Overcome the Destabilizing Effect of Instantaneous Constant Power Loads in DC Microgrids, IEEE Transactions on Energy Conversion, vol. 32, no. 1, pp. 36-47, March 2017, 2017.

[113] Y. Yong, F. Gang, L. Jinjun, Jiangfeng and L. Tao, “A virtual RC active damping method in weak grid for three-level three-phase grid-connected inverters,” in *2016 IEEE 8th International Power Electronics and Motion Control Conference (IPEMC-ECCE Asia)*, 2016.

[114] A. Khodamoradi, H. Abdollahi, E. Santi and P. Mattavelli, “A Loop Gain-Based Technique for Online Bus Impedance Estimation and Damping in DC Microgrids,” *IEEE Transactions on Power Electronics,* vol. 36, p. 9648–9658, August 2021.

[115] *IEEE Recommended Practice for Terminology Used for Direct Current Electric Transit Overhead Contact Systems,* IEEE.

[116] “Appendix D: Self Inductance of a Straight Finite Cylindrical Wire,” in *Analysis of Faulted Power Systems*, IEEE, 2009.